# Design and Fabrication of Functional Contact Lenses with Integrated Light Emitting and Photovoltaic Components

Andrew Lingley

A dissertation
submitted in partial fulfillment of the
requirements for the degree of

Doctor of Philosophy.

University of Washington
2012

Reading Committee:
Babak A. Parviz, Chair
Brian P. Otis
Bruce Darling

Program Authorized to Offer Degree:
Electrical Engineering

University of Washington

# Abstract

## Design and Fabrication of Functional Contact Lenses with Integrated Light Emitting and Photovoltaic Components

Andrew Lingley

Chair of the Supervisory Committee:
Dr. Babak A. Parviz
Electrical Engineering

This dissertation presents progress toward the realization of functional contact lenses. Two primary goals of the functional contact lens project are to create displays for augmented reality and to create sensors to measure biomolecules in tears. First, work on contact lens displays is described, detailing the steps and process optimization required to fabricate fully functional contact lenses and culminating in the wireless activation of a single pixel contact lens display *in vivo* on a rabbit under general anesthesia. Next, solar cells designed to conform to a sphere for use with contact lens biosensors are described. To measure analytes in the tear film using electrochemical methods, contact lenses would require embedded sensors, electronics, antennas or LEDs for communication, and power sources. Ideally, a contact lens biosensor would be autonomous, provide regular readings, and operate during normal daily activity, thus requiring power continuously. Photovoltaic structures could provide continuous power for autonomous contact lens systems that could store sensor readings and communicate data when occasionally queried.

# Table of Contents

# List of Figures

# List of Tables

# Acknowledgements

First, I would like to thank my advisor, Dr. Parviz, for his imagination, intuition, enthusiasm, and guidance over the last five years. I would also like to thank all of my group members, particularly Ramin for his work developing the blue LED lenses and Christian for saving me probably hundreds of hours solder coating. Lastly I would like to thank my family, friends, and loved ones for their support and encouragement.

# Chapter 1: Introduction

There are many ways in which information can enter the brain. Arguably the most important is that of light reflecting or refracting off of various objects (books, trees, people, computer screens, etc.), collected by the eyes, and transmitted to various parts of the brain for specific processing. The first bodily object light encounters is the cornea, an essentially clear layer of cells that is, to first approximation, spherical in shape and that provides about two-thirds of the refractive power of the eye. Light then passes through the aqueous humor and pupil and is refracted dynamically by the crystalline lens. Finally, light passes through the vitreous humor and the bulk of the retina where it is absorbed by photoreceptors and undergoes transduction into an electrical signal. Amplification is performed by about $1.2 \times 10^8$ rods and $5 \times 10^6$ cones, and the resulting signal is sent to ganglion cells. Then this information passes through the million or so fibers of the optic nerve, into the brainstem, and on to the visual cortex. The human visual system operates over a wide range of light intensity (~12 orders of magnitude) and allows for color vision, judgment of distance and movement, and high resolution tasks such as reading this dissertation [1], [2].

Unfortunately, despite the complexity and adaptability of the visual system, some people cannot see clearly. Often this results from a misshapen cornea that projects a focused image behind or in front of the retina. Thus eyeglasses were invented and were the sole means of vision correction for centuries until the realization of contact lenses, which were initially blown glass structures fitted over the cornea and part of the sclera. Corneal lenses were patented in 1950, and the first soft contact lenses (made from poly-HEMA) were demonstrated in 1961. Rigid gas permeable lenses with high oxygen permeability were invented next, followed by silicone hydrogel soft lenses that are now ubiquitous [3]. Contact lenses are used by tens of millions worldwide in a market estimated at $6.1 billion in 2010 [4].

Although primarily used for vision correction (and occasionally for aesthetics), their location on the corneal surface presents unique opportunities for vision augmentation or biological monitoring [5]. For example, see-through displays could overlay computer-generated visual information on the real world, providing immediate, hands-free access to information. Additionally, because tears contain many biological molecules of interest, contact lenses could be used to track key biomarkers in tears [6]. Section 1.1 provides an overview of work toward creating a contact lens display, and Section 1.2 covers various contact lens sensors. Section 1.3 describes how contact lens sensors could act as part of wireless body area networks, and discusses why energy harvesting would maximize contact lens biosensor potential. Section 1.4 is a feasibility analysis directed at using solar cells to provide power for the various components necessary to realize such a system.

## 1.1 Contact lens displays

Wearable computing and augmented reality will likely provide new ways to manage information and interact with the world. The first step towards always-accessible, superimposed information will most likely be implemented in see-through eyeglass displays, such as those presented by Google’s Project Glass team. However, a much less cumbersome display for augmented reality may take the form of a contact lens. Like their larger counterparts, contact lens displays could communicate with internet enabled devices to retrieve discrete and real-time emails, text messages, reminders, or navigational information. Pioneering contact lens display development has been made by the Parviz Group at the University of Washington, with the long-term goal developing systems with pixel arrays, focusing optics, and antennas, as well as circuitry for power harvesting, radio communication, and pixel control (Figure 1).

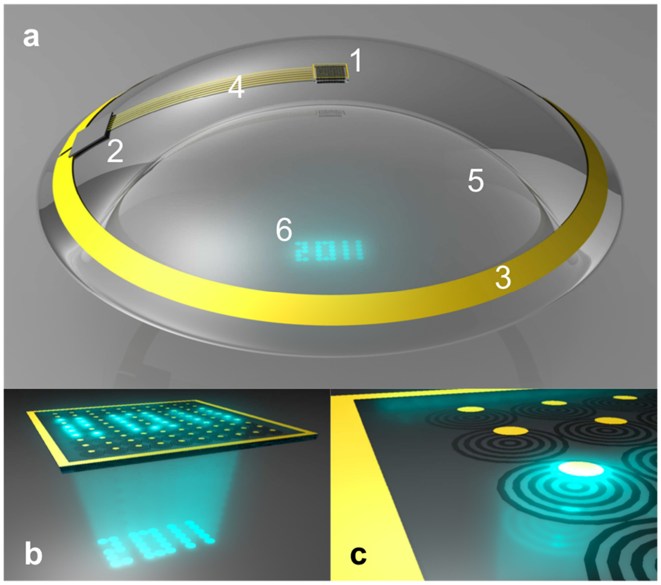

**Figure 1. Concept drawing of a multi-pixel contact lens display. a) A contact lens display comprising a multi-pixel light emitting diode chip (1), power-harvesting/control circuitry (2), an antenna (3), and interconnects (4). These subsystems are encapsulated in a transparent polymer (5), creating a system to project virtual images (6) perceivable by the eye of the wearer. b) LED chip with 100 pixels. LED active layers can be grown atop a transparent substrate. Emitted light travels through the substrate and is re-imaged using planar Fresnel lenses. c) Magnified view with one pixel activated, showing Fresnel lenses opposite each LED pixel.**

Integrating displays on contact lenses presents several challenges. First, as the display rests on the eye, power must be provided wirelessly. Second, the lens system must be biocompatible and meet various safety regulations for radio frequency (RF) radiation, thermal dissipation, etc. A third challenge is mechanical and electrical integration of heterogeneous micrometer-scale components (e.g. silicon integrated circuitry and III-V optoelectronics) on a polymer substrate. This requirement stems from the fact that low power systems would require highly efficient subcomponents, which at this time are necessarily solid state devices made using semiconductors. Furthermore, different semiconductors are ideal for different functions: LEDs typically require direct band gap materials, whereas low power circuitry is almost exclusively made using high purity silicon. All components must fit within the volume of standard contact lenses, ~1.0 cm$^2$ in area with thicknesses of 200 $\mu$m or smaller [3]. The optics required for contact lens displays are also very complex. The human eye, with a minimum focal distance of several centimeters, cannot resolve objects on resting on its surface. Two solutions to this problem are envisioned; light from LEDs could be focused using subsidiary lenses, or alternatively, beams from vertical cavity surface emitting lasers could be used to create an image. An overview of unfocused single-pixel contact lens displays is given below, and more detailed process development and system integration is given in Chapter 2:.

First, Harvey et al. devised a fabrication process to deposit two metal layers and polymer insulation on a clear polymer substrate, upon which an array of micrometer-scale LEDs was assembled. However, the LEDs failed when molding the device for corneal fitting [7]. Next, Pandey et al. used a similar fabrication process to create single pixel LED displays on planar polymer discs comprising custom integrated circuits (ICs), antennas, and LEDs. The on-lens antenna collected radiation from an external transmitter, and the power-harvesting IC rectified and stored energy to duty-cycle an LED at a frequency sufficiently high as to give the appearance of continual light emission [8]. The following year, the lenses were improved by electrolessly plating the custom ICs for flip-chip style assembly, and the polymer substrate fabrication process was modified to reduce antenna resistance and improve system performance [9]. Using flip-chip style assembly, an operational molded structure was realized. Building from these efforts, systems comprising single blue LEDs, antennas, and ICs were tested *in vivo* on rabbits [10].

To the author’s knowledge, the only other attempt at developing a contact lens display was by De Smet [11]. A contact lens display based on liquid crystal modulation of light was theorized, as well as additional uses such as tunable sunglasses or artificial irises. Voltage controlled liquid crystals were embedded between two polymer sheets separated by photolithographically defined spacers. After spherical molding, an applied voltage caused the transparent crystals to rotate and become opaque.

## 1.2 Contact lens sensors

Contact lenses have also been used, although almost strictly in laboratory environments, to perform a number of sensing functions. One of the first atypical applications for contact lenses was to measure eye movement. In 1963, Robinson used a contact lens containing two metal coils, together with an alternating magnetic field, to measure the induced voltage in accordance with Faraday's Law and thus eye movement. They were able to measure horizontal, vertical, and torsional movement at a resolution of 15 arcseconds [12]. In 1975 another group developed the scleral search coil to improve upon Robinson's device. Noting that slipping and bulging was difficult to control with lenses that were not individually fit, a ring shaped holder of silicon rubber with an embedded induction coil was fabricated to fit the limbic region (i.e. the cusp where the cornea connects to the sclera). The ring was designed with a concave inward surface that would tightly adhere when pressed onto an anesthetized eye. However, some subjects noted irritation from the wires extending from the ring [13]. The scleral search coil method has been used in countless studies on topics ranging from ocular counter-rolling [14] and motion after-effect [15] to eye movement in mice [16] and other animals [17]. More recently there has been an attempt to create a wireless version of a similar device. Kim, Lee, and Kim used a contact lens system that was essentially the inverse of Robinson's prototype. A thin, ring-shaped magnet was embedded into a contact lens and an eyeglass-shaped PCB board with magnetoresistive sensors was used to measure eye movement [18].

Kinn and Tell developed a contact lens to determine the temperature of the cornea using encapsulated liquid crystals. When illuminated with white light, the embedded liquid crystals would reflect in a temperature dependent manner and could thus provide temperature profiles across the cornea. However, the devices required calibration because contact lenses have an effect on corneal temperature due to insulation and reduction in evaporative cooling [19].

The only commercially available contact lens sensor for home use, to the author's knowledge, is a sensor that measures the curvature of the eye to determine intraocular pressure [20–22]. Leonardi spun-off SENSIMED and developed the Triggerfish® as a continuous intraocular pressure monitor commercially available in parts of Europe. The Triggerfish® is a system comprising a contact lens with integrated passive and active strain gauges and an application specific integrated circuit (ASIC), together with an adhesive antenna that is worn around the eye and connected to a recording device. The circuit, measuring 2.5 mm x 2.2 mm x 50 µm, receives power from the external antenna, provides power to the sensor, and converts the measured pressure response to a digital signal that is sent back to the recorder.

Glucose sensing is another active area of contact lens sensors. Self-monitoring of blood glucose (SMBG) has been shown to improve glycemic control in diabetics, delaying the onset of serious complications [23], [24]. Most of the billions of annual glucose assays are conducted by measuring levels in blood samples using electrochemical techniques. These methods are accurate but provide few data points, and additionally lancing to draw blood can cause discomfort or pain. To overcome these setbacks, research over the last several decades has been conducted to develop less invasive and more continuous glucose measurement techniques. It has been demonstrated that tear glucose correlates to blood glucose [25], [26], although in lower concentrations and with a time lag, and therefore glucose sensing contact lenses could prove an ideal tool for SMBG.

Badugu used off the shelf, disposable contact lenses embedded with boronic acid-containing fluorophores (BAFs) to measure glucose concentrations in tears. Intensity and wavelength changes were detected in the fluorescent spectrum of the BAFs in the presence of sugars. However, the fluorescence was pH and polarity dependent, and in the contact lens environment the sensing range was limited [27]. There have also been attempts to measure glucose in the tear film using colorimetric sensors based on reflection from photonic crystals. Again using boronic acid-based molecules for glucose recognition, the spacing of the photonic crystals decreased in the presence of glucose causing a blue-shift of the reflected light [28].

Chu used electrochemical methods to measure tear glucose. Platinum working electrodes and Ag/AgCl reference and counter electrodes were fabricated on flexible PDMS membranes with glucose oxidase as a recognition element. An oral glucose tolerance test was performed, revealing a delay of 10 minutes between blood and tear glucose. The sensor was wired, and the device did not incorporate any additional on-lens circuitry for readout [25]. Liao et al. also developed contact lens biosensors for glucose monitoring using a glucose oxidase-based approach, and demonstrated a system comprising a contact lens substrate with metal interconnects and sensor electrodes, readout circuitry, and an antenna for wireless backscattering of sensor data capable of measuring glucose concentrations ranging from 0 to 2 mM [29].

## 1.3 Contact lens sensors for continuous health monitoring

Increasing medical problems such as diabetes, obesity, cancer, and the associated physical an economic toll warrant a reexamination of current health care paradigms. As opposed to addressing illness in a reactionary fashion, one proposed method of reducing health care costs and managing diseases is to focus on prevention and early detection through the use of continuous health monitoring. Wireless body area networks (WBANs) consisting of multiple sensor nodes placed on or around the body to measure vitals and environmental parameters have been proposed to accomplish this goal. Individuals could track trends in their vitals and biochemistry at home in response to lifestyle changes, for example, or hospital patients could be monitored more closely after surgeries and the administration of prescriptions [30], [31]. Contact lenses are unique in that they are the only commercially available and commonly used product in intimate contact with tear fluid, which contains a variety of proteins, ions, and biomolecules that are continually refreshed. In concert with various other sensors, such as heart rate monitors and blood oxygen sensors, a contact lens sensor could provide biochemical information to help form a complete wireless sensor network for continuous personal health monitoring.

An active contact lens sensing system would be similar in concept to the system described in Figure 1. Like the display system, an active sensing system would have an antenna for communication, an application specific integrated circuit, and electrical interconnects, all contained within a thin polymer lens. However, the circuitry required would be very different, and instead of a pixel array it would contain a sensor or sensor array. Although a display would likely require some milliwatts, a sensing system could potentially operate on orders of magnitude less power, opening possibilities for autonomous sensing. An autonomous system would be ideal because it could most closely approximate continuous monitoring, provided that an adequate, on-lens power source could be included along with sufficient on-chip memory to store relevant biological information between times of communication with an external reader.

### 1.3.1 Sensor power requirements

Although many different physical phenomena can be utilized to measure the presence of target analytes, electrochemical transduction holds the most potential for developing contact lens biosensors. Electrochemical sensors combine a biological recognition element with a transducer to produce a measureable current or potential. Amperometric sensors are those in which a constant potential is applied to a system of electrodes, and the current responds in proportion to a biological reaction. Potentiometric sensors operate by converting biological recognition into a proportional voltage. Both sensors types can be highly selective and sensitive, and can be miniaturized for low power operation and to fit into small systems. For example, many amperometric sensors operate in the hundreds of millivolts, and have current outputs proportional to electrode size and analyte concentration that can be as smalls as tens of nano amps. Liao reported operation at 400 mV and up to 750 nA (300 nW max) [29] and Chu reported a full-scale sensor power of 600 nW (1.5 µA at 400 mV) [25].

In addition to electrochemical sensors located off-chip, there is a push to integrate sensors directly with CMOS circuitry. For example, ion-selective field-effect transistors and enzyme field-effector transistors operate on changes in transistor characteristics in response to biological reactions near the gate. Although work is needed to improve selectivity and sensitivity, these have been developed for penicillin, glucose, urea, and creatinine, among others [32]. On-chip CMOS temperature sensors, simpler than most electrochemical sensors, have been developed with extremely low power consumption as well. For example, Law et al. developed an ultra-low power CMOS temperature sensor for RFID food monitoring applications with sub-µW dissipation [33].

### 1.3.2 Circuitry and storage power requirements

The readout circuitry for glucose sensing reported in [34] required 3 µW. The circuit consisted of power management, readout, and wireless communication blocks, as well as energy storage capacitors. Yang et al. developed a compact impedance-to-digital converter (IDC) in a 0.5 µm CMOS process for use with impedance-based electrochemical sensors. Each operational IDC occupied100 µm x 600 µm area, consumed 2 µA on a 3 V supply, and could operate over a widely varying and configurable input current range (100 fA to 100 nA). The circuit was tested by measuring the ion transport activity of an artificial bilayer lipid membrane. Although the design was tailored for sensor arrays, a single unit could operate on very low power [35], [36]. To make a complete sensing system, this group later implemented an on-chip waveform generator, potentiostat, and amperometric readout in a circuit dissipating 22.5 mW. As more research is directed at ultra-low power systems, design principles and approaches for sub-threshold VLSI circuits are becoming better understood [37].

As mentioned above, a contact lens sensor system would be optimally beneficial if it could store data. Analyte concentrations could be read, stored on-lens, and queried occasionally, allowing for continuous monitoring, more convenience, and less user compliance. Self-powered wireless devices for a variety of other applications, such as sensor networks, wearable electronics, nanorobotics, biosensors, and MEMS, is an active area of research likely to drive down power requirements of sensors and circuitry in the coming years [38].

Chen et al. developed a “nearly perpetual” sensor system powered by two series connected 1 $mm^2$ solar cells and a Li thin-film battery with on-chip memory. The system collected data, performed data processing, and stored readings during a 7.7 µW active state, and then entered a 550 pW sleep state. During the active state, non-retentive SRAM and retentive SRAM were used, and in the sleep state only retentive RAM was used with 3.3fW/bit standby-power [39], later reduced to 1.85 fW/bit ([40]. An 8 kbit array of supply feedback SRAM (SF-SRAM) has recently been demonstrated with standby power of 60 nW (or ~7.3 fW/bit), while read 0, write 0, and write 1 operations required 210 fJ, 380 fJ, and 350 mJ, respectively. These values were determined for a 400 mV supply, but cells were operational at voltages as low as 250 mV [41].

Nonvolatile FeRAM integrated with CMOS appears to be an appealing technology to further reduce standby power for energy-harvesting applications [42], [43].

During periods of communication, the lens system would be located near a reader, which would provide additional power to communication-specific circuitry necessary to read and transmit stored data. Inductive coupling between an external loop antenna and an on-lens antenna could provide power and extract data in a manner similar to the Sensimed Triggerfish®.

## 1.4 Solar power for continuous contact lens sensors

Providing power to an autonomous contact lens system in intimate contact with the eye, a sensitive organ, is a major challenge. Carrying a transceiver for RF or inductive power would be cumbersome, while using a transceiver only occasionally would negate the many benefits of continuous sensing. Batteries could be used, but would either need to be recharged or implemented in single-use systems. Ideally, the system would harvest sufficient energy from the environment. The many reports on energy harvesting techniques for low power systems seem to indicate that photovoltaic generation is the most practical for this application [38], [44–47]. Some scavenging methods are simply not possible for use with contact lenses, such as generators operating on ambient airflow, push buttons, or ambulatory motion. Vibrational devices can generate power in the low $\mu W/cm^3$ range, although these require some moving parts, such as a magnet moving through a coil or a rotating proof mass that winds a spring. Thermoelectric generators produce tens of $\mu W/cm^2$, but require a temperature difference of several Kelvin that may not be available in temperate climates or office buildings. Light is readily available and can provide about 100 $mW/cm^2$ outdoors and 100 $\mu W/cm^2$ in a normal office. Therefore the best option for powering autonomous contact lens sensing systems is using photovoltaics.

Indoor spectra are much different than that of sunlight, which has a significant amount of ultraviolet and a somewhat smooth profile. Incandescent bulbs also have a smooth profile, but with peak intensity shifted up because of a lower temperature profile. Fluorescent lighting usually has several large peaks in an irregular spectrum that gives the impression of white light. For example, a florescent light bulb might have large peaks at 450 nm, 550 nm, and 600 nm. Indoors, on-lens solar cells could generate several microwatts of power, assuming ~0.5 $cm^2$ available area (i.e. contact lens area minus that of the pupil), ambient light of hundreds of $\mu W/cm^2$ [44], and power conversion efficiency of a few percent. In bright sunlight much more power would be available, even without staring at the sun.

Research in a variety of fields is directed at extremely low power, fully-functional, autonomous sensing systems powered by photovoltaic devices. For example, Smart Dust was developed to determine the feasibility of packing sensing, computing, and communication into devices on the order of a cubic millimeter for military uses, animal or insect tracking, inventory control, and product quality monitoring. Systems were comprised of batteries, solar cells, sensors, charge storage capacitors, readout and transmission circuitry, and photodiodes for data reception. In addition, active and passive data transmission was described, the former with a laser diode and beam steering mirror, and the latter with a modulated corner reflector. In 2001, a 63 $mm^3$ device was reported [48], and more recently a 16 $mm^3$ solar-powered node was described capable of ~12% power conversion efficiency and power output of 1.0 $mW/mm^2$ and 1 $\mu W/mm^2$ in full sunlight and bright indoor light, respectively [49].

Also, autonomous contact lens systems are conceptually similar to computational RFIDs (CRFIDs). CRFIDs communicate through backscattering, but also perform sensing, computation, and storage, and then transmit data instead of an identification number. Normally, CRFIDs require continuous RF power from a nearby reader to function, but recent focus has been directed toward making such systems autonomous by incorporating additional power sources. It has been demonstrated that solar energy harvesting can allow for sensing, data storage, and increased RF read range [50–52].

Some amount of additional circuitry is necessary when using solar cells as a power source. The output voltage of silicon solar cells ranges from a few tenths of a volt to a maximum of about 0.7 volts under different light levels. Stacking solar cells can provide higher voltages, but for reliable operation voltage converters and regulators would be necessary. It has been demonstrated that optimal conversion efficiency under different input voltage levels can be achieved through reconfiguration of charge pump circuits [53].

## 1.5 Summary

Autonomous contact lens sensors could be integrated into continuous health monitoring systems to provide data pertaining to a wearer’s health. Such devices would require at least several µWs for sensors, readout circuitry, and data storage, and photovoltaic devices are a plausible means of meeting this need. Before discussing solar cells, functional contact lens process development for single pixels displays, including improvements on lens substrate fabrication, component integration, and molding procedures, is covered in Chapter 2:. Chapter 3: describes solar cell theory, with emphasis on the mechanisms related to solar cell losses, as well as a review of relevant solar cells. Finally, the design, simulation, and fabrication of solar cells to conform to the shape of contact lenses is presented in Chapter 4:.

# Chapter 2: Contact lens process development

The major steps in active contact lens development are as follows: 1) microfabrication of substrates with antennas, electrical interconnects, sensor electrodes, and component receptor sites, 2) assembly of circuits and optical components, 3) and substrate molding.

## 2.1 Contact lens development overview

The substrate material for contact lenses was required to be optically clear, biocompatible, and thin. Also, because microfabrication on curved surfaces presents many challenges, processing was performed on planar, wafer-shaped substrates compatible with standard microfabrication equipment. Poly(ethylene terephthalate) (PET) was used because of good chemical resistance, thermal stability, transparency, and also because of its previous use with flexible electronics [54–56]. Although not ideal because of low oxygen permeability (diffusion constant $D \approx 4 \times 10^{-9}$ $cm^2/s$ [57]), it was sufficient to study the feasibility of creating systems on contact lenses.

The process used by Ho [7] was replicated and later modified and improved as necessary for different projects. The process developed by Ho anticipated a large number of LED pixels on a contact lens, and therefore metal bridges were incorporated to allow for close packing of LEDs. Standard 100 mm wafer-shaped discs with major and minor flats were cut from 25.4 cm x 25.4 cm x 100 μm sheets of PET (Policrom, Inc.) using a $CO_2$ laser cutter. After a standard solvent clean, AZ4620 (MicroChem Corp.) photoresist was spun and soft-baked at low temperature (65 ºC). Contact alignment and exposure was used with tank development in 4:1 deionized water (DI):AZ400K (MicroChem Corp.). An electron beam evaporated was used to deposit a metal layer stack of Cr/Ni/Au. This stack was used to provide good adhesion, an intermetallic when solder coating, and high conductivity for interconnects and good solder wettability. After metal evaporation, wafers were placed in acetone for approximately one hour and sonicated for an additional thirty seconds to facilitate lift-off. SU-8 2 was used as an insulation layer and for bridging, and then a second metal layer was sputter deposited and removed using the same lift-off procedure. However, the sputtering process was performed in steps to avoid substrate heating and warping. Next, SU-8 25 was used to create component receptor sites to restrict component movement during assembly and to protect exposed metal.

It should be noted that lift-off on PET, particularly using positive resists with low temperature bake steps, is not ideal for creating smooth metal edges, as positive photoresists usually have a positive sidewall. This problem is compounded when using sputter deposition as it normally is more conformal than evaporating. Additionally, wafers underwent some amount of warping during the metallization process which made alignment difficult. Therefore, feature sizes were kept larger than 25 µm, and masks were designed so functionality could be maintained with large and unavoidable alignment errors at the wafer periphery (>10 µm).

Assembly was based on methods presented by Stauth [56]. After fabricating substrates with contacts and receptor sites, exposed metal pads were coated with 47ºC In/Sn/Bi/Pd alloy using angled dip coating. Low temperature indium-containing solders are often incompatible with standard fluxes, which have significantly higher activation temperatures than those used during soldering. Also, solder fluxes often require special cleaning procedures and can have complicated chemistries that may or may not be toxic. Therefore, ethylene glycol (EG) with hydrochloric acid (HCl) was used in place of standard fluxes to remove surface oxides and promote wetting. Next, the solder coated substrates were placed at an angle in slightly acidic ethylene glycol that was heated to reflow the solder. Silicon transistors were flowed over the substrate (~100x per binding site) and self-assembled.

After assembly, planar structures were molded into the appropriate shape and coated with parylene, a biocompatible and conformal polymer. The remainder of this chapter is devoted to the methods, iterations, and various improvements on the processes described above, in chronological order from the first operational molded structure and ending with a wirelessly-powered single pixel lens that was tested *in vivo*.

## 2.2 System 1: Molded lens with red LEDs and dummy silicon components

PET was used as a flexible substrate for electronics, but to the authors knowledge it had never been spherically molded with working components. Therefore, an initial goal was to show that various components could be assembled on a planar structure and molded while maintaining electrical conductivity and component functionality. Components chosen for this experiment were red LEDs (described in detail in [58]) and small silicon chips with simple metal traces. Current from test probes would travel along the substrate interconnects, through solder connections and into traces on the silicon components, then back onto substrate interconnects and through assembled LEDs to create bright red emission.

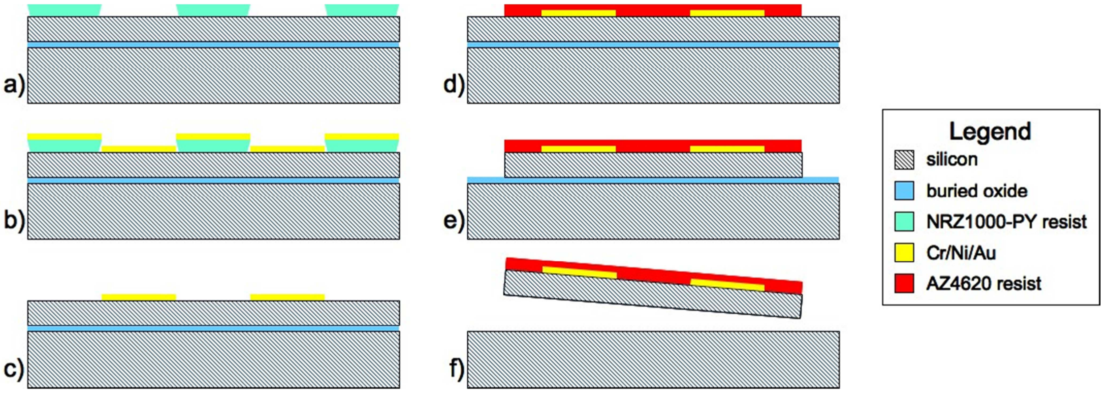

**Figure 2. Silicon dummy component fabrication process. This process was used for two types of dummy components, one with arbitrary metal lines and contact sizes, and a second with specifically placed electrical contacts mirroring functional integrated circuits.**

Thin silicon components were fabricated using SOI wafers in the follow manner. First, a negative lift-off resist (NRZ1000-PY, Futurrex) was patterned using contact lithography (Figure 2, a). With a single coat and appropriate exposure dosing, this resist displays a strong negative sidewall conducive to easy lift-off with clean, rectangular metal cross sections. (However, high temperature bake steps are also required, which is the reason it was not used with PET.) A Cr/Ni/Au metal layer was deposited using electron beam evaporation (Figure 2, b), and a short acetone soak and sonication removed unwanted metal (Figure 2, c). Then AZ4620 was patterned to define component shapes, in this case 500 x 500 µm squares (Figure 2, d). The silicon device layer was etched to the buried oxide using deep reactive ion etching (DRIE) (Figure 2, e), and then chips were released from the handle wafer in hydrofluoric acid (Figure 2, f). After release, chips were rinsed, collected, and soaked in photoresist stripper at 90 °C. They were again rinsed in deionized water and finally stored in glass vials for later use. PET substrate fabrication (the bulk of the contact lens) was nearly identical that described above by Ho, except that the second metallization was a single layer of chromium used to keep solder from wetting test pads.

To assemble red AlGaAs LEDs and silicon dummy chips, a pseudo self-assembly process was used; components were placed in receptor wells manually, but accurate alignment was provided by capillary forces of the molten solder. First, the 47 ºC solder was immersed in EG in a 100 mL beaker, and heated on a hotplate set to 225 ºC. The solder would take about 20 minutes to fully melt, during which time, a solution of 25 mL of EG and 10 µL of HCl was prepared in a petri dish and set on different hotplate under a stereo microscope. When the solder fully melted, 60 µL of HCl was added to remove any surface oxidation that had formed on the solder. Immediately after adding the acid, the beaker was carefully lifted off the hot plate and partially lowered into an ultrasonic bath. Immediately, so as to not allow significant cooling, the contact lens substrate was dipped at an angle, removed quickly, and placed in the previously prepared petri dish.

Silicon dummy chips and micro-LEDs were placed on the contact lens in corresponding SU-8 25 wells using a glass pipette while viewed through the stereo microscope. The petri dish was heated to melt the solder, at which time components self-aligned and were electrically and mechanically connected to the substrate metal traces. The petri dish was removed from the hot plate approximately thirty seconds after chip alignment. After cooling for five minutes, contact lenses were removed from the EG solution, soaked in isopropyl alcohol (IPA), rinsed with IPA, and dried with nitrogen.

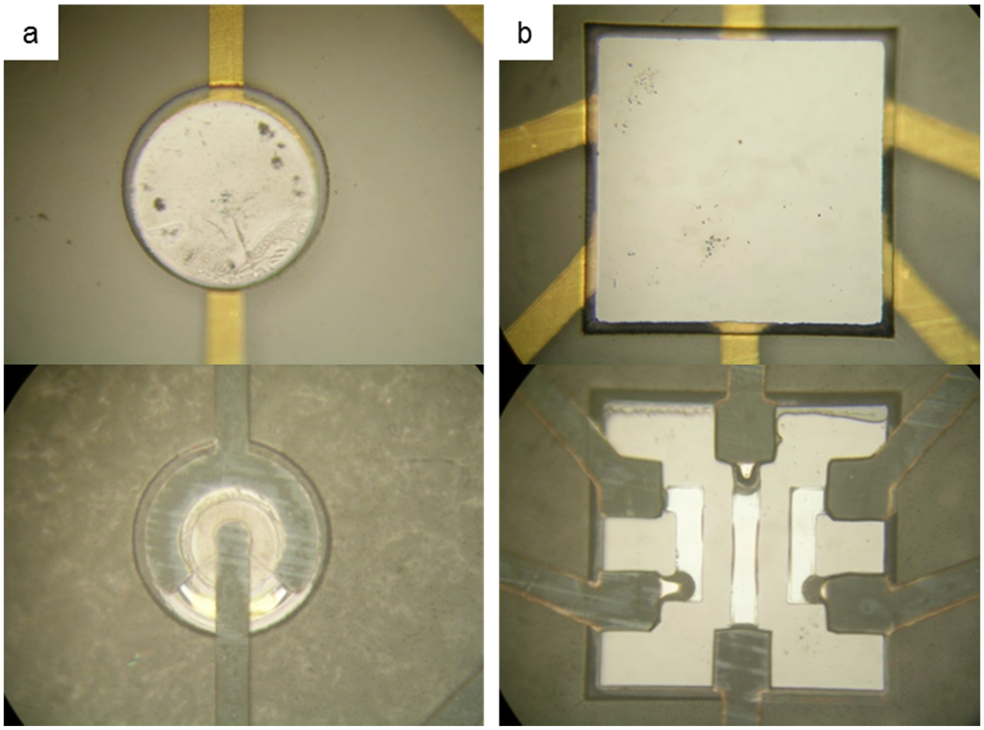

**Figure 3. Assembled components. a) Assembled red LED viewed from above (top) and through the transparent substrate (bottom). b) Assembled silicon dummy component viewed from above (top) and through the transparent substrate (bottom). Solder can be seen extending along the traces of the silicon chip.**

Next, a hemispherical aluminum mold was used (radii ≈ 7.1 mm convex and 7.225 concave, to account for the lens thickness) to obtain a curvature appropriate for New Zealand White Rabbits. Essentially, the substrate was a bilayer polymer structure with 100 μm of PET underneath 25 μm of SU-8, each with different glass transition temperatures. The glass transition temperature of PET is dependent on manufacturing and previous thermal treatments. The temperature at which SU-8 flows is also dependent on processing (i.e. UV exposure, baking time and temperature, etc. [59]). Therefore, molding was carried out from 150 ºC to 220 ºC to empirically determine the best operating temperature. At temperatures below 180 ºC, the structure would either wrinkle badly or it would not hold its shape when removed from the mold. At 190 ºC and 200 ºC, molding produced smooth surfaces that retained their structure, provided the lens was allowed to cool sufficiently (<80 ºC) before being removed from the mold. If the structure was removed prematurely, it would flatten significantly. At 210 ºC, and even more so at 220 ºC, the SU-8 layer seemed to flow and take on the micro-scale imperfections of the mold. All further molding of PET/SU-8 structures was performed at 200 ºC.

Lastly, a layer of parylene-C (~10 µm, Specialty Coating Systems, PDS 2010 Labcoater® 2) was conformally deposited over the contact lens for biocompatibility and mechanical strength. The contacts lenses were sterilized in ethanol for 10 minutes and stored in a saline solution prior to testing on animals. To test the fit, parylene coated lenses were placed on New Zealand White Rabbits under general anesthesia in the University of Washington vivarium. *In vivo* studies were performed according to the guidelines of the National Institutes of Health for use of laboratory animals, and with the approval of the Institute of Animal Care and Use Committee of the University of Washington (Protocol # UW4139-01). Female New Zealand White Rabbits (mean wt. 2.5kg) underwent general anesthesia with 5% induction of isoflurane and oxygen, which were maintained at 2% during the studies. Artificial tears were applied frequently to insure hydration. Prototype contact lenses were well-fitted to the rabbit ocular surface (Figure 4d), but moved around on the eye significantly.

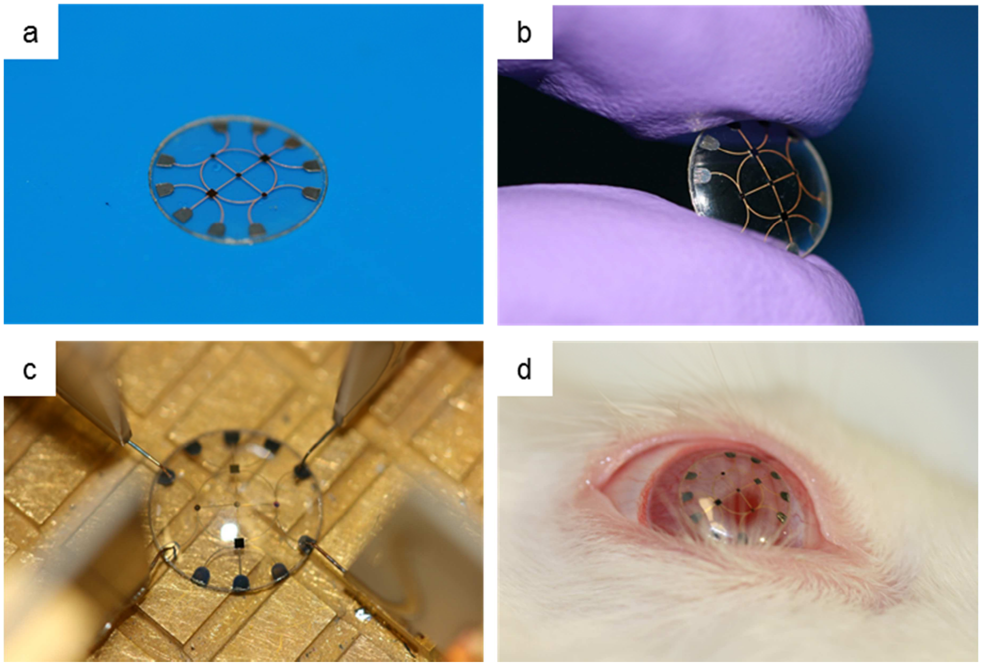

**Figure 4. System 1 results. a) Planar device with three LEDs and two dummy silicon components. b) Molded structure. c) System 1 testing. LEDs could be tested directly or by passing current through one or two dummy silicon chips, depending on which test pads were probed. d) Molded and parylene coated device on anesthetized rabbit.**

## 2.3 System 2: Single red pixel and wire-bonded integrated circuit

The first fully functional powered devices comprised metal loop antennas, interconnects, custom integrated circuits, and single red AlGaAs LEDs. An external transmitter sent RF radiation at ~1 GHz that was collected by the on lens loop antenna and fed into a small, custom integrated circuit (~450 µm x 480 µm) for the purposed of rectification, voltage multiplication, and LED duty cycling.

For fabrication of the substrate, a single metal layer process with two SU-8 layers was used (Figure 13, Process 1). However, because of GHz transmission and the skin depth of Au at those frequencies, it was determined that a thicker Au layer would improve the antenna performance. Therefore, Au thickness in the metal stack was increased to 1 µm from the previous thickness of 150 nm. Additionally, during this fabrication sequence it was discovered that a short oxygen plasma step directly before evaporation significantly increased metal adhesion to the PET, allowing for long ultrasonic agitation to remove unwanted metal. Otherwise, large vertical Au spikes on the edges of metal lines of approximately the photoresist height were unavoidable, but expected because of the suboptimal low temperature, positive resist lift-off process. However, with increased adhesion, longer ultrasonic agitation could be used to minimize this problem. Therefore, just prior to metal evaporation, wafers were plasma cleaned in a Branson barrel etcher for 3 min at 300 W.

Although LED assembly was identical to that previously described (i.e. manual placement and subsequent heating in a petri dish), the solder coating process was altered significantly. First, because of health concerns and the trend away from lead-containing solders, a lead-free solder (Indium Corp., Indalloy 19, In/Sn/Bi) with a slightly higher eutectic temperature of 60 ºC was used in place of the 47 ºC alloy. Additionally, the dipping procedure was altered because manual dipping introduced significant and unavoidable variability: difficulty in controlling solder temperature, dip angle, dip speed, and energy transferred to the beaker because of standing waves in the ultrasonic bath, for example. In response to these problems and the ensuing poor reliability (see Figure 5), an apparatus to more systematically control the dipping was designed, consisting of a linear actuator, ultrasonic agitator, beaker holder, and tweezer holder (see Figure 6).

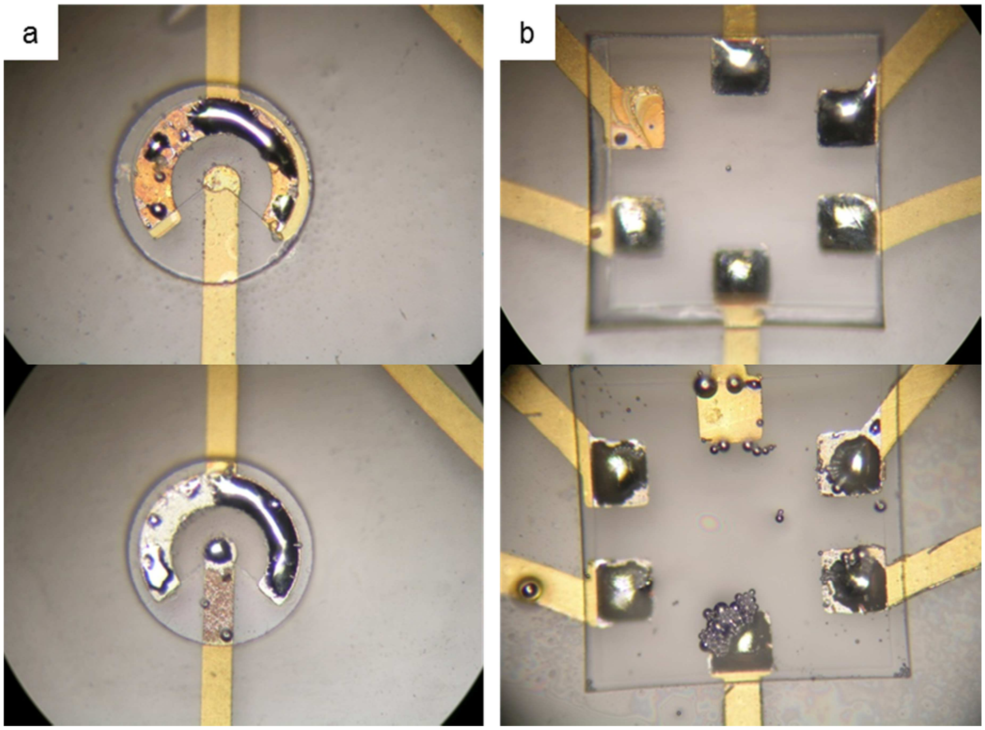

**Figure 5. Examples of poor solder coating. Solder coating was very unreliable using manual methods because of difficultly controlling any of the variables affecting the coat, such as temperature, dip time, removal speed, etc. a) Poorly coated LED assembly sites. b) Poorly coated dummy silicon assembly sites.**

After failing to hold the solder beaker partially suspended in the ultrasonic bath with a coil of wire and later a U-bracket, a piece of ¼” plastic was laser cut in the shape of the sonicator lid with a hole slightly larger than the beaker diameter removed from its center. This method ensured that the solder beaker was in exactly the same position every time, and allowed for more dips because the water temperature was maintained for a longer duration. Otherwise, the ultrasonic bath, set to the maximum (69 ºC), would only maintain a water temperature of 47 ºC, cooling the solder quickly and eliminating the possibility of performing many experiments without refilling the hot water. The linear actuator was later attached to a locking hinge that could be adjusted in increments of ten degrees.

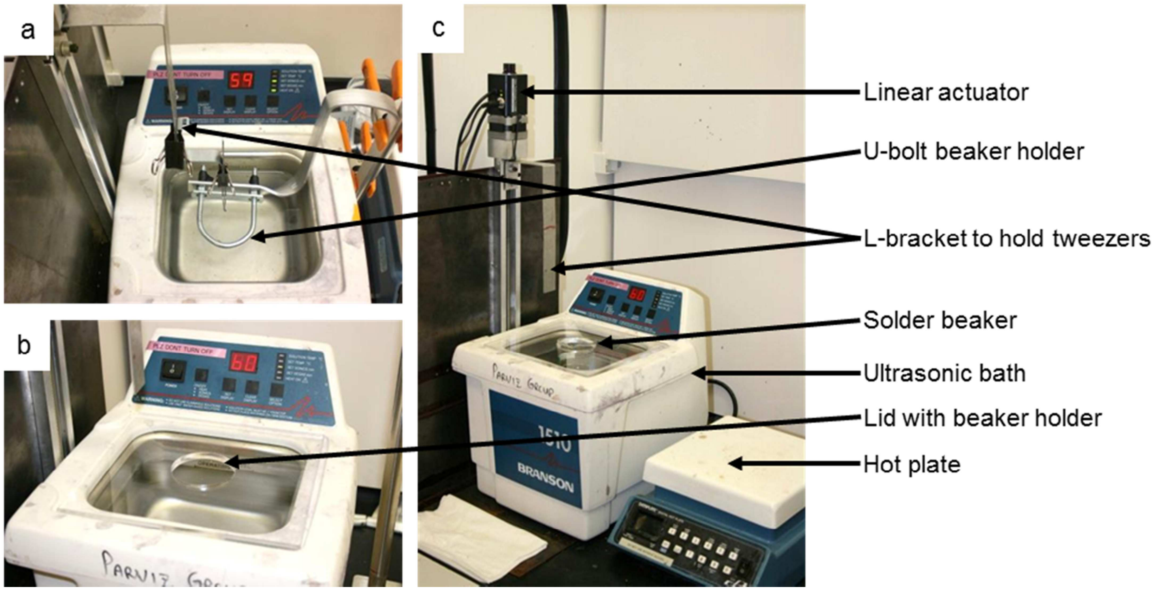

**Figure 6. Solder dipping setup. a) Initial setup with a U-bracket to hold the solder beaker, that was later replaced by a custom lid with a hole cut for a 100 mL beaker (b). c) Entire setup, showing dipping assembly, ultrasonic bath and beaker holder, and hotplate to melt solder. Later the linear actuator was mounted to a locking hinge adjustable in ten degree increments.**

Using this dip setup, solder coating of Au circles on PET and Au circles surrounded by Cr were tested extensively with special templates. Each test template had 100 circles, with sizes ranging from 10 to 100 µm. Templates were dipped vertically and at ten and twenty degrees from vertical. Removal speeds were 366.2, 732.4, 1098.6, and 1464.8 µm/s. These seemingly random linear speeds corresponded to integer values used in the scripting language for rotational speed. The absolute coverage for 32 different dips (3200 circles) was measured, and it was determined that pad sizes down to 60 µm could be coated with near 100% coverage using this dipping method. Also, the average height for solder bumps was measured using an optical profilometer for a single test template, dipped at ten degrees (Table 1).

**Table 1. Solder bump heights for coating Au circles.**

| Approximate Height [µm] | | | | | | | | | | |
|---|---|---|---|---|---|---|---|---|---|---|
| Pad size [µm] | 100 | 90 | 80 | 70 | 60 | 50 | 40 | 30 | 20 | 10 |
| Pad #1 | 25.3 | 22.9 | 21.4 | 20.9 | 17.8 | 15.6 | 13.4 | 10.8 | 9.4 | 6.9 |
| Pad #2 | 26.2 | 23.9 | 20.9 | 20.1 | 18.8 | 15.6 | 13.2 | 10.6 | 4.4 | 1.8 |
| Pad #3 | 24.3 | 23.5 | 21 | 18.7 | 18.3 | 15.3 | 13.3 | 11.2 | 6.8 | 6.4 |
| Pad #4 | 26 | 22.6 | 22.6 | 19 | 16.9 | 15 | 13.5 | 10.5 | 9.1 | 2.4 |
| Pad #5 | 26.4 | 22.2 | 21.6 | 19.8 | 18.4 | 15.6 | 13.7 | 10.4 | 7.9 | 1.5 |
| Pad #6 | 26.1 | 19.5 | 21.1 | 19.6 | 18 | 14.9 | 13.7 | 11.8 | 6.2 | 2.9 |
| Pad #7 | 25.3 | 21.7 | 21.2 | 19.7 | 18.2 | 15.9 | 12.6 | 10.9 | 9.2 | 6.6 |
| Pad #8 | 26.1 | 23.5 | 21.2 | 20.2 | 17.8 | 15.3 | 13.6 | 11.4 | 9.4 | 6.6 |
| Pad #9 | 26.1 | 23 | 20 | 19.8 | 18.8 | 15 | 12.9 | 11 | 9.1 | 6.3 |
| Pad #10 | 26.2 | 25.3 | 21 | 20.1 | 18.5 | 15.3 | 12.4 | 10.9 | 9.5 | 6.7 |
| Average [µm] | 25.8 | 22.81 | 21.2 | 19.79 | 18.15 | 15.35 | 13.23 | 10.95 | 8.1 | 4.81 |

Although red LED assembly was exactly the same as before, the process to attach the custom IC was altered. Contact pads on the custom ICs were aluminum, which could not be directly coated with low temperature solder. Therefore, the LED was assembled first and then the substrate was molded. Finally the IC was epoxied in place pad-side-up on the molded lens and wire-bonded to the substrate. This device was operational, but the reliability and efficiency were poor, in part because of the exposed wire bonds the bond wire inductance.

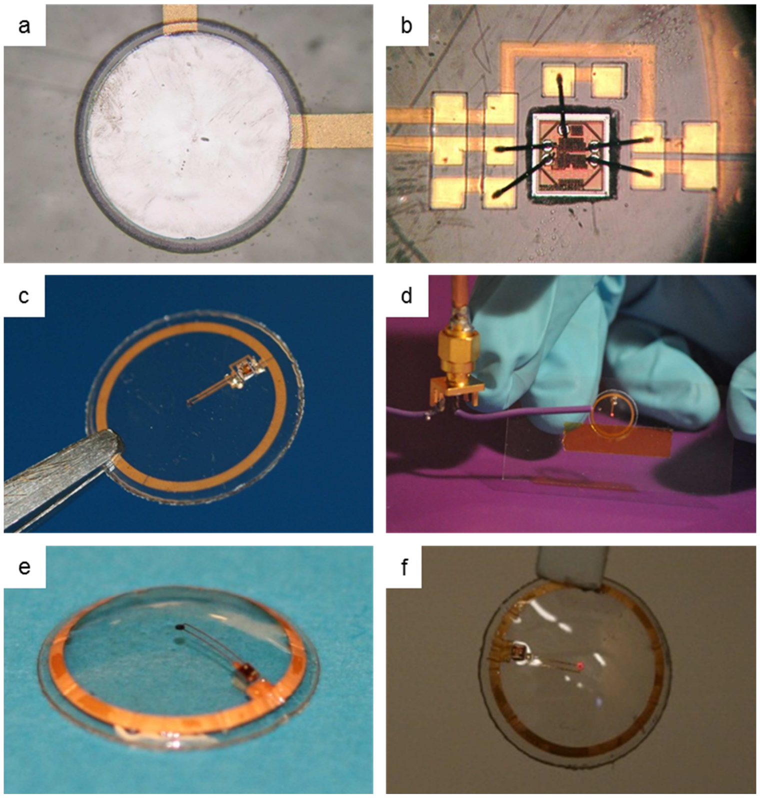

**Figure 7. System 2 results. a) Assembled AlGaAs LED. b) Wire-bonded custom IC. c) First, a planar device was assembled and powered with a dipole antenna (d). e) Later a device was molded and tested in the same manner (f). The LED can be seen lit in the center of the contact lens in (d) and (f).**

## 2.4 System 3: Electroplated antenna and flip-chipped IC

Although there were several intermediate systems with layout changes, the next major developments were the addition of a thick electroplated gold layer to the substrate fabrication process, and the exchange of red LEDs for more efficient blue InGaN LEDs (described in [60], [61]). Also, to address problems associated with bond wires, a flip-chip method was employed to remove bond wire inductance, decrease contact resistance, and improve yield after molding.

Although 1 µm Au lift-off was possible, it was not ideal because of poor Au cross sections, the long evaporation time required, and loss of Au to the chamber. Therefore, the next progression in the substrate process was the addition of an electroplated Au layer to further increase the antenna thickness, decrease the resistance and improve efficiency (Figure 13, Process 2). Initially, a Cr/Ni/Au seed layer was deposited over the whole wafer, then the antenna and interconnects were electroplated, and finally the seed layer was etched. However, catastrophic adhesion failure was observed after even a very short Cr etch (Figure 8).

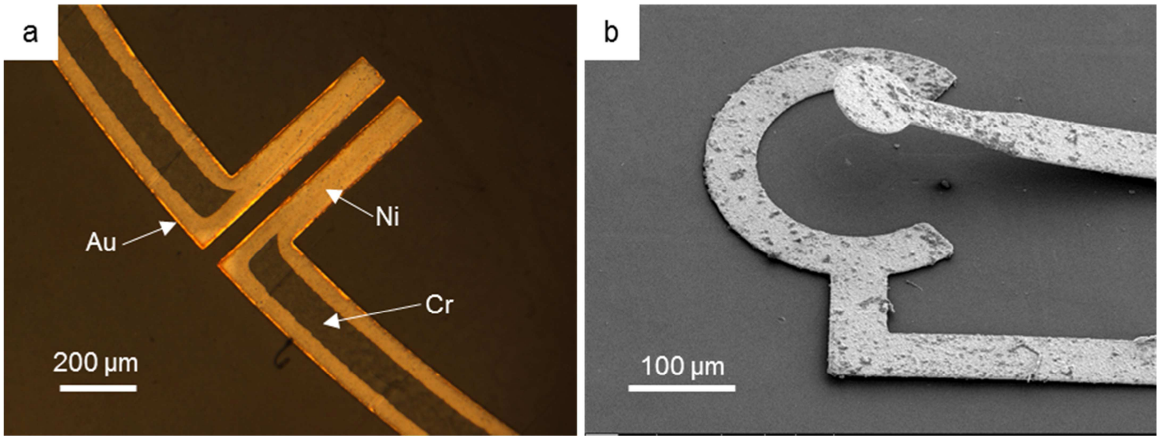

**Figure 8. Catastrophic adhesion failure after a short Cr etch observed during the first attempts at creating electroplated metal antennas. a) Slight nickel undercut and significant Cr undercut was observed, resulting most likely from a combination of poor Cr/PET adhesion and stress in the plated gold. b) Poor adhesion resulting in an electrode peeling off of the substrate.**

To solve this problem, a single metal layer comprising all the necessary electrical interconnects and an antenna that was slightly smaller in width than the final antenna were deposited. Then, SU-8 2 was deposited, followed by a thin (~40 nm) seed layer of Au across the entire wafer. The electron beam evaporation system, using a rotating planetary that changed the substrate angle continually, provided for reasonable sidewall coverage necessary for electrical connection over the SU-8 2 features during electroplating. Then, AZ4620 was spun at slow speed (1500 rpm) to pattern the final dimensions of the antenna, and ~5 μm of Au was electroplated using a pulsed process (1 ms on, 1 ms off) in a cyanide-based Pur-A-Gold® 401 formulation (Enthone-OMI Inc.). Then the seed layer, this time only Au, was etched, resulting in thinner interconnects (~400 nm) and a thick (~5 μm) antenna. The interconnect Au layer thickness was significantly larger (~400 nm) than the seed layer (~40 nm) to ensure that seed layer etching would not remove all the Au. This substrate fabrication process, described in detail in Appendix A:, was used in [9], [10].

After completing microfabrication, the $CO_2$ laser cutter used to cut out individual contacts would generally leave rough edges. To minimize this effect, laser cutter parameters were optimized and 5 µm grit aluminum oxide sandpaper was used to polish the edges. The sanding process was done prior to chip and LED assembly to avoid damaging or dislodging components and also because it generated some amount of dust-like polymer that required removal with a solvent clean.

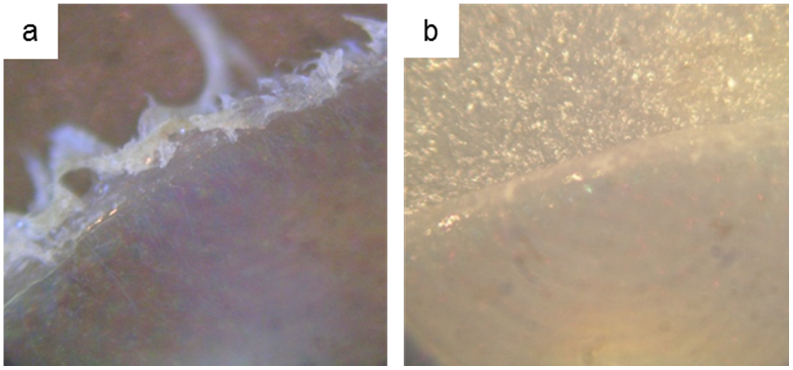

**Figure 9. Magnified view of a contact lens edge prior to (a) and after (b) optimization of laser cutter parameters and polishing.**

Instead of wire bonding, the integrated circuit for this system was flip-chipped directly on the substrate in the manner previously described to assemble dummy chips and red LEDs. Prior to solder coating, the custom silicon IC aluminum pads (from MOSIS) were electrolessly plated with Ni and Au (CV Inc.). Although this metallization scheme worked successfully in previous work, the standard method of solder coating only the substrate pads, placing the chip, and melting the solder did not produce any operational devices. If pressure was applied when the solder was molten, it would flow across the pads and cause connections to short. A solution to this problem was to cover the pads on the chip and the substrate separately, and then perform reflow in acidic EG in the usual manner.

To cover the chip pads, manual angled dipping with the sonicator and a pair of small tweezers was attempted. Although solder coating was not reliable, when chip pads coated adequately there was always good connection between chip and substrate. To improve solder coating, the chip was held with a pair of tweezers and a glass pipette was used to flow molten solder over the chip. This very simple procedure produced outstanding results and high repeatability, and eventually became the method of solder coating the substrates. The final procedure for solder coating substrates and ICs is described below.

First, 60 ºC solder was covered with 10 mL EG in a 100 mL beaker and heated. In order provide more even heating (previously several beakers broke because of uneven solder expansion), the 100 mL solder beaker was placed in a small evaporating dish filled with water, and then both beakers were placed on a hotplate set to 225 ºC (Figure 10a). After the solder fully melted (Figure 10c), the dirty EG was carefully removed by pipette (Figure 10d), and 10 mL of fresh EG was poured over the molten solder. Then 60 µL of HCl was added (Figure 10e), and molten solder was pipetted over the substrate and chip (Figure 10f). Using this method, the solder would remain at the proper temperature (~95 °C) as long as the water level was kept sufficiently high. After some time, the solder surface would again lose its luster, at which time the EG could be removed, replaced, and refreshed with HCl. This process could be repeated indefinitely.

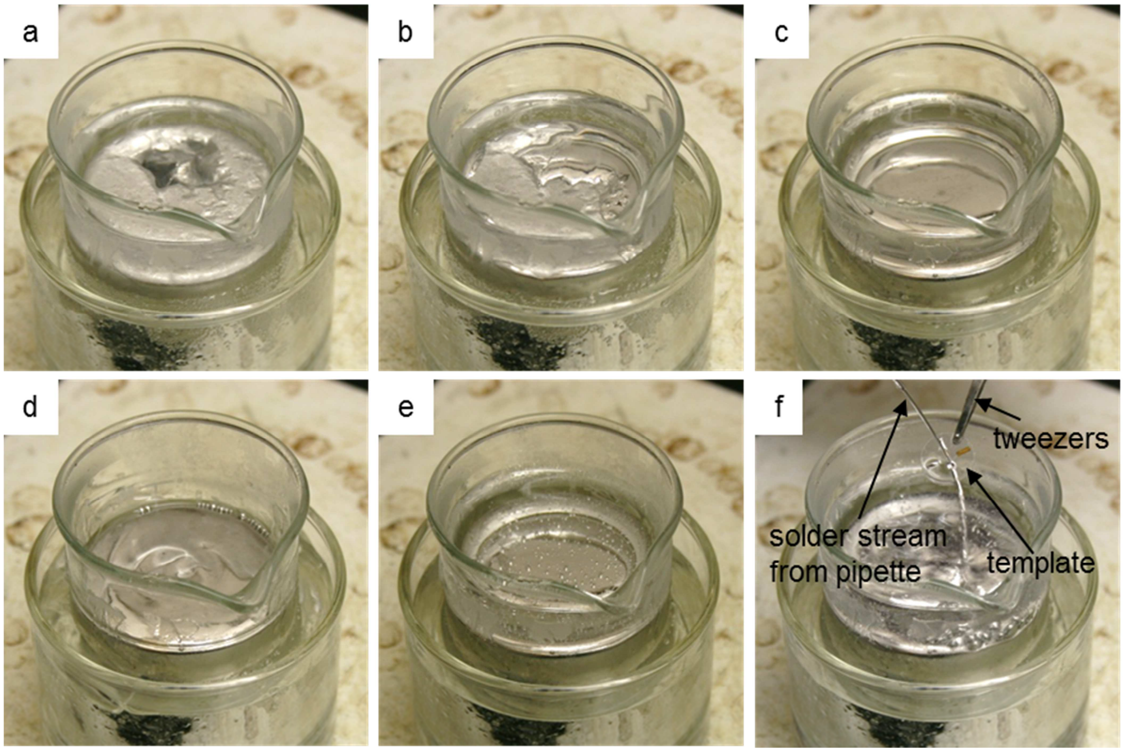

**Figure 10. Final solder coating process. Boiling water in the outer beaker maintained the solder and overlying ethylene glycol at ~95 °C. a) Solid solder in a 100 mL beaker, placed in a second beaker filled with water. b) Partially melted solder. c) Fully melted solder. d) After removing dirty ethylene glycol. e) After adding 10 mL of fresh ethylene glycol and 60 µL HCl. f) Templates were coated with solder by pipetting molten solder across a template. Here, three out of four large Au pads were coated for easy visibility.**

When molding devices that comprising flip-chipped integrated circuits, the concave side of the mold could not be used without moving or breaking the integrated circuits. This was because ICs were ~250 µm thick, and the mold was designed so that the gap between the bottom and top surfaces was ~125 µm, allowing for the thick SU-8 as well. To solve this problem, a small hole was drilled through the center of the convex mold and exited the side, which was connected to a vacuum line to hold the lens in place. Next, the convex mold and a metal ring were heated on hotplate set to 200 ºC. The vacuum was pulled, and the contact lens was centered on the convex mold. The mold was placed on an insulating surface, and the ring, having an inner diameter slightly less than the contact lens, was used to slowly press and shape the lens without disturbing the components. After cooling, the contact lens was removed from the mold, cleaned with IPA, and dried with nitrogen.

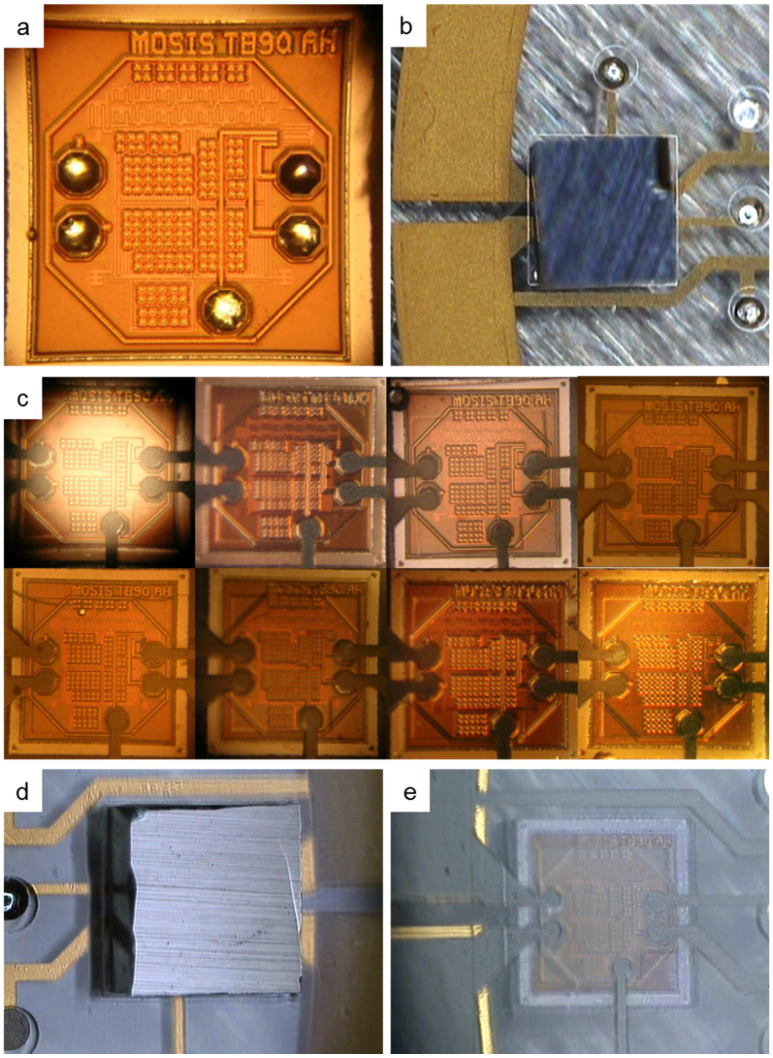

**Figure 11. Integrated circuit flip-chip results. a) Soldered chip (450 µm x 480 µm in area and 250 µm thick). b) Assembled chip with electroplated antenna shown to the left. Notice that the chip can be placed very close to the antenna. c) Eight different trials of flip-chipping with both the chip and the substrate soldered, showing extremely good alignment to the substrate interconnects. After molding, the device remained in place with accurate alignment, shown from the top in (d) and through the substrate in (e).**

For this device, wireless activation of an on-lens LED was accomplished using 1.05 GHz transmission in free space. The transmit antenna was an SAS-571 double ridge guide horn antenna (A.H. Systems, 700 MHz – 18 GHz) fed with a +25 dBm signal. The contact lens was held using polymer tweezers and oriented with the maximum directivity facing the horn antenna. For a small loop antenna, the maximum directivity and loop are coplanar. Under these conditions, the LED was brightly lit and visible to the naked eye at ~10 cm. In free space using a +35 dBm signal, the LED could be activated at distances of ~1.0 m, as measured from the horn antenna mouth.

Tests on a rabbit cadaver eye showed activation of the LED at ~10 cm from the horn antenna and +35 dBm input power, again at 1.05 GHz. However, when a saline film was applied to the top of the lens, the frequency changed significantly (~1.05 GHz to ~1.8 GHz) and the operational range decreased. To see the LED brightly lit, a dipole antenna was used at close range (~2.0 cm). In this setup, the LED could be activated in a larger frequency range (~0.8 to 2.0 GHz). The larger frequency range and closer operational distance suggests a more inductive link. Table 2 summarizes test conditions and results.

**Table 2. Summary system 3 of test results.**

| Test platform | Transmit antenna | Input power | Frequency [GHz] | Operating distance |
|---|---|---|---|---|
| Free space | Horn | +25 dBm | 1.05 | 10 cm |
| Free space | Horn | +35 dBm | 1.05 | 1 m |
| Rabbit cadaver eye, w/o saline film | Horn | +35 dBm | 1.05 | 10 cm |
| Rabbit cadaver eye, with saline film | Horn | +35 dBm | 1.8 | 1 cm |
| Rabbit cadaver eye, with saline film | Dipole | +35 dBm | ~0.8 – 2.0 | 2 cm |
| Live rabbit eye | Dipole | +35 dBm | ~0.8 – 2.0 | 2 cm |

Next, lenses were tested on a rabbit under general anesthesia in the same manner described previously (Figure 12b). The effects of wearing the contact lens display were tested using portable slit lamp biomicroscopy and pachymetry. Additionally, topical fluorescein was applied to the corneal surface using a dropper and the eye was visually examined for corneal abrasions, thermal burns or corneal edemas as a result of *in vivo* testing. Such damage would result in corneal surface roughness, causing the fluorescein to accumulate. A healthy corneal epithelial layer after testing is displayed in Figure 12c, showing no fluorescein streaks or cloudiness.

All active systems described above were powered by RF transmission. The ICNIRP has a basic requirement for exposure of the head and trunk for the general public of 2 $Wkg^{-1}$ (up to 10 GHz), or a plane wave power density of 10 $Wm^{-2}$ (2 – 300 GHz) [62]. The IEEE Standard C95.1-2005 places exposure limits at 2 $Wkg^{-1}$ (100 kHz – 3 GHz) or 10 $Wm^{-2}$ (2 GHz – 100 GHz) [63]. Research contained in the IEEE standard and a recent ICNIRP review [64] point toward thermally induced cataracts as the primary biological concern. RF transmission requires a nearby transmitter, and therefore is not ideal for creating a system for continuous health monitoring.

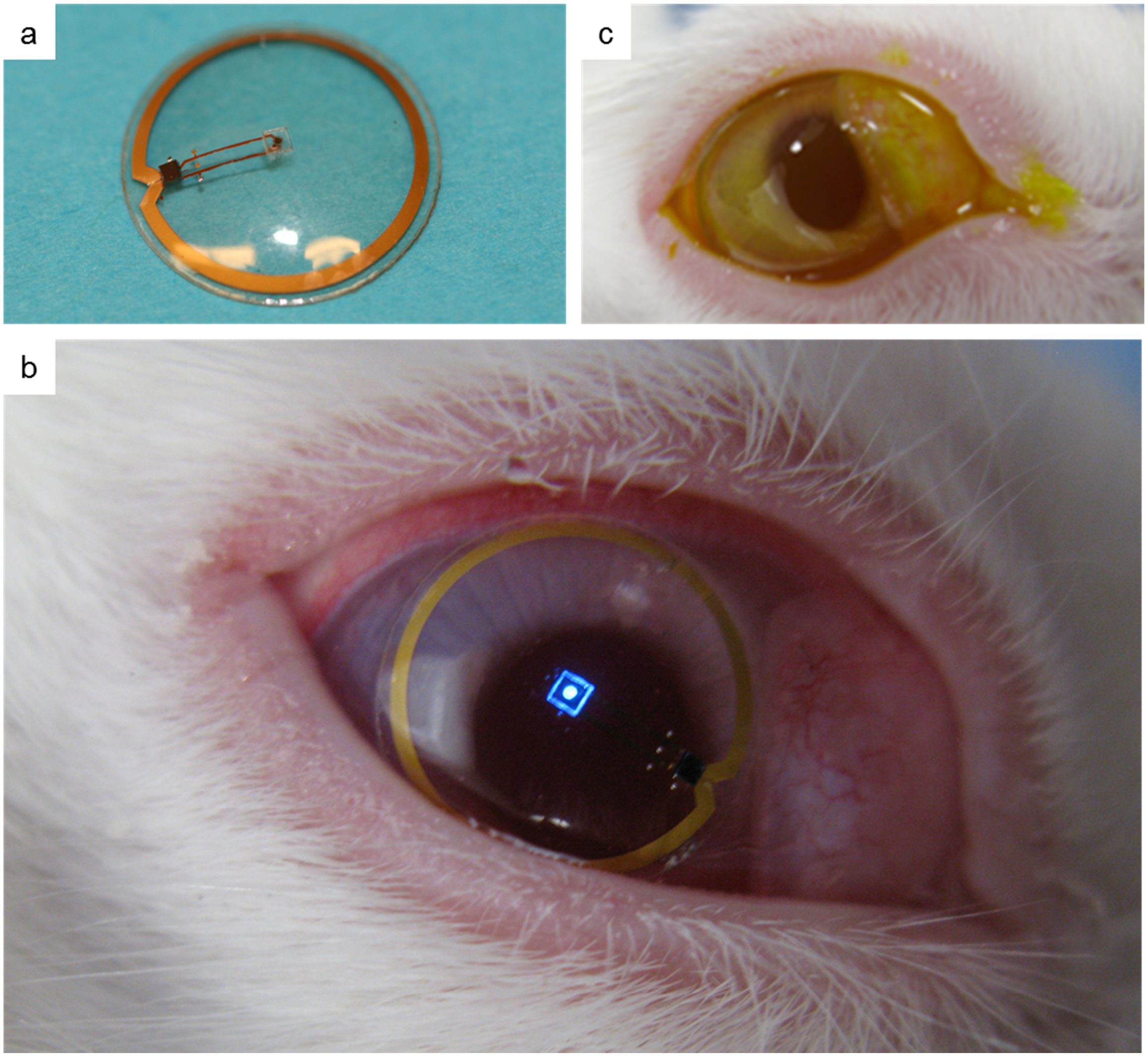

**Figure 12. Wireless activation of a contact lens display on a live rabbit. a) Photograph of a completed contact lens system. b) The contact lens display was placed on the eye of a live rabbit and powered by a dipole antenna, resulting in bright blue emission from the on-lens pixel. The micro-LED indicator was activated periodically and remained *in vivo* for up to 40 minutes. c) Subsequent tests using fluorescein showed no corneal epithelial damage.**

Although the system could be powered in free space from ten centimeters, operating distances on the rabbit eye were reduced to the cm-range. Matching, interface, and absorption losses were likely causes of the limited operational distance. Improvements could be made by reducing matching losses and ensuring that power received by the contact lens was maximized at the frequency of best antenna-to-chip matching.

## 2.5 Summary of process development

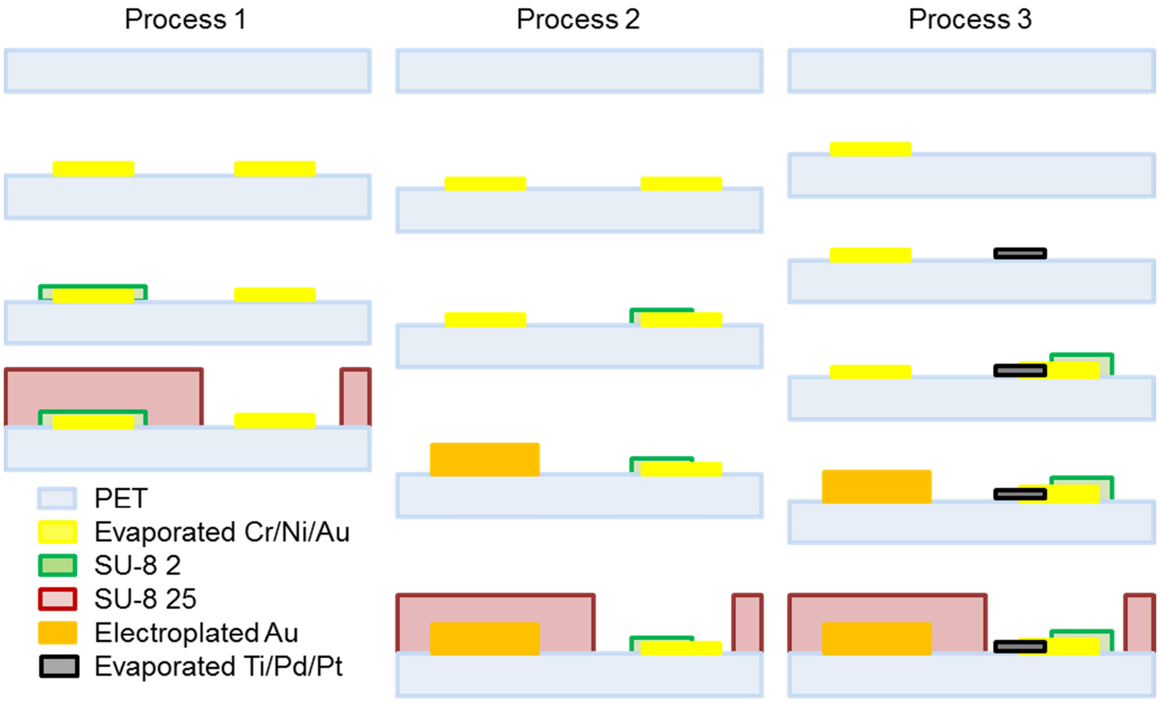

**Figure 13. Evolution of substrate fabrication processes.**

The first contact lens substrate consisted of a PET template with a single metal layer and two SU-8 layers (Figure 13, Process 1). Silicon components and red LEDs were assembled, then the device was molded, and finally it was coated with a biocompatible polymer layer. Next, the antenna metal thickness was increased with an electroplated Au layer, and soldering techniques were improved so that ICs could be flip-chipped (Figure 13, Process 2). The last major addition to the substrate fabrication process was to add another metal layer for enzymatic sensor electrodes (Figure 13, Process 3). Here, directly after the first Cr/Ni/Au metallization, a second lift-off was performed, but with a Ti/Pd/Pt stack. The Cr/Ni/Au was deposited first, because the electrical contact would be better than if Cr/Ni/Au was placed atop oxidized Pt. This process was used in [34].

# Chapter 3: Solar Cell Theory

The sun is a large fusion reactor, in which hydrogen is converted to helium while releasing energy. The temperature of the surface of the sun is about 5900 K, and its emission is approximately that of a blackbody due to the ionization and broadening of atomic spectral lines. Some light emitted by the sun hits Earth and is partially absorbed by various gases (primarily oxygen, water, and carbon dioxide) before reaching planet surface.

Solar cells are devices illuminated by light from the sun to produce electrical power. A primary distinction between a photodetector and solar cell is that the latter generates power and is connected to an appropriate load, while the former is normally kept under reverse bias and used to detect an optical signal. The majority of current solar cell research is directed at decreasing the cost per watt to compete with traditional energy sources. One main route is to reduce material costs by using less high-quality silicon or using lower quality, cheaper silicon. Another is to improve efficiency, but often this is accomplished with an increase in processing complexity and cost.

Placing solar cells on contact lenses presents different challenges. Here, the total output power is of concern, as well as how well the devices conform to a contact lens, while cost and complexity are not necessarily major factors. Contact lenses are typically made from organic polymers, so it might seem logical to use organic solar cells. However, they are typically made using compounds that are not biocompatible and have low efficiency [65]. Therefore, silicon solar cells were determined to be the most practical for contact lenses.

## 3.1 PN diode

To understand silicon solar cells, it is necessary to first understand silicon pn junctions. This topic is covered thoroughly in semiconductor physics textbooks. Derivations shown in [66], [67], and [68] were used for the following sections. When a p doped region is in intimate contact with an n doped region, electrons from the n region will diffuse into the p region, leaving behind positively charged, stationary atoms.

Similarly, holes from the p region will diffuse to the n region, leaving behind stationary negatively charged atoms. These stationary charges create an electric field that opposes additional diffusion, and eventually an equilibrium condition is reached in which the electric field formed exactly counters diffusion. The area containing fixed charges and a strong electric field is called a space charge region (because of the fixed charges) or a depletion region (because mobile carriers are readily swept out).

At equilibrium with no external connections, the Fermi energy level of the device is flat. However, because the Fermi level of the p and n regions are different in relation to the vacuum level, the valence and conduction bands bend through the space charge region to maintain equilibrium. Thus, the amount of band bending, or the built-in voltage $V_{bi}$, is determined by difference between the p and n extrinsic Fermi levels and the intrinsic semiconductor Fermi level, which are given by

$$|\phi_{Fn}| = \frac{kT}{e}\ln\left(\frac{N_d}{n_i}\right), \text{and} \qquad \textbf{3.1}$$

$$|\phi_{Fp}| = \frac{kT}{e}\ln\left(\frac{N_a}{n_i}\right), \qquad \textbf{3.2}$$

where $k$ is Boltzmann's constant, $T$ is temperature, $e$ is the elementary charge, $n_i$ is the intrinsic carrier concentration, $N_d$ and $N_a$ are the donor and acceptor concentrations, and $\phi_{Fn}$ and $\phi_{Fp}$ represent the potential difference between the extrinsic Fermi levels and the intrinsic semiconductor level. Therefore, the total band banding is $|\phi_{Fp}| + |\phi_{Fn}|$

$$V_{bi} = V_t \ln\left(\frac{N_a N_d}{n_i^2}\right), \qquad \textbf{3.3}$$

where $V_t$ is the thermal voltage $kT/e$. This function relates the device built-in voltage to the device doping concentrations and allows determination of the relative concentrations of carriers across the junction. Assuming complete acceptor ionization and using the Law of Mass Action, expressions for the equilibrium concentration of majority carrier holes on the p side ($p_{p0}$), as well as the minority carrier holes on the n side ($p_{n0}$) are given by

$$p_{p0} \approx N_a \text{ and } p_{n0} \approx \frac{n_i^2}{N_d}.$$

By substituting these into equation 3.3, an expression is found for the minority carrier concentration (equilibrium hole concentration on the n side, $p_{n0}$) in terms of the built-in voltage and the majority carrier hole concentration (equilibrium hole concentration on the p side $p_{p0}$):

$$p_{n0} = p_{p0} \exp\left(\frac{-V_{bi}}{V_t}\right). \qquad \textbf{3.4}$$

Under forward bias, a positive potential is applied to the p side with respect to the n side, and the minority carrier hole concentration at the edge of the n-type space charge region is

$$p_n = p_{p0} \exp\left(\frac{-(V_{bi} - V_a)}{V_t}\right) = p_{n0} \exp\left(\frac{V_a}{V_t}\right). \qquad \textbf{3.5}$$

A similar treatment can be used to determine the minority carrier electron concentration on the p side. Therefore, at the edge of the space charge region, the minority carrier concentrations are much larger than their equilibrium values, resulting in diffusion and recombination processes that create a steady state current. The current arising from diffusion of minority carrier holes in the n-type region can be derived using the one dimensional continuity equation for holes,

$$D_p \frac{\partial^2(\delta p_n)}{\partial x^2} - \mu_p E \frac{\partial(\delta p_n)}{\partial x} + g' - \frac{\delta p_n}{\tau_{p0}} = \frac{\partial(\delta p_n)}{\partial t}, \qquad \textbf{3.6}$$

which contains terms for diffusion, drift, generation, and recombination. $D_p$ is the diffusion coefficient for holes, $\mu_p$ is hole mobility, $E$ is the electric field, $g'$ is excess carrier generation rate, $\tau_{p0}$ is the hole lifetime, and $\delta p_n$ represents the excess hole concentration (i.e. the number of carriers above the thermal equilibrium value of $p_{n0}$). If it is assumed that there is no electric field or generation outside the depletion region, this equation can be simplified to

$$\frac{\partial^2(\delta p_n)}{\partial x^2} - \frac{\delta p_n}{D_p \tau_{p0}} = 0. \qquad \textbf{3.7}$$

Equation 3.7 can be solved with the following set of boundary conditions:

$$p_n(x_n) = p_{n0} \exp\left(\frac{V_a}{V_t}\right) \text{ and} \qquad \textbf{3.8}$$

$$p_n(x = x_n + W_n) = p_{n0}, \qquad \textbf{3.9}$$

where $x_n$ is the edge of the depletion region on the n side and $W_n$ is the width of the neutral region on the n side. If $D_p\tau_{p0} = L_p^2$, where $L_p$ is the hole diffusion length, the general solution Equation 3.7 is

$$\delta p_n(x) = p_{n0}\left[\exp\left(\frac{V_a}{V_t}\right) - 1\right]\frac{\sinh\left[(x_n + W_n - x)/L_p\right]}{\sinh\left(W_n/L_p\right)}. \qquad \mathbf{3.10}$$

This result can be simplified significantly by examining the relationship between hole diffusion length and width of the n-type neutral region. If $W_n \gg L_n$, the generalized solution in equation 3.10 reduces to

$$\delta p_n(x) = p_{n0}\left[\exp\left(\frac{V_a}{V_t}\right) - 1\right]\exp\left(\frac{x_n - x}{L_p}\right). \qquad \mathbf{3.11}$$

This indicates that the concentration gradient of minority carrier holes on the n side decays exponentially to zero as $x \to \infty$. The standard equation for hole current density is

$$J_p(x_n) = -eD_p\frac{d\left(\delta p_n(x)\right)}{dx}, \qquad \mathbf{3.12}$$

and substituting 3.11 into 3.12 gives the hole current density from a forward biased pn junction

$$J_p(x_n) = \frac{eD_p p_{n0}}{L_p}\left[\exp\left(\frac{V_a}{V_t}\right) - 1\right]. \qquad \mathbf{3.13}$$

In summary, lowering the built in potential with a positive applied voltage first causes holes from the p side to be injected into the n side. This produces an excess of minority carrier holes, a concentration gradient, and a resulting diffusion current. The excess holes recombine with the majority carrier electrons on the n side and a constant current is produced within the device. An analogous derivation can be made for the diffusion current arising from the minority carrier electrons in the p region:

$$J_n\left(-x_p\right) = \frac{eD_n n_{p0}}{L_n}\left[\exp\left(\frac{V_a}{V_t}\right) - 1\right]. \qquad \mathbf{3.14}$$

Note that for positive applied voltage, the current densities $J_p$ and $J_n$ both increase in the positive $x$ direction as $V_a$ increases. In steady state, the current density through the device is constant, so that the hole and electron currents at any $x$ location can be added to find the total current. If the electron and hole currents are continuous and constant through the space charge region, it is convenient to determine the total current by adding the values derived above in 3.13 and 3.14. For example, $J = J_p(x_n) + J_n(-x_p)$ where it is assumed that $J_p(x_n) = J_p(-x_p)$;

$$J = \left[\frac{eD_p p_{n0}}{L_p} + \frac{eD_n n_{p0}}{L_n}\right]\left[\exp\left(\frac{V_a}{V_t}\right) - 1\right] = J_{S-long}\left[\exp\left(\frac{V_a}{V_t}\right) - 1\right], \quad \mathbf{3.15}$$

where $J_{S-long}$ is the saturation current in the long diode approximation. The same ideal current relationship can be derived if Equation 3.7 is solved with the boundary condition $p_n(x \to \infty) = p_{n0}$ instead of using equation 3.9.

In reality, the excess minority carrier decay is often not exponential because the neutral regions are not longer than the diffusion length. This can be true for solar cells with heavily doped front side emitters, or in solar cells with total thicknesses that are thin compared to the diffusion length. In this case, current density can be computed by setting $L_n \gg W_n$. Using this assumption, the hyperbolic sine terms in equation 3.10 are approximated by their arguments:

$$\sinh\left[\frac{W_n}{L_p}\right] \approx \left[\frac{W_n}{L_p}\right], \text{and} \quad \mathbf{3.16}$$

$$\sinh\left[\frac{x_n + W_n - x}{L_p}\right] \approx \left[\frac{x_n + W_n - x}{L_p}\right]. \quad \mathbf{3.17}$$

Deriving the current density using the one dimensional diffusion equation then results in

$$J_p(x_n) = \frac{eD_p p_{n0}}{W_n}\left[\exp\left(\frac{V_a}{V_t}\right) - 1\right]. \quad \mathbf{3.18}$$

If it is assumed that the junction is short on both sides, as is the case for some thin film solar cells, the current density is

$$J = \left[\frac{eD_p p_{n0}}{W_n} + \frac{eD_n n_{p0}}{W_p}\right]\left[\exp\left(\frac{V_a}{V_t}\right) - 1\right] = J_{S-short}\left[\exp\left(\frac{V_a}{V_t}\right) - 1\right]. \quad \mathbf{3.19}$$

In this case, because $L_n \gg W_n$ and $L_p \gg W_p$, the reverse saturation current can be much higher than in an equivalently doped long diode.

## 3.2 PN diode under illumination

A semiconductor can produce charge carriers under illumination if, in the simplest case, the energy of incident photons is greater than that of the semiconductor band gap. For silicon ($E_g \approx 1.12$ eV at room temperature), an electron hole pair can be created from photons of about 1100 nm and less. In direct band gap semiconductors, the absorption of photons with energy above the band gap is very high. However, the absorption edge is less sharp for indirect semiconductors because the conduction band minimum and the valence band maximum do not have the same crystal momentum. This means that silicon absorption is a strong function of wavelength; high energy photons near UV or violet absorb very near the surface of the silicon, whereas red and near infrared light can penetrate significantly. For example, the absorption length, defined as the depth at which the incident intensity drops to $1/e$ of its initial value, is about 10 nm for 400 nm light, and it is over 1 μm for 800 nm light [69].

If a long pn junction is illuminated by a near infrared light near the band edge, say 1050 nm, the electron-hole generation can be approximated as a constant throughout the device because of the low absorption. Equation 3.6 can again be solved to find a solution for illuminated junction characteristics, still assuming no field in the neutral regions but taking into account the generation term,

$$\frac{\partial^2(\delta p_n)}{\partial x^2} - \frac{\delta p_n}{D_p \tau_{p0}} + g' = 0. \qquad \mathbf{3.20}$$

The solution to equation 3.20, and the analog problem for electrons on the p side, are

$$J_p(x) = \frac{eD_p p_{n0}}{L_p}\left[\exp\left(\frac{V_a}{V_t}\right) - 1\right]\exp\left(\frac{x_n - x}{L_p}\right) - eg'L_p \exp\left(\frac{x_n - x}{L_p}\right) \text{ and} \qquad \mathbf{3.21}$$

$$J_n(x) = \frac{eD_n n_{p0}}{L_n}\left[\exp\left(\frac{V_a}{V_t}\right) - 1\right]\exp\left(\frac{x_p + x}{L_n}\right) - eg'L_n \exp\left(\frac{x_p + x}{L_n}\right). \qquad \mathbf{3.22}$$

In addition, because the generation is uniform throughout the device, there must be a current contribution from carriers generated within the depletion region. Because of the large electric field in the depletion region, in the simplest case it is assumed that all the carriers generated are swept out and contribute to the total current

$$J_w = eg'W_d, \qquad \mathbf{3.23}$$

where

$$W_d = x_n + x_p = \sqrt{\frac{2\varepsilon_{Si}\varepsilon_0}{e}(V_{bi} - V_a)\frac{N_a + N_d}{N_a N_d}}. \qquad \mathbf{3.24}$$

So the illuminated current response in an ideal long diode is

$$J = J_{S-long}\left[\exp\left(\frac{V_a}{V_t}\right) - 1\right] - eg'(L_n + L_p + W_d), \qquad \mathbf{3.25}$$

$$J = J_{S-long}\left[\exp\left(\frac{V_a}{V_t}\right) - 1\right] - J_L.$$

What this implies is that, for a uniform generation in a long diode, the generation current $J_L$ flows opposite of current induced by a positive external voltage $V_a$, and also that it is independent of $V_a$. Any carriers generated in the depletion region, or within a diffusion length of it, contribute to this current. In other words, the normal dark current curve for a long diode is moved downward by a constant value when additional carriers are generated evenly throughout the device. The short circuit current density can be easily determined from equation 3.25 by setting $V_a$ to zero:

$$J_{SC} = -J_L. \tag{3.26}$$

The cell open circuit voltage, $V_{OC}$, can be found by setting $J = 0$ in equation 3.25 and solving for $V_a$:

$$V_{OC} = V_t \ln\left[\frac{J_L}{J_{S-long}} + 1\right]. \tag{3.27}$$

The power conversion efficiency of a cell is defined as the maximum output power of the cell over the total optical input power. Cell output power is $VI$, so max output power can be found by determining the voltage at which maximum power occurs with

$$\frac{dP}{dV} = d\left(V\left(J_{S-long}\left[\exp\left(\frac{V}{V_t}\right) - 1\right] - J_L\right)\right)/dV = 0,$$

$$\left(1 + \frac{V_m}{V_t}\right)\exp\left(\frac{V_m}{V_t}\right) = 1 + \frac{I_L}{I_{S-long}}, \tag{3.28}$$

where $V_m$ is the voltage corresponding to maximum power output. The corresponding maximum current is found by substituting $V_m$ into equation 3.25. Note that $J$ is current density expressed in amperes/area, and $VJ$ is not actually power but rather has the units watts/area. However, illumination is usually given in intensity, and therefore efficiency will indeed be unitless. It is common to define efficiency $\eta$ using a fill factor $FF$ in the following manner

$$FF = \frac{V_m I_m}{V_{OC} I_{SC}}, \tag{3.29}$$

$$\eta = \frac{FF \cdot V_{OC} I_{SC}}{P_{opt}}. \tag{3.30}$$

## 3.3 Solar cells

Operating characteristics for the most common industrial solar cells, with an $n^+$ emitter and $p^-$ base, can be calculated reasonably well using analytical methods. Cell structures with a strong 2D and 3D dependence are more difficult to describe. In the derivations above, effects from recombination in the depletion region, resistive losses, and many other important parameters were not included. For example, in real solar cells, effects from non-uniform generation and bulk and surface recombination drastically change device characteristics, and can also make deriving analytical solutions more difficult. Solar cell losses can be broken into two general categories: intrinsic and extrinsic. Intrinsic losses are those that are unavoidable due to fundamental physical laws, and extrinsic losses are those that proper design can mitigate or eliminate.

### 3.3.1 Intrinsic losses

In 1961, Shockley and Queisser presented the first theory for maximum solar cell efficiency using the detailed balance limit. Previously, conversion efficiencies were determined using empirical values. First, an “ultimate efficiency” was calculated using Planck’s Law for black-body radiation and assuming that every photon above the energy gap produces a single electron hole pair. Next, solar cell steady state current-voltage relationships were derived by equating rates of photo-generated electron-hole (EH) pairs, cell radiative recombination, non-radiative generation and recombination, and EH pair removal by the cell pn junction. It was also mentioned that recombination centers from imperfections and impurities could be the primary cause of recombination in semiconductors [70].

Hirst and Ekins-daukes recently discussed five intrinsic losses for single band gap solar cells: below gap loss, thermalisation loss, emission loss, Carnot loss, and Boltzmann loss. Below band gap loss refers to losses that arise because incident photons do not possess sufficient energy to excite and electron-hole pair, for example photons with wavelengths larger than ~1100 nm impinging upon silicon solar cells. Thermalisation loss occurs because electrons excited into the conduction band with energies greater than the band gap will quickly lose excess energy as the electron relaxes to the conduction band edge. Emission loss occurs because solar cells themselves act as black bodies, and must emit some radiation. Carnot loss results in a voltage drop because of thermal processes. Boltzmann loss occurs because of entropy increases when the absorption and emission angles differ. Analytical expressions for each loss were also given [71].

### 3.3.2 Optical losses

Optical losses are primarily the result of reflection and transmission, and are a strong factor of device geometry and design. Reflection losses occur because of a mismatch in index of refraction as light hits a solar cell. For normally incident illumination from one medium onto another, the reflection is given as:

$$R = \left|\frac{n_1 - n_2}{n_1 + n_2}\right|^2 \qquad \mathbf{3.31}$$

For example, reflection of 550 nm light off an air-silicon interface ($n_{air} \approx 1, n_{Si} \approx 4.1$) is about 37%. Typically, solar cells are designed with an anti-reflection (AR) coating that is comprised of a either a single or multiple dielectric coatings. The reflection from a single layer AR coating on silicon is given by:

$$R = \frac{n_1^2(n_{air} - n_{Si})^2(\cos\phi)^2 + (n_{air}n_{Si} - n_1^2)^2(\sin\phi)^2}{n_1^2(n_{air} + n_{Si})^2(\cos\phi)^2 + (n_{air}n_{Si} + n_1^2)^2(\sin\phi)^2} \qquad \mathbf{3.32}$$

$$\phi = \left(\frac{2\pi}{\lambda}\right) n_1 t \qquad \mathbf{3.33}$$

where $n_1$ is the index of the dielectric coating and $\phi$ is the phase accumulated in a trip through the dielectric thickness $t$. A single layer dielectric AR coating cannot be perfect for the entire spectrum, so it is normally optimized for the peak intensity of incoming AM1.5 spectrum (~550 nm). Additionally, surface texturing can reduce reflection and has been used extensively. The standard PERL cell (described in detail in 3.6.1) employed inverted pyramids with a double layer anti-reflection coating [72]. A similar cell was created using random pyramids, achieving 21% efficiency on Cz grown silicon [73].

There have also been more exotic methods for AR in solar cells. Zhao developed a 19.8% efficient multi-crystalline solar cell by using a hexagonally symmetric, isotropic etch to create a honeycomb-like structure for anti-reflection. Although inverted pyramids trap light better, the fabrication method to produce inverted pyramids requires anisotropic wet etching that cannot be achieved in the random structure of multi-crystalline wafers [74]. More recently, solar cells have been created with nanodome structures to reduce reflection and enhance absorption on very thin solar cells. These cells absorbed 94% of light ranging from 400-800 nm in a layer of only 280 nm. Domes were formed by packing $SiO_2$ nanoparticles onto a silicon substrate to use as a mask for reactive ion etching. Solar cell layers (bottom Ag reflector, bottom electron, active region, top electrode) were grown on the resulting cones, creating the nanodome structure [75].

Transmission loss occurs when photons with energy close to that of the band gap are not absorbed by the crystal. This is of particular interest for thin solar cells, where the absorption length for longer wavelength light is on the same order as the cell thickness. Transmission loss can be minimized by using a thick wafer, but this requires high quality silicon with high minority carrier lifetimes and diffusion lengths that can significantly increase cost. Alternatively, light trapping schemes can increase the effective thickness of the solar cell by forcing light to travel through the thickness several times, thus allowing the use of thinner, lower quality silicon [76–78].

Lastly, grid finger shadowing can also cause optical loss, but with careful design this can be minimized while also keeping contact resistance low, for example with the use of buried contacts. Here, the cell top surface is grooved mechanically or with a laser to create deep trenches in the silicon that are highly diffused and electrolessly plated [79]. Also grid finger shading can be entirely avoided by using back contact solar cells, described in 3.6.3.

### 3.3.3 Bulk recombination

Recombination through trap states was initially described by Shockley and Read [80], and also Hall in the early 1950s . Theoretical and empirical work showed that recombination in semiconductors is largely due to trap levels within the semiconductor band gap that arise from crystal defects (e.g. vacancies) or impurity elements. This theory was developed by examining four processes that can take place involving a trap: trap capture (1) and emission (2) of electrons from the conduction band, and trap capture

(3) and emission (4) of holes from the valence band. The common expression for recombination $U$ is

$$U = \frac{(np - n_i^2)}{\left[\tau_{p0}(n + n') + \tau_{n0}(p + p')\right]}, \qquad \mathbf{3.34}$$

where

$$n' = N_c \exp\left(\frac{-(E_c - E_t)}{kT}\right), \text{and}$$

$$p' = N_v \exp\left(\frac{-(E_t - E_v)}{kT}\right).$$

For an extrinsic semiconductor in low level injection, the lifetime is inversely proportional to the minority carrier capture cross section and the density of traps. Thus, for an n-type semiconductor the recombination is inversely proportional to the minority carrier hole lifetime. Recombination due to traps causes currents in real diodes to deviate significantly from the ideal case in equations 3.15, because it allows for an additional current path. That is, holes injected from the n-side can recombine with electrons injected from the p-side in the space charge region. The contribution of current in the space charge region was described by Sah in 1957 [81], leading to the common two-term diode model:

$$J = J_{S1}\left[\exp\left(\frac{V_a}{n_1 V_t}\right) - 1\right] + J_{S2}\left[\exp\left(\frac{V_a}{n_2 V_t}\right) - 1\right], \qquad \mathbf{3.35}$$

where $J_{S1}$ represents the ideal saturation current (for a short or long approximation), $J_{S2}$ is included to account for recombination in the space charge region, and $n_1$ and $n_2$ are ideally 1 and 2, respectively. Recombination can play a role in reducing carrier collection in the base, emitter, and depletion regions. In general, high recombination in the bulk semiconductor will manifest as a low minority carrier lifetimes, low minority carrier diffusion lengths, and low current density.

### 3.3.4 Surface Recombination

The surface of a semiconductor can exhibit high recombination because of the abrupt break the periodicity of the crystal lattice, causing a large number of surface states within the band gap. Reducing the surface recombination is an important factor contributing to high efficiency in solar cells, and as a result the topic has been studied extensively [82]. An expression similar to that of bulk recombination can be derived for surface recombination; recombination at the surface is a function of the trap state properties, capture cross sections, doping levels at the surface, and injection level. In general, there are two ways of reducing the recombination at the surface: reduce the number of trap states or reduce the number of free carriers at the surface.

The first method to reduce the surface recombination velocity is to remove the number of trap states by growth or deposition of a material that will remove dangling bonds at the surface. The most common method is the use of the thermal oxide. Another popular coating for passivation is PECVD $SiN_x$. Due to the processing gases used during $SiN_x$ passivation, it contains a significant amount of hydrogen that can diffuse into the silicon and help to passivate surface and bulk defects and increase minority carrier lifetimes. $SiN_x$ also has an index of refraction well-suited for anti-reflection coatings.

A more exotic means of surface passivation is valence-mending. Depending on the exposed orientation, <100> or <111> for example, single layers of atoms like selenium can be deposited to remove and dangling bonds at the silicon surface. Unlike $SiO_2$ and $SiN_x$, which are at least a few nanometers thick to provide adequate passivation, this technique requires only a monolayer. Therefore, it can simultaneously reduce surface recombination and contact resistance. However, this requires extreme deposition control, because more than a monolayer will introduce new dangling bonds and less will leave the dangling silicon bonds exposed. Also, the current deposition method (molecular beam epitaxy) is too slow and expensive for industrial use [83].

Reducing the number of carriers at an interface can be accomplished by implementing a doping profile ($p^+p$ or $n^+n$ junction) to “reflect” minority carriers, or by using the field-effect from a charged insulator or metal-insulator. A doping profile used in this way is typically referred to as a back surface field (BSF) or front surface field (FSF).

### 3.3.5 Resistive losses

As current flows in a solar cell and to a load, it encounters resistance from the metal bus lines, the metal-emitter contact, the emitter, the base, and the base-metal contact. Resistive losses decrease the fill factor or open circuit voltage, and should therefore be minimized. For standard solar cells with a front surface grid, the metal line thickness is very important. A wider (or thicker) metal reduces the trace resistance, but also increases the shading loss. Additionally, the width of the metal-semiconductor contact is important, and thus there is a tradeoff between having high recombination for ohmic contact, and reducing the unwanted minority carrier recombination. The base resistance for standard solar cells, especially thin solar cells, is normally negligible. For example, a cell with base resistivity of 1 Ω-cm, thickness of 300 μm, and area of 1 cm would yield a resistance $R = \rho l / A = 0.03$ Ω.

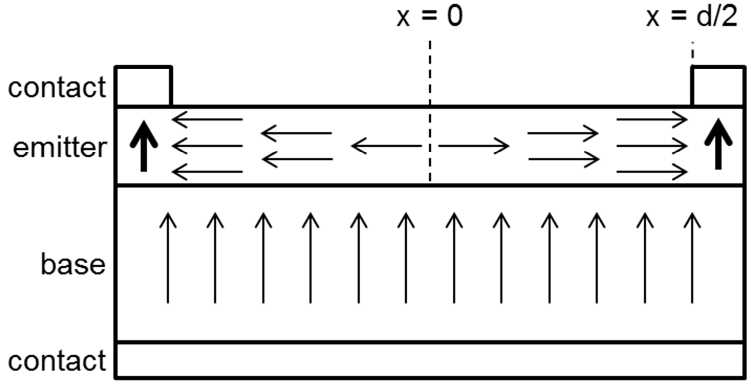

**Figure 14. Idealized current flow in a solar cell used for calculation of emitter resistance. It is assumed that the current in the base in homogeneous, so that the current in the emitter increases linearly from the center to the emitter contact.**

The emitter resistance is more complicated, as is the resistance of the base in an interdigitated back junction back contact cell (described in section 3.6.3). In a standard cell, the emitter resistance can be calculated assuming that current flowing into the emitter from the base is homogeneous, and therefore that the lateral current in the emitter increases linearly from zero exactly between two grid fingers ($x = 0$) to $J/2$ at the finger contacts ($x = \pm d/2$, see Figure 14). This means that the current flowing into the emitter regions in terms of distance from the midline between emitter contacts is

$$I(x) = Jlx, \tag{3.36}$$

where $l$ is the length of the emitter contact (i.e. length of the emitter contact normal to the cross section shown in Figure 14). Next, if the sheet resistance is defined as the average resistivity over the junction depth the differential resistance of a strip of emitter parallel with fingers is

$$dR_{emit} = \frac{R_{sq}}{l}dx. \tag{3.37}$$

The power loss in the in this thin strip is

$$dP = I(x)^2 dR = (Jlx)^2 \frac{R_{sq}}{l} dx. \tag{3.38}$$

Integrating from $0$ to $d/2$ gives the total power dissipated

$$P = J^2 l R_{sq} \frac{d^3}{24}, \tag{3.39}$$

which is power consumed from the resistance in half of the emitter. Therefore, the effective emitter resistance is the power divided by the maximum current squared

$$R_{eff} = \frac{P}{{I_{max}}^2} = \frac{R_{sq}}{l}\frac{d}{6}. \tag{3.40}$$

Intuition also would lead to the same conclusion, that decreasing the sheet resistance and the separation while increasing the length of the contacts would minimize the emitter resistance. Goetzberger covers a broad spectrum of losses and has many effects parameterized for a standard solar cell design with a highly doped front surface n-type emitter and a low doped p-type base [67]. Using the two diode model and lumped resistances, a reasonable model for a solar cell can be established (Figure 15). Using this model, the total solar cell current density becomes

$$J = J_{S1}\left[\exp\left(\frac{V_a - IR_{series}}{n_1 V_t}\right) - 1\right] + J_{S2}\left[\exp\left(\frac{V_a - IR_{series}}{n_2 V_t}\right) - 1\right] - \frac{V_a - IR_{series}}{R_{shunt}} - J_L. \tag{3.41}$$

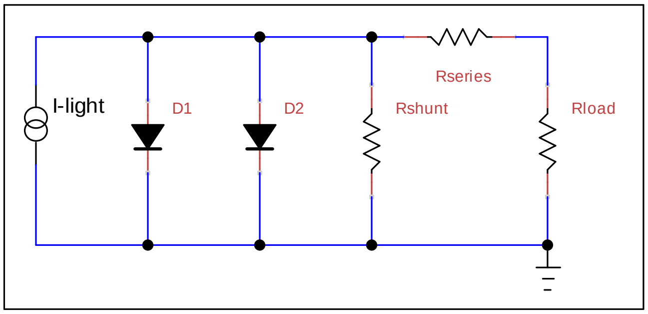

**Figure 15. Two-term circuit model of a real solar cell.**

## 3.4 Solar cells at low light intensity

Solar cells are typically characterized at AM1.5, a spectrum designed to simulate light that has passed through an *air mass* 1.5 times that of normal incidence light at the equator (about 41.8 degrees from off the horizon). However, solar cells for a contact lens must be able to produce power indoors, at much lower light intensity with widely varying spectra. In the simplified case of uniform generation and a long, ideal diode, the effect of light intensity on efficiency can be estimated using equations 3.25, 3.27, and 3.30. Short circuit current is proportional to the generation rate, or $I_L \propto g'$, $V_{OC} \propto \ln(g')$ when $I_L \gg I_{S-long}$ (i.e. when $I_L / I_{S-long} \gg 1$), and it is also reasonable to assume that $g' \propto P_{opt}$. Therefore, to first approximation without taking into account the variations in fill factor as a function of light intensity,

$$\eta = \frac{FF \cdot V_{OC} I_{SC}}{P_{opt}} \propto \frac{\ln(g')\, g'}{g'} \propto \ln(P_{opt}). \qquad \mathbf{3.42}$$

Although it is expected that the efficiency of a solar cell will drop with decreasing optical intensity, there are many processing and fabrication considerations that can keep this relationship from becoming more detrimental. There has been limited research dedicated specifically to solar cell operation at irradiance levels on par with indoor lighting, but design considerations can be gleaned from what few research efforts exist.

In response to challenges designing Product Integrated Photovoltaics (PIPV), Reich et al. measured 41 industrial mono- and multi-crystalline solar cells at light levels ranging from 3 to 1000 W/m$^2$ using neutral density filters, and assessed the accuracy of several different modeling approaches intended to predict the low light level performance from standard PV data. Cell efficiencies at one sun were similar for all cells, but varied widely at 3 W/m$^2$. For example, the relative difference in efficiency of two cells was 1% at one sun, but increased to over 200% at the minimum intensity measured. After comprehensive cell measurements, including one cell measured in a wider range (0.04 to 1000 W/m$^2$), various models were examined to determine which was most effective at predicting low light level efficiency. They used one-diode and two-diode models, where the two diode model more accurately accounted for different losses in real solar cells. Diodes with different ideality factors account for diffusion-based recombination in the neutral regions (n = 1), and a second accounts for the space charge region diode (n = 2), as discussed in section 3.3.3. In modeling the effect of series and shunt resistance, it was determined that shunt resistance played a major role at low light levels, and should be high (>10kOhm-cm$^2$) to keep efficiency as high as possible at low light levels. Although many different commercial cells were tested, little was known or discussed about cell fabrication or design (other than mono- or multi-crystalline). Theoretical explanations as to why cells behaved better or worse at low light levels were not included (aside from shunt resistance), nor were any discussions of thin film solar cells due to more complex physical phenomena such as voltage-dependent photocurrent collection [84].

Randall and Jacot also measured several cells at intensities ranging from 0.1 to 1000 W/m$^2$ under AM1.5 and also under fluorescent tubes from 1-10 W/m$^2$. Twenty-one cells with areas less than 5 cm x 5 cm were measured, including crystalline, polycrystalline, and amorphous silicon, GaAs, CdTe thin film, CIGS thin film, and GaInP cells. Efficiency was modeled using an equation derived from fill factor, short circuit current as a function of intensity, and open circuit voltage as a function of short and saturation currents. Again, the role of shunt resistance at low light levels was emphasized, suggesting a natural log relationship between shunt resistance and efficiency.

## 3.5 N type silicon for solar cells

Solar cells are commonly made from Cz grown p-type silicon wafers. However, these cells exhibit a characteristic decay in performance under illumination. Schmidt et al. used boron, gallium, and phosphorus doped silicon wafers to determine the carrier lifetimes during illumination and after annealing. Both cell surfaces were passivated with PECVD silicon nitride, and lifetimes were measured using microwave-detected photoconductance decay. Oxygen content was measured using infrared absorption. In the boron doped wafers, lifetimes degraded after an illumination time of tens of minutes, with higher degradation for higher doping concentrations. This behavior was not observed in the gallium or phosphorus doped wafers. A model was proposed in which the light-induced degradation and recovery upon annealing results from the competing action of boron-oxygen defect centers and boron-carbon ones. Because of the degradation, they proposed using n-type wafers or doping with another group five element to avoid boron-oxygen traps. In addition, higher resistivity wafers or different growth methods (e.g. without quartz crucible) would also alleviate this problem [85].

It has also been shown that n-type monocrystalline solar cells outperform p-type cells at low light levels. Gong et al. examined the low injection level limit of Shockley Reed Hall recombination and concluded that the n-type minority carrier lifetimes are impacted less by decreasing light levels because of smaller hole capture cross sections. Deep and shallow defects were considered, and the calculated minority carrier lifetimes were higher for n-type cells. N and p-type cells fabricated using similar processing were tested as a function of intensity, and the n-type cells performed better. However, the cell design, base dopant concentration, wafer growth method, and cell thickness were not the same for both experiments. For example, the n-type wafer was Cz grown, 625 µm thick, and 10 Ohm-cm, whereas the p-type wafer was FZ, 250 µm thick, and 0.5 Ohm-cm [86].

## 3.6 Review of solar cells

The first report of silicon solar cells was presented by Chapin, Fuller, and Pearson in their 1954 paper, “A new silicon p-n junction photocell for converting solar radiation into electrical power.” It discussed various challenges associated with increasing the efficiency beyond the reported 6%, including unavoidable losses, such as above and below band gap losses, and avoidable losses like reflection, recombination, and resistance [87]. Solar cell technology has since evolved and branched, and now there are crystalline silicon cells of 25% efficiency, GaAs cells over 28% efficient, and even organic polymer cells of over 8% [88].

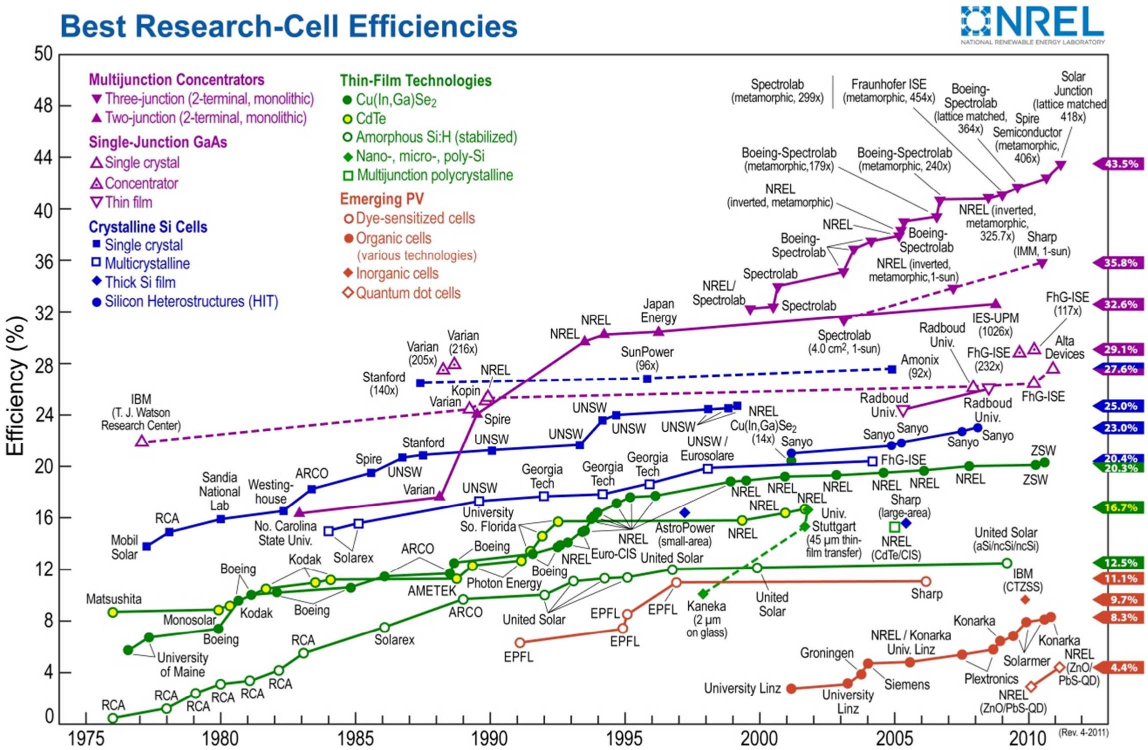

**Figure 16. Best research cell efficiencies, compiled by Lawrence Kazmerski, National Renewable Energy Laboratory (NREL).**

### 3.6.1 Standard high efficiency cells

The most common industrial structure for solar cells has a highly-doped, silicon oxide passivated front side n-type emitter with a thick (hundreds of µm), lightly-doped p-type base. The front side has a grid of metal contacts, and the backside is totally metallized. This basic structure, albeit with many more fabrication steps and much more complexity, is used in the highest efficiency silicon solar cells. Blakers and Green have been the primary investigators of this cell type, and have been increasing cell efficiency steadily since the 1980s. A review of their progress during this time is useful in determining the primary losses in real solar cells and how they can be minimized.

In 1981, Blakers and Green reported the metal-insulator-NP junction (MINP) cell, which is essentially the cell described above, with oxide under the emitter metal contacts that is sufficiently thin to allow for tunneling. Under AM0 conditions the cell open circuit voltage was 678 mV. This cell incorporated a light front surface n-type implant, Al back contact with annealing to form a back surface field, front surface metal fingers, and an evaporated SiO front surface anti-reflection coating. It had an estimated efficiency of 16% under AM1.0 [89]. Three years later, they presented an 18% efficient cell with an improved front surface metallization (Ti/Pd/electroplated Ag instead of Mg) and a broadband double layer AR coating (MgF/ZnS), which allowed for thinner front side contacts and less optical loss from reflection, respectively. The importance of front surface passivation for increase the open circuit voltage was stressed, including reducing recombination at the metal-semiconductor interface by reducing its area and reducing the recombination in the exposed regions by growing a thin thermal oxide [90].

The next major improvement was made in 1984. Green et al. reported a 19.1% efficient passivated emitter solar cell (PESC) that, instead of having a thin oxide under the metal contacts, reduced the contact area on the front side by employing localized contacts. N contacts were made with Ti/Pd using a self-aligned process whereby the same photoresist that was utilized for oxide etching was also used for lift-off. This led to a series of passivated emitter cells, each with increasing efficiency. This included an improved PERC (passivated emitter rear cell) with inverted pyramid surface texturing and an oxide passivated rear surface with localized contacts. Although the metal coverage was higher, the metal grids only contacted the solar cells on 0.5% of the top surface, under which the silicon was heavily diffused to produce good ohmic contact and low recombination. Because of the passivated rear surface, aluminum layer on the opposite side acted as a good reflector for longer wavelength light that traveled through the cell thickness [91]. This led to the passivated emitter rear locally-diffused (PERL), with 24% efficiency. Here, they employed localized heavy boron doping under the back contacts, which reduced minority carrier recombination, allowed for closer contact spacing, and thus reduced the lateral resistance between contacts. They also were able to use higher resistivity silicon, while still having very good ohmic contacts [92]. It is worth noting that all of these cells were made using float zone wafers.

### 3.6.2 Emitter wrap through

Another common solar cell class, the emitter wrap through (EWT) cell, was introduced in 1993 by Gee, Schubert, and Basore. It was designed to eliminate the trade-off between low grid resistance and low grid optical loss, while maintaining the front surface emitter for good collection efficiency. A front surface emitter is particularly important when cell thickness is greater than diffusion length, because top side illumination will generate most of the mobile charge carriers near the surface. Fabrication and assembly complexity can be reduced by taking out the requirement of thin front contacts and front-to-back cell stringing, respectively. This design incorporates through-wafer vias heavily doped to connect the front surface emitter to the emitter contact on the back of the wafer. Interdigitated back contacts are required, but with less restricted requirements on feature size than for front grid patterning. Typically the highly doped vias are electrolessly plated with nickel and then copper or silver. EWT cells can also have a backside emitter, in what is called a double-junction EWT cell, improving collection efficiency [93].

Low fill factors have limited efficiency in EWT cells, but in 2010 Ulzhöfer et al. demonstrated that the losses were primarily due to recombination in the base and could therefore be minimized by careful selection of base doping [94]. Recently, Kiefer et al. developed EWT cells on Cz grown n-type wafers with efficiencies up to 21.6%. Instead of the common three diffusion process necessary for most high-efficiency cells (i.e. n emitter diffusion, $n^+$ emitter contact diffusion, $p^+$ BSF and ohmic contact), they employed only two diffusions, a phosphorus diffusion for BSF and boron diffusion for the front, via, and back regions of the emitter. All emitter surfaces were passivated with an $Al_2O_3$-$SiN_x$ stack [95].

### 3.6.3 Back junction back contact

Another type of cell that has been used extensively in concentrator applications, and more recently in thin and small solar cells (see 3.6.4) is the back junction back contact (BJBC) solar cell. As with the EWT cell, there are no front contacts, but in this case the junction is only on the back side of the wafer. This allows for increased cell packing density, and less optical reflection loss, and in most cases lower emitter resistance losses (as opposed to the standard cell where current flows long distances laterally through the thin front side emitter). However, the lack of collection at the front surface means that the bulk minority carrier lifetime must be high and, especially, that the front surface must be passivated very well [96].

Bock recently created a BJBC cell with using 150 µm thick n-type Cz grown silicon with an efficiency of 19%. The front surface featured a $SiN_x$ anti-reflection coating (ARC) over a textured, moderately doped $n^+$ region that acted as a front surface field to repel minority carrier holes. The back surface emitter was created by screen printing aluminum, firing, and then removing excess aluminum, the Al-Si eutectic, and 2-3 µm of the underlying silicon. The back surface was then covered in $SiN_x$ and laser ablated in regions where the n-type contacts were to be made. After etching in KOH through the blanket Al emitter, the n-contact regions were heavily doped. All $SiN_x$ was then removed, and a stack of 10 nm oxide and 70 nm $SiN_x$ was applied to all surfaces. Lastly, 15 µm of aluminum was deposited and etched for contacts [97].

A similar cell was created using screen-printing for every metallization. The front surface was textured, doped, and coated with thermal SiO2 and $SiN_x$. Instead of a blanket Al emitter that is etched through as in the previous example, the localized emitter and contact were created simultaneously by firing a screen printed Al aluminum paste in a belt furnace [98].

### 3.6.4 Small area solar cells

Most solar cells are created for large scale power generation. However, for a contact lens system, the cell requirements are significantly different because the area and thickness of the cell must be constrained. Although many of these cells were created for larger scale power applications, their fabrication, size, and, in some cases, flexibility, are useful to review before designing solar cells for contact lenses.

Bellew et al. developed solar cells on 50 µm silicon-on-insulator (SOI) wafers with isolation trenches etched to the buried oxide. First, silicon wafers were implanted with boron to create a $p^+$ layer that eventually would be a back surface field for the solar cell. Then a thick thermal oxide was grown, and two wafers were fusion bonded at 1100ºC. The wafer with the $p^+$ layer was then ground and polished to a final thickness of 50 µm. Trenches were created with DRIE and were subsequently coated with a thin LPCVD nitride and filled completely with intrinsic LPCVD polysilicon. Next, three implants created the p contact region, n emitter region, and n contact region, which were driven in during a 1050ºC oxidation/surface passivation. The cells were connected in arrays with an estimated 14.3% efficiency at AM2.0 [99].

Similarly, Ortega fabricated solar cells using SOI wafers, isolation trenches, and arrays, but with device thicknesses of 5 and 10 µm. However, standard SOI wafers were used (i.e. without the BSF on the buried oxide), the emitter extended to all sides of the cell except the backside, and trench etching was accomplished with TMAH. Presumably the wafers were of <111> orientation. Cells had areas of 0.225 mm$^2$, open circuit voltages between 620 and 660 mV, and were connected in series during microfabrication. A module of 169 series connected cells (~0.42 cm$^2$) produced 3.2 mW of power at 103V. Relating experimental results to PC1D simulations showed that the back surface recombination of these cells (i.e. buried oxide $SiO_2$-device Si interface), had surface recombination velocities between $10^2$ and $10^3$ cm/s. Ten µm cells outperformed the 5 µm cells slightly (10.2% and 8.9%, respectively) [100]. In the examples presented above, the cells remained on the handle wafer for mechanical stability, hence were not freestanding.

Yoon et al. developed arrays of micro solar cells using crystalline silicon <111> wafers using a transfer printing process and post transfer metallization to connect cells into arrays. They doped long and narrow cells, then etched into the wafer somewhere between 5 and 50 µm, depending on the desired cell thickness. The cells were passivated, and anisotropic wet etching in KOH removed all but a small portion of the silicon underneath the cells called anchors. An elastomeric stamp was used to break the anchors and transfer the cells to a second, ultraviolet-curable polymer substrate. After the stamping processing, cells were connected with a final metallization. Although this fabrication method was used to create cells of various sizes, those that were 15 x 50 x 1550 µm$^3$ had efficiencies of 7% at AM1.5 and 1000 W/m$^2$ [101].

Knuesel and Jacobs designed and fabricated freestanding and self-assembled solar cells from 20 µm device thickness SOI wafers with widths varying between 20 and 60 µm. Simple cells, made with one diffusion, one metallization, a single silicon trench etch, and buried oxide etch release, were designed primarily to test a method of self-assembly in which parts were connected to a substrate at the interface between water, silicone oil, and solder. After assembly, the cells were coated with SU-8, the SU-8 was etched back to reveal the top contact, and the second metal contact was evaporated. Thus these cells required post-assembly processing to create arrays, because p and n contacts were on opposing sides of the cell [102]. Also, although a transparent conductive oxide could have been used, the top contact was very thin gold which created a tradeoff between low resistance and low optical loss.

Another example of released, small area, back contact solar cells are Microsystems Enabled Photovoltaics (MEPV). First, $n^+$ and $p^+$ implants are performed, followed by a deep silicon etch to define the approximate cell shape (hexagonal, ~250 µm width) and thickness (~20 µm). Then they passivated the silicon with a LPCVD nitride, and opened holes for metal contact and to expose the bottom of the trenches. After depositing and patterning a tungsten layer, they etched further into the trenches (~5 µm) to expose silicon for wet anisotropic etching in a manner similar to that describe above in [101]. Here, however, the entire cell was released (i.e. no anchors holding the cells to the wafer). The primary purpose for creating these was to reduce silicon use by reusing a thick wafer several times using the same process. After release, the front surface (previously etched in KOH) had to be passivated to produce high efficiency. They experimented with atomic layer deposited alumina for passivation (3 – 4% efficiencies with forming gas anneal), and PECVD silicon nitride with various temperatures, ammonia-to-silane ratios, and RF power settings. Device assembly was not discussed thoroughly, nor were any difficulties in PECVD deposition on such miniscule parts [103].

Presumably to confront the problem of PECVD on small parts, they developed a method to accomplish all high-temperature steps while the cells were still on the wafer. Starting with a p-type SOI and a 1 µm buried oxide, honeycomb-shaped trenches were etched into the silicon, through the buried oxide, and then filled with polysilicon. Next, chemical mechanical polishing exposed the top surface, and the device layer was etched through again, exposing the buried oxide while keeping the tethers intact. HF was used to etch the entirety of the buried oxide, leaving silicon hexagons attached with tethers. Subsequent LPCVD nitride deposition showed that the underside of the hexagons was sufficiently covered [104].

Other interesting types of small solar cells are those made from multi-crystalline spherical silicon. Minemoto et al. created 1 mm spherical, multi-crystalline p-type silicon spheres by forcing molten silicon through a small aperture at the bottom of a crucible and that crystallizes during a long free fall. The resulting spheres were uniformly doped with phosphorus to create an emitter structure. Then part of the cell was ground to expose the p-region, contacts were applied, and an antireflection coating was deposited. Lastly, the spheres were mounted in cup reflectors, with efficiencies up to 10% using the area defined by the cup aperture [105]. Similar cells had been described earlier [106].

# Chapter 4: Solar cells on contact lenses

There are two primary challenges for designing silicon solar cells for use on contact lenses. First, the solar cells must provide sufficient power, as discussed in section 1.4. Total output power, not just efficiency or cost, is the primary concern. Second, solar cells for contact lenses need to conform to a sphere with radius of 7.8 mm. This is inherently more difficult than creating structures for cylindrical deformation, because stretching occurs irrespective of the substrate thickness. For example, a thin, planar sheet of cellophane can easily conform to a cylinder, such as the roll it is normally dispensed from. However, covering a basketball with the same sheet requires that the cellophane stretch. In summary, efficiency, ease of assembly, total area covered, and ability to conform to a sphere must be taken into account. There is a wealth of knowledge on how to produce efficient solar cells and an increasing interest in creating flexible electronics. The first approach capable of achieving these goals is to use a multitude of rigid but very small cells connected by flexible and malleable interconnects. Another method is to assemble one or two large, flexible cells.

One advantage of assembling many small solar cells is that adjusting the output voltage and current can be accomplished by changing the connections on the contact lens substrate. Circuit design could be simplified by providing close to the appropriate voltage using three sets of solar cells connected in series, which would give around 1.5 V instead of 0.5 V. Additionally, this would allow for built-in spacing for diffusion of oxygen and nutrients to the cornea through the polymer contact lens. However, assembling a large number of cells could be time consuming and unreliable.

Assembling one or two flexible, relatively large cells could potentially cover more area and would certainly be easier to assemble. With more area, requirements for efficiency could be lessened along with fabrication complexity. However, it would be more difficult to stack cells and tailor the output voltage, and the tradeoff between cell efficiency, flexibility, and reliability in terms of thickness would need to be carefully examined.  Although both methods were explored, the multi-cell approach was more closely related to previous work and was hence pursued first.

## 4.1 Multi-cell design

There have been several examples of arrays of rigid electronic devices on spherical surfaces.  Lacour et al. also test the characteristics of stiff islands of material on a stretchable substrate.  Islands 200 x 200 µm of stiff, diamondlike carbon was deposited onto PDMS substrates, and then interconnects of thin Cr and 25 nm Au were deposited and patterned.  The resistance of Au interconnects, which were 200 µm wide by 1 cm long by 25 µm thick, were tested under 20% strain along their length.  The resistance increased almost linearly with strain.  Cracks were observed afterward, but never crossed the entirety of the Au strips [107].  Although no functional devices were used, this work demonstrated the ability of Au strips to stretch appreciably and maintain electrical conductivity.

Hsu et al. fabricated thin amorphous transistors directly on a deformable polyimide sheet.  First, a $SiN_x$ layer was deposited on the polyimide, followed by a Cr gate electrode, a $SiN_x$ gate insulator, undoped amorphous silicon, $n^+$ amorphous silicon, and finally Cr source and drain electrodes.  These transistors were patterned into isolated islands, connected after spherical deformation by shadow-masked metal evaporation [108].  Here, the active devices were based on amorphous silicon, which can be used for solar cells but is not capable of reaching the efficiency of single crystalline cells.

Ko et al. developed a hemispherical electronic eye camera with the goal of reducing aberrations.  An array of photodiodes and pn junction didoes were created on SOI wafers and electrically connected, using design strategies that allowed for compression and stretching of at least 50%.  First, a thin PDMS structure was created that in its relaxed state was dome-shaped, but that could be stretched to form a planar sheet that they called a “drumhead”.  The array of silicon photodiodes was created on SOI wafers, with compressible metal interconnects and polymer posts connected through the buried oxide to the underlying silicon.  The buried oxide was etched in HF, leaving an array of photodiodes that were only loosely connected to the substrate.  The sufficientlysticky PDMS drumheads were pressed onto the photodiode arrays, which were removed from the handle wafer. When the drumhead radial tension was released, the PDMS returned to its hemispherical shape with the diode array attached. Most of the strain resulting from this deformation would be transferred to the metal interconnects in the form of significant outward bowing. The PDMS with attached silicon photodiodes could be pressed against a glass mold with a photocurable adhesive and connected to external circuitry to form a camera [109].

Although a process similar to the one described above by Ko would have been acceptable for assembling solar cells onto lenses, the design approach shown here was intended to take advantage of previously developed strategies for assembling components onto PET sheets without the need for complex PDMS stretching and relaxing, and with simpler solar cell processing. Also, a solder-based assembly approach allows for easy integration of different types of components which could be necessary when creating a complete contact lens sensing system.

## 4.2 Multi-cell fabrication

Solar cells of 500 x 500 x 10 $\mu m^3$ were fabricated using highly doped p-type SOI wafers to ensure ohmic contact (Ultrasil Corporation, 0.01 – 0.02 Ohm-cm p-type, 10 µm device thickness (Figure 17a). First, wafers were cleaned in 3:1 $H_2SO_4$:$H_2O_2$, 49% HF, and then 5:1:1 $H_2O$:HCl:$H_2O_2$. Then, 350 nm of wet thermal silicon dioxide was grown and patterned using a photoresist mask (MicroChemicals GmbH, AZ4620) and reactive-ion etching. The patterned oxide acted as a diffusion barrier for a phosphorus spin-on-dopant (Filmtronics, Inc., P509), which was used to create n-type emitters (Figure 17b). Oxide and spin-on-dopant were stripped in 49% HF, and Cr/Ni/Au (15/50/200 nm, respectively) was deposited for p and n electrical contacts using photolithography, electron beam evaporation, and lift-off (Figure 17c). Cell widths and lengths (500 µm x 500 µm with chamfered corners) were defined with photoresist (AZ4620), and E isolated individual cells (Figure 17d). After photoresist stripping with oxygen plasma in a barrel etcher, polydimethylsiloxane (PDMS, Dow Corning Corporation, Sylgard 184 Silicon Elastomer Kit) was spin-coated on the processed SOI wafer and onto a bare silicon wafer.

To minimize thickness variations caused by edge beads and etched trenches, wafers were left on a flat surface to planarize for several hours before curing overnight in a vacuum oven at 85ºC.  Next, both wafers were placed under low-power oxygen plasma for 30 seconds to prepare the surfaces for bonding.  Upon removal, wafers were immediately pressed together to form a strong bond (Figure 17e).  Using DRIE, the entire SOI handle wafer was etched, and then was etched the buried oxide using buffered oxide etchant (Figure 17f). Lastly, PDMS was etched in 3:1 n-methyl pyrrolidone:tetrabutylammonium fluoride (Sigma-Aldrich Co LLC) and rinsed thoroughly in deionized water, resulting in a collection of freestanding solar cells (Figure 17g).  For a more detailed process, please refer to Appendix B:.

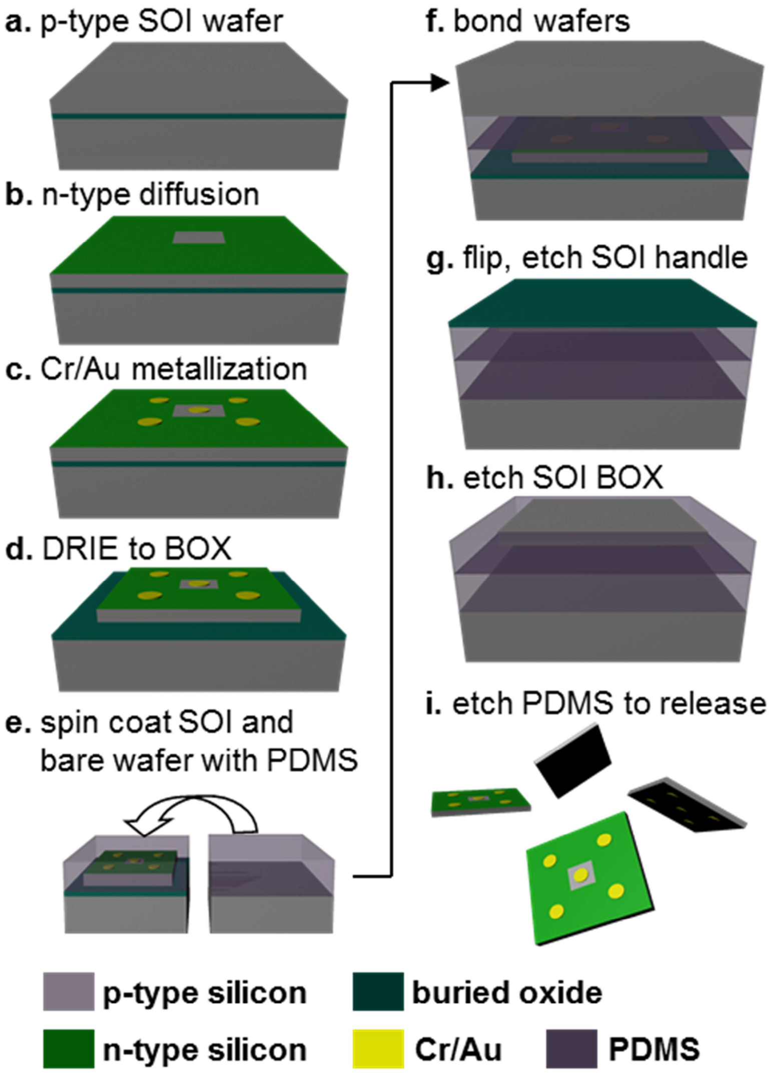

**Figure 17. Fabrication process for freestanding, back-junction, single-crystalline silicon solar cells.**

## 4.3 Multi-cell results and characterization

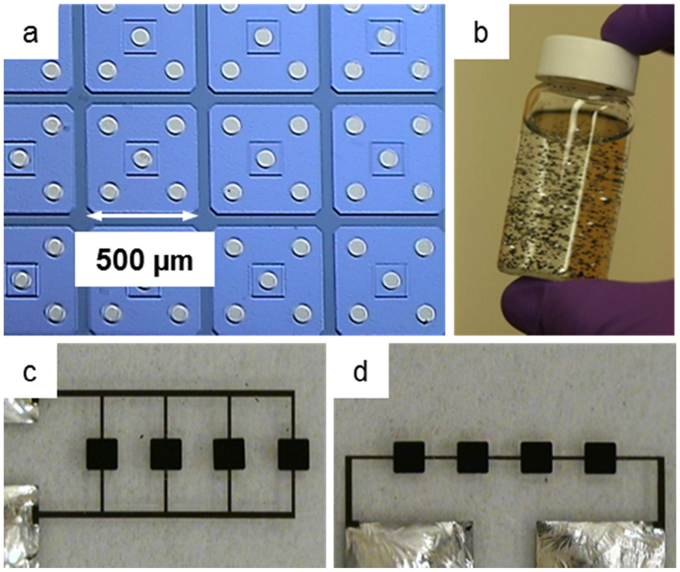

**Figure 18. Multi-cell approach fabrication and assembly results. a) Microscope image of micro solar cells on a handle wafer after metallization and DRIE, prior to release. On each cell, a central p contact is surrounded by four n contacts, ensuring operation in any orientation after assembly on the contact lens. b) Released solar cells stored in deionized water. c) Microscope images of four cells assembled in parallel and d) four cells assembled in series.**

Solar cells were characterized using an Oriel solar simulator, which comprises a xenon lamp coupled to a set of filters to approximate AM1.5 illumination. Output intensity was calibrated to 100 mW/cm$^2$ using a Hamamatsu S1787-12 photodiode. Maximum power conversion efficiency of 1.24% occurs at 310 mV (Figure 19) with a fill factor of 0.67. The mean short circuit current was 11.5 µA with 1.8 µA standard deviation. Series and parallel configurations of assembled solar cell arrays were tested using the same illumination, the result of which can be seen in Figure 20. Using series and parallel configurations allows for application dependent voltages and currents.

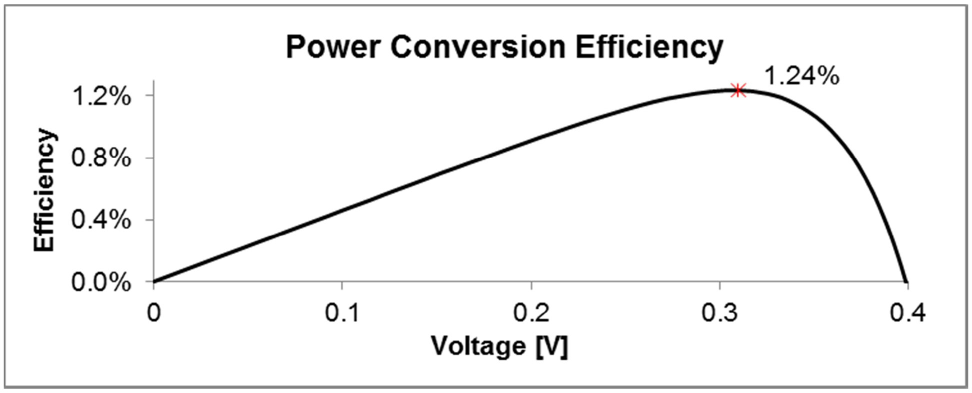

**Figure 19. Measured power conversion efficiency as a function of voltage at AM1.5 (100mW/cm$^2$).**

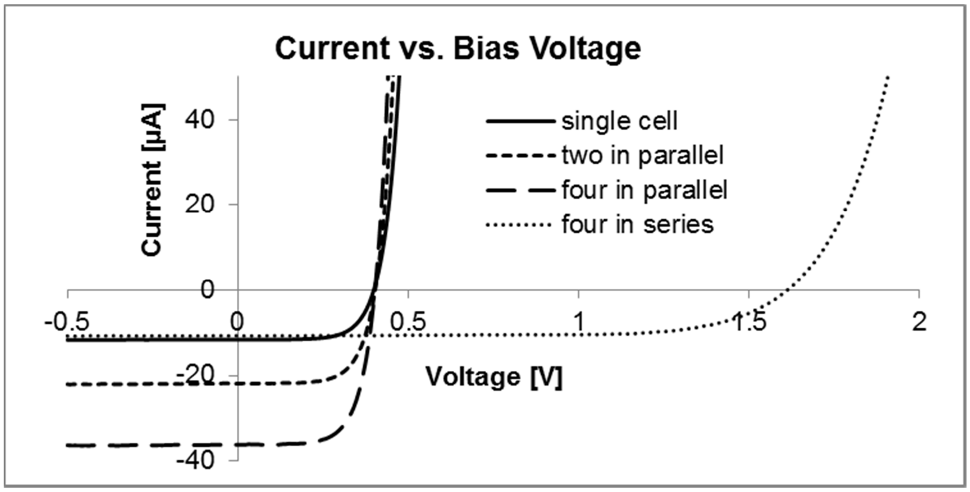

**Figure 20. Measured current vs. bias voltage of arrays of assembled micro solar cells at AM1.5.**

Responsivity was measured using the setup depicted in Figure 21. White light from an Oriel 77501 source (shown in yellow for clarity) passed through a chopper (Stanford Research Systems, Inc., Model SRS40) operating at 100 Hz and then into a Czerny-Turner-type monochromator (Action Research Corporation, SpectraPro-275). The narrowband output (red) was focused onto a photovoltaic device under test (DUT). The DUT output was connected to a lock-in amplifier (Stanford Research Systems, Inc., Model SR810 DSP Lock-In Amp) triggered at the chopper frequency. To eliminate overlapping order effects from the monochromator diffraction grating, an order-sorting filter with a cutoff wavelength of 530 nm was placed in the optical path when measuring

525 nm and above. Thus, two scans were performed for the calibrated diode and for each solar cell: one ranging from 400 to 600 nm without an order-sorting filter, and a second filtered from 525 to 1100 nm.

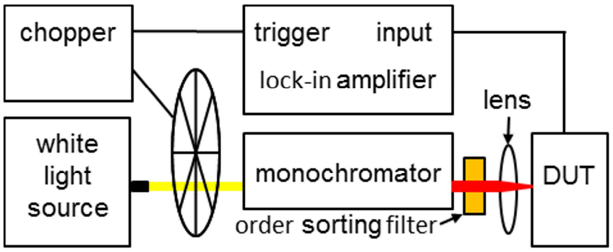

**Figure 21. Setup to measure responsivity as a function of wavelength. White light (yellow for clarity) modulated with a chopper was sent into a monochromator. The narrowband output (red) passed through an order sorting filter and was focused onto a device-under-test (DUT). DUT short circuit current was measured using a lock-in amplifier triggered by the chopper. Measurements were taken from 400 to 1100 nm.**

First, the short circuit current ($I_{sc}$, [A]) of a known photodetector was measured (Newport Corporation, 818-SL) at wavelengths from 400 to 1100 nm at 25 nm intervals and divided by the corresponding calibrated responsivity [A/W] to determine light source optical power at each wavelength [W]. Next, $I_{sc}$ was measured for several assembled solar cells using the same experimental setup. Due to their small size, each cell was mounted on a three axis micro positioner and translated until $I_{sc}$ maximum was reached, and then kept in place for the remainder of each scan. Finally, solar cell responsivity was calculated by dividing measured $I_{sc}$ by the previously determined optical power and then normalized (Figure 22).

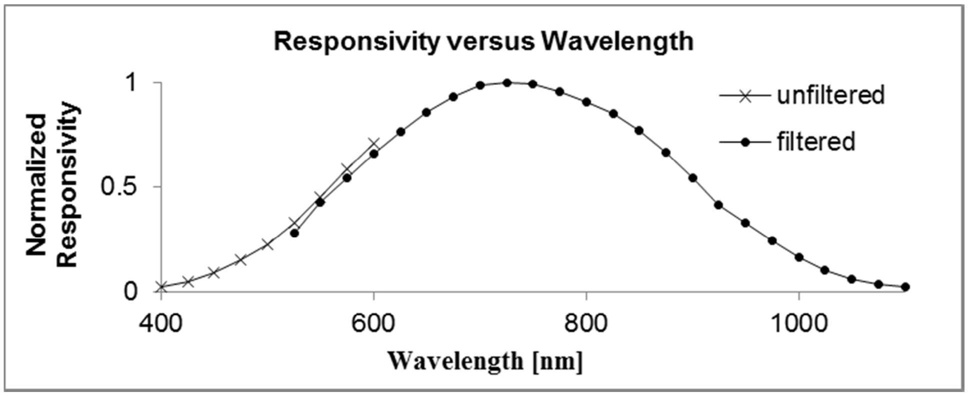

**Figure 22. Normalized cell responsivity. Peak responsivity was at approximately 725 nm; shorter wavelength light absorbed near the surface, far from the depletion region, and longer wavelength radiation passed through the cell.**

In preparation for further testing of complete contact lens systems with embedded sensors and circuitry, a 2 x 12 array of solar cells was molded and parylene coated for *in vivo* fitting on a rabbit cornea. Experiments were conducted in a manner similar to that presented in section 2.2.4 (Figure 23).

**Figure 23. Image of a contact lens with a 2 x 12 solar cell array placed on a live rabbit eye.**

## 4.4 Flexible solar cell design

The multi-cell approach described above was designed to test an assembly and integration scheme, without significant attention to power conversion efficiency. Hence, fabrication was as simple as possible: three masks were used, a single oxidation, one diffusion process, and one metallization. In addition, modeling was not used to determine the effect of doping levels, cell thickness, or surface recombination. This approach resulted in poorly performing solar cells with low output power (essentially zero at low light levels). Additionally, although this verified that solar cells could be assembled onto a polymer substrate, yield was inversely proportional to the number of cells assembled. The process described in section 2.4 was very reliable for one or two components, but decreased as the number of components increased. Furthermore, to cover a large area, the cell spacing would necessarily decrease, making manual assembly more difficult. Although self-assembly of chips of this size is achievable, a single, large cell would be more appropriate for this application because of the area coverage and the ease of assembly.

Before fabricating solar cells, several shapes of silicon pieces were etched and released from SOI wafers and wrapped around a mold (7.1 mm radius of curvature) to ensure they were sufficiently flexible. Three designs were tested: 1) concentric rings, 2) single meander, 3) double meander, at 10 and 20 µm in thickness. The 10 µm devices were more flexible and had better yield when deformed over the mold, while the single meander devices were vastly more reliable than the double meander devices. From these experiments, it was determined that the rings and the single meander devices would be used for the solar cells. The single meander was designed to allow for spherical deformation by essentially transforming a three-dimensional stretching problem into a two dimensional bending problem. Each radial finger bends easily in two dimensions provided the thickness is limited. After generally determining device design, cells were simulated to determine which parameters would have the largest impact on cell performance.

## 4.5 Simulation using Synopsis Sentaurus

Interdigitated back contact solar cells require at least two dimensional models to determine even the most basic functionality because of lateral currents in both the emitter and base. Synopsis Technology Computer Aided Design tools were used for simple 2D solar cell simulations. Knowledge gained from these endeavors, coupled with the availability of processing technology and personal experience, led to the fabrication process presented in section 4.6.

### 4.5.1 Back contact solar cell simulation review

Lu et al. used Sentaurus device to model interdigitated back contact silicon heterojunction cells. The effects of front surface passivation and also of n to p strip width were examined. As expected, low front surface recombination velocities were required for high efficiency, as most of the carriers were created near the front surface. Also, the efficiency increased with increasing emitter coverage over the simulated range, because light impinging over the base (in this case n-type regions) created carriers requiring lateral and vertical diffusion to reach a junction [110].

Kluska et al. presented a modeling approach to calculate the effect of design parameters on loss mechanisms of one sun industrial back contact back junction cells. Specifically, they modeled approaches for determining short circuit current density, non-intrinsic saturation current density, and series resistance. In doing so, it was found that electrical shading loss, or “shading-like” loss above base regions, was minimized with a greater fraction of emitter coverage. For their cell design, it was determined that the electrical shading could be avoided with base widths less than 100 µm. It was determined that maximum efficiency with a set minimum for base width (600 um) was strongly determined by pitch and a tradeoff between electrical shading and series resistance. For example, it was determined that a pitch of 3000 µm was acceptable for the lower resistivity silicon of 1 Ohm-cm, while 2000 µm was better for 8 Ohm-cm silicon.

Nichiporuk et al. used DESSIS to perform 2D and 3D numerical simulations of IBC solar cells while varying width of doped n+ and p+ regions, depth of doping, distance between diffused regions, substrate resistivity and recombination, and surface recombination on both surfaces. SRH recombination, band gap narrowing, doping-dependent lifetime, Auger recombination, and doping dependent mobility were used in conjunction with AM1.5G solar spectrum for simulation. Emitter doping greater than $10^{19}/cm^2$ was required to keep the pn built-in potential high. It was also found that dark current can increase because of strong recombination at the contacts if the emitter and BSF regions are thinner than around 1 um. Additionally, the importance of emitter coverage and the spacing between emitter and base was emphasized [111].

### 4.5.2 Simulation setup

Sentaurus Process (SProcess) is a multidimensional simulator for device fabrication. It can simulate oxidation, etching, deposition, annealing, photolithography, and diffusion, and outputs files that contain meshed geometries, materials, doping profiles and other pertinent information for use in electrical and optical simulations. Command files contain an initial simulation domain, remeshing strategies, and various processing steps. By properly preparing a command file, simulation can mimic real processing.

Sentaurus Device (SDevice) takes input about a semiconductor and uses various physical models to simulate electrical and optical characteristics. SDevice takes mesh files, parameter files, and spectrum files as inputs. Mesh files contain information from SProcess about device geometry, material types, doping concentrations, etc, and parameter files included specific information about materials and interfaces. For this simulation, n-k parameter files were included with real and imaginary absorption coefficients, as well as files to define the surface recombination at various material interfaces.

Sentaurus Workbench (SWB) allows for optimization by parameterizing variables in SProcess and SDevice. Two major simulations were conducted, one in which a large number of parameters were varied using a broad range of reasonable values with a representative BJBC cell designed for fast simulation. In SWB, cell wafer doping, thickness, implant energies, implant doses, and front and back surface passivation were varied. A second simulation was conducted to with specific values from the first experiment, and applied to a realistic cell of dimensions that were constrained by fabrication in the MFF cleanroom. The basic cell geometry used in both experiments comprised a front surface $SiO_2$ coating (shown on the bottom), an n-type base, and a boron-doped emitter, with metal point contacts through silicon nitride backside passivation (Figure 24).

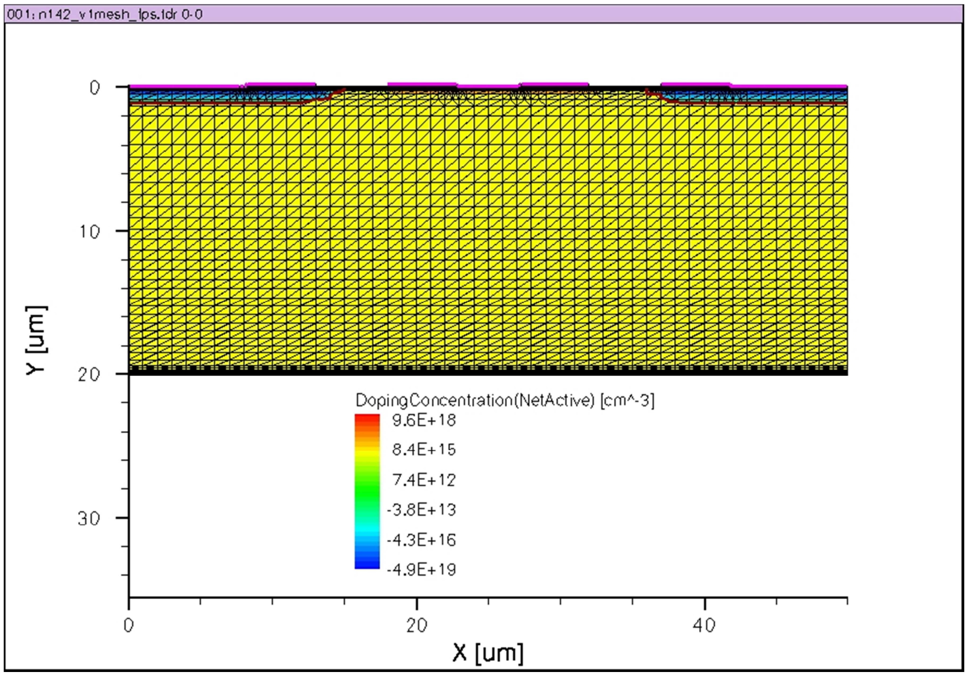

**Figure 24. Example of simulated cell structure for multivariable parametric sweep.**

### 4.5.3 Simulation results

The first experiment verified that the primary factors affecting efficiency in a back contact cell are the front and rear surface passivation, as demonstrated in Figure 25. With reasonably good front and rear surface passivation, simulated efficiency reached nearly 10% for a variety of other processing conditions. Cells of 20 µm in thickness were on average slightly more efficient than 10 µm cells. Substrate doping (0.1, 1, 10 Ω-cm phosphorus), implant energies (10, 40, 80 keV for phosphorus, 10, 40 keV for Boron), implant doses ($10^{14}$/cm$^3$, $10^{15}$/cm$^3$ for both boron and phosphorus), and diffusion times had less of an effect. However, the cell simulated was unrealistically small in lateral dimensions, and also tighter meshing near the implants may have revealed a larger dependence.

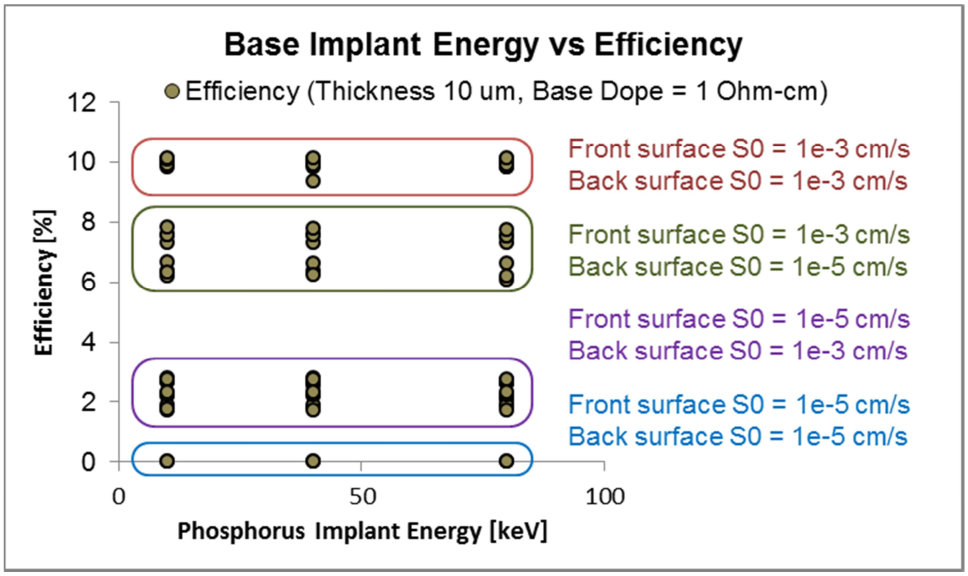

**Figure 25. Base implant energy versus efficiency. For a cell with a specific thickness and base doping, the major factor affecting efficiency was determined to be the front surface recombination, and the second most important factor was the rear surface recombination. Parameters not specifically listed were: emitter implant dose, emitter implant energy, and diffusion time, which account for the closely bundled data points within the larger groupings.**

Using a more realistic cell structure (i.e. larger separation between pads, larger area, and much tighter meshing), front and rear surface recombination were varied with other processing parameters as constants. Reasonably high cell efficiencies were observed for cells with front surface recombination velocities below $10^4$ cm/s, even with very poor rear surface passivation. The values used in this experiment were identical to those used in device fabrication (Table 3).

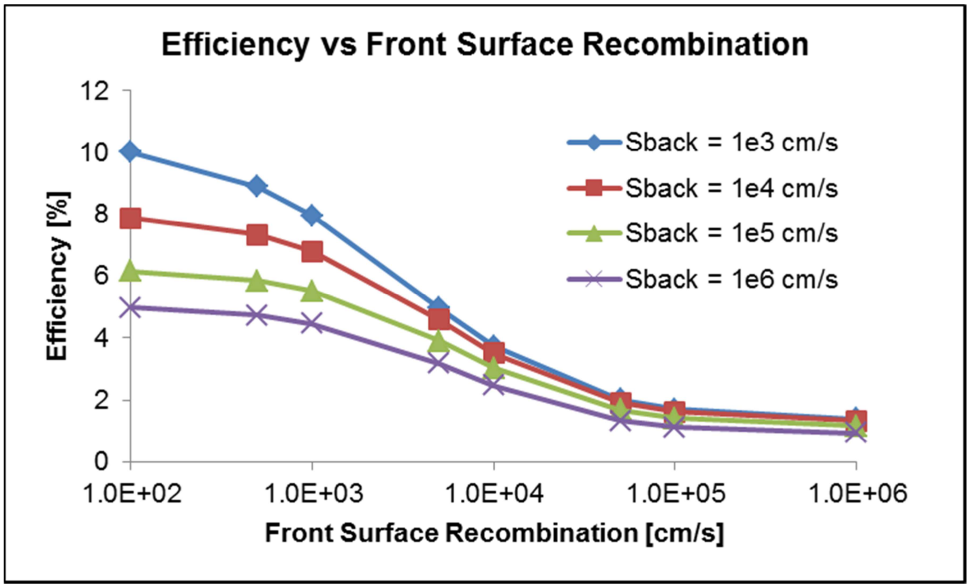

**Figure 26. Efficiency vs front surface recombination. With exceptional front surface recombination (100 cm/s), the efficiency of this cell could be above 5%, with up to 10% achievable with good back surface passivation. As the front surface recombination increased, the effect of rear surface passivation was lessened and the cell efficiency dropped substantially.**

**Table 3. Parameters used in the simulation of a realistic solar cell. The parameters given below used in simulation were very close to those of the fabricated solar cells.**

| Parameter | Value | Unit |
|---:|:---:|:---:|
| SOI Device Layer Thickness | 15 | µm |
| Substrate Resistivity | 5 | Ω-cm |
| Phosphorus Implant Energy | 65 | keV |
| Phosphorus Implant Dose | 7.0E+15 | P/cm3 |
| Boron Implant Energy | 23 | keV |
| Boron Implant Dose | 7.0E+15 | B/cm3 |
| Implant Angle (B and P) | 7 | degrees |
| Diffusion Time | 2, 6 | minutes |
| Diffusion Temperature | 1100 | Celsius |

### 4.5.4 Simulation limitations

Unlike many solar cell applications, where light levels are reasonably constant or at least predictable, a solar cell on contact lens will have a highly variable environment. First, while wearing a contact lens, the amount of light impinging upon the solar cell will vary across the cell. In most common situations, whether indoors or out, the direction of highest intensity is up. Therefore, it could be expected that the top of the solar cell would receive the most light. However, this may be offset by occlusion from the eyelids or lashes, and certainly would change depending on the direction of the wearer's gaze. Therefore, simulating a small portion of the cell with uniform illumination may neglect many effects from partially illuminated cells.

Additionally, output from solar cells placed on the eye would vary because of the constantly changing conditions of the eye itself. For example, the natural response to increasing light levels is to squint, which would result in more cell occlusion. However, this would only occur in very bright light where sufficient power would probably be available from a smaller area. Additionally, the penetration depth of red to near IR light in the skin, particularly the thin eyelids, is significant, and this would likely correspond to the highest responsivity of the thin crystalline cells. Furthermore, in addition to a biocompatible coating, the tears would cover the lens in a non-uniform manner, which makes simulation of a dielectric anti-reflection layer moot. The index of refraction of human tears is about 1.33 – 1.34 [112] and has a thickness of ~10 µm [113]. However, the thickness can vary significantly (4-10 um), especially between those who normally wear contact lenses and those who do not [114]. Hence the reflection from the solar cell front surface is highly variable, and the primary purpose of the front surface dielectric should be surface passivation.

A last practical reason why simulations will not be precise is that it is difficult to exactly match the fabricated parameters to the simulation. For example, when etching through the handle wafer of the SOI, loading effects can cause uneven etching of the Si, and non-infinite Si/SiO2 selectivity means that oxide will be thinner for devices on the edge of the wafer than in the center. Therefore, the reflection and optical generation will be different. Metal-semiconductor interfaces are also hard to predict unless the cleanroom laboratory and deposition conditions are well controlled.

## 4.6 Flexible solar cell fabrication

SOI wafers were purchased from Ultrasil, nominally 1-5 Ω-cm, with a measured average resistivity of 3.9 Ω-cm. The wafers underwent a standard RCA clean and alignments marks were etched into the silicon, necessary because implants often do not give rise to significant contrast for use with contact lithography systems. The 275 nm alignment etch was carried out in a reactive ion etcher (RIE) for good visibility in contact aligners.

After etching alignment marks, the resist was stripped and wafers were cleaned before a second lithography for implant masking. Implant processing is convenient because oxide growth is not necessary. Normally, a thin layer of photoresist (~1.5 µm) is sufficient to mask a low energy, shallow implant, whereas diffusion processes often require thick thermal oxide. Patterned wafers were sent to Core Systems for implantation. High implant doses and low energies were used, because previous experience annealing the Ti/Ni/Au layers resulted in very poor results and complete degradation of assembly reliability. Therefore, it was necessary to have high surface concentrations to ensure good ohmic contact without annealing. After the $n^+$ implant, wafers were again cleaned and patterned, and sent back to Core Systems for emitter implantation. During both implants, bare n-type wafers with similar starting resistivity (~6.5 Ω-cm vs 3.9 Ω-cm) were included for ease of measuring the sheet resistance using a four point probe. After rapid thermal annealing for dopant activation, sheet resistivity for the phosphorus implant was 13.6 Ω/sq, while the boron emitter measured 26.2 Ω/sq.

The back surface was passivated with PECVD nitride in a manner similar to that used in [103]. The temperature was set to 350 ºC and a ratio of either 2:1 or 6:1 ammonia to silane was employed during a 10 minute deposition at high frequency. After via etching, the wafers were cleaned and patterned using a negative resist specifically designed for lift-off processing (NR71-1000PY, Futurrex). Then wafers were dipped in buffered oxide etchant for 30 seconds, dump rinsed, dried, and immediately placed under vacuum in the electron beam evaporation deposition chamber. A metallization of Ti/Ni/Au was chosen to provide low resistance, ohmic contact, and a surface for low temperature solder assembly. After deposition, the majority of the metal was removed in acetone, while a small fraction around the edges where the SOI device layer met the handle wafer required sonication to remove. After sonication, small bits of metal remained on the wafer and were removed in deionized water with a small amount of surfactant.

The device layer was etched using DRIE masked with AZ4620. The cell was etched to the buried oxide, and then the buried oxide, initially 500 nm thick, was partially etched to a thickness of ~150 nm in a parallel plate RIE using a standard oxide etch. The 150 nm of oxide was left so that the ICP etcher would not be exposed to the PDMS.

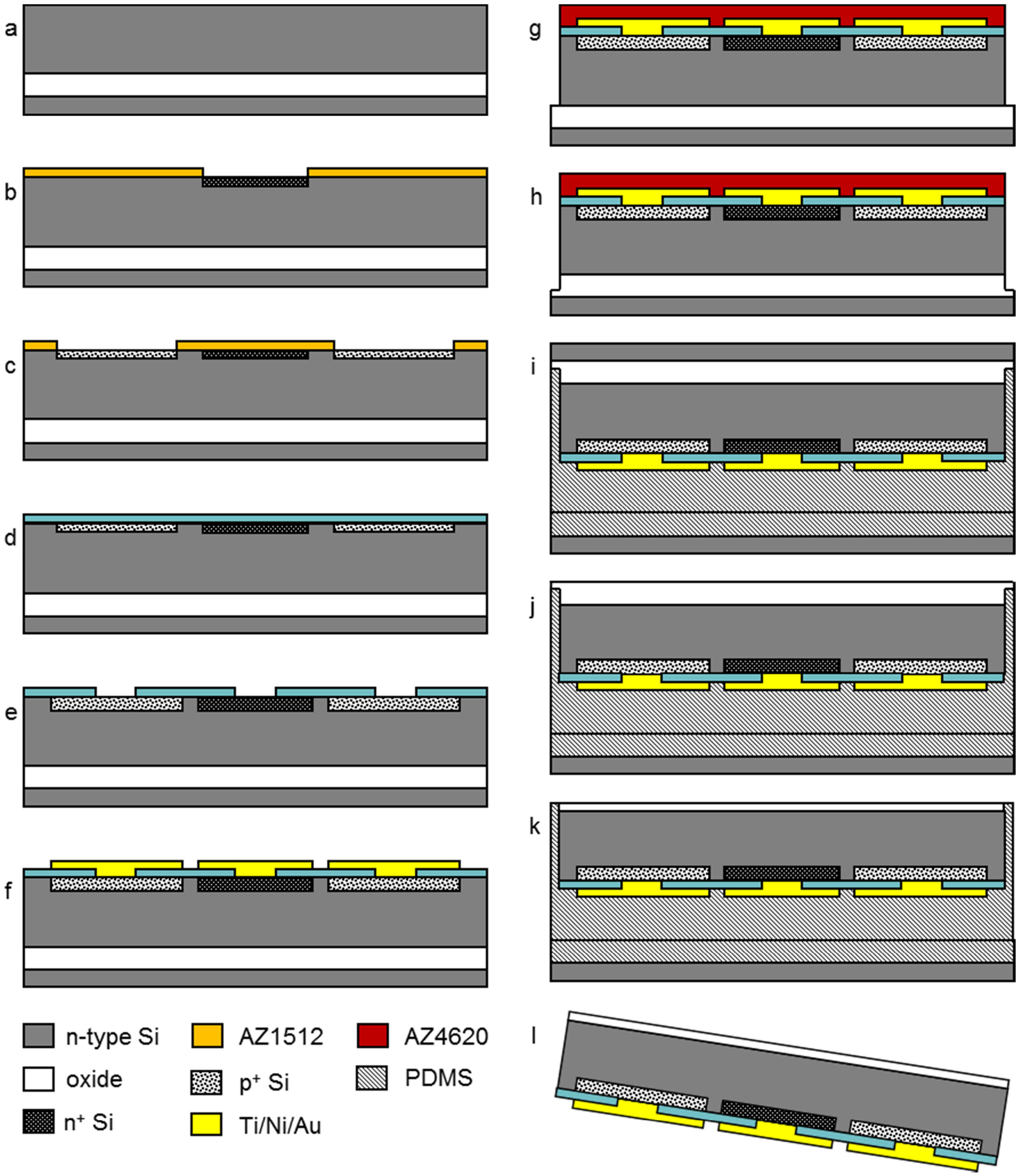

**Figure 27. Fabrication process for flexible solar cells. a) N-type SOI wafer. b) Photoresist mask and n$^+$ implant. b) Photoresist mask and p$^+$ implant. d) Nitride growth. e) Drive-in and via etch. f) Ti/Ni/Au deposition and patterning. g) Photoresist mask and DRIE etch to buried oxide. h) Partial etch of buried oxide. i) PDMS bond to silicon wafer and flip over. j) SOI handle wafer etch. k) Buried oxide thinning, which also totally etches previously thinned oxide. l) PDMS etch to release devices.**

Next, PDMS was spun on a bare silicon wafer and over the solar cell device layer, and then wafers were set on a horizontal surface for 24 hours to planarize, after which time the wafers were baked at 65 ºC for 2 hours. After baking, the wafers were placed in a low power barrel etcher (25 W) for a short time (30 s). Immediately the wafers were pressed. Initially, wafers were sandwiched between two glass plates while applying a significant amount of pressure. However, because of the edge bead, this method did not produce good bonding across the wafer, and many of the devices cracked or broke after the handle wafer etch step. To achieve a better bond, the SOI wafer was placed face up on a glass plate, and the bare wafer with PDMS was placed face down. A cleanroom mask wipe was place on the back surface of the bare wafer, and pressure was applied primarily to the center of the wafer. Then the wafers were placed in a vacuum oven at 80 ºC overnight to ensure void-free bond.

Reactive ion etching was selected to etch the handle wafer of the SOI. Although normally this is not used for etching an entire, unmasked wafer, it was determined that this was the most reliable and simplest method available. Initially a standard silicon DRIE was used, but this resulted in extremely poor uniformity across the wafer because of loading; the etch rate at the center was approximately 80% the etch rate near the wafer periphery. Therefore, for a 450 µm etch, the handle wafer, the buried oxide, and the device layer were etched completely at the edges before the handle wafer in the center was completely removed. Therefore, an etch process with an extremely high oxide selectivity was developed, the details of which are presented in Appendix D:. One option to achieve better $SiO_2$ selectivity is to use cryogenic etching with $SF_6/O_2$-based high density plasma [115]. This was not feasible due to the PDMS bond layer. The high pressure (35 mTorr), high flow $SF_6$ recipe achieved that was developed achieved an etch selectivity of greater than 1000:1 for $Si:SiO_2$. Despite the excellent oxide selectivity, the thickness across the wafer varied significantly (Figure 28). After the handle wafer was completely etched, the oxide was thinned to ~100 nm to remove the all oxide between the cells while leaving an AR coating over the silicon devices. Oxide thicknesses afterward ranged from ~40 to ~120 nm.

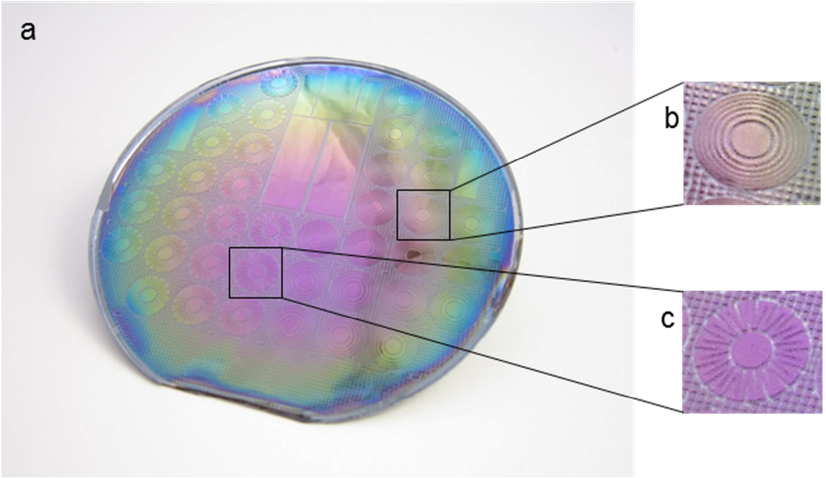

**Figure 28. Solar cells after etching the SOI handle, prior to oxide thinning. a) On the wafer scale, the variation is oxide thickness is apparent from the color of the reflection. The wafer oxide is substantially thinner on the edges (blue) than in the center (red). b) Inset showing a magnified view of the concentric ring design. c) Inset showing a magnified view of the single meander design.**

As with the multi-cell process, components were released in 3:1 NMP:TBAF. However, unlike the small parts that could be easily filtered, the larger parts (~1 cm diameter), would stick together, interweave with one another, or stick to the filter paper. Therefore, a release assembly was designed using SolidWorks that was machined by the University of Washington Physics Machine Shop. The device consisted of a thick PTFE base with ridges to hold a standard wafer, pyramids directly under each component, and two screw holes to attach handles. The system also had two handles for easy removal and a lid to hold the released components in place while rinsing Figure 29. After rinsing, cells were dried, placed in individual containers, and assembled using pseudo self-assembly methods presented earlier. For a detailed fabrication process for the flexible cells, please refer to Appendix C:.

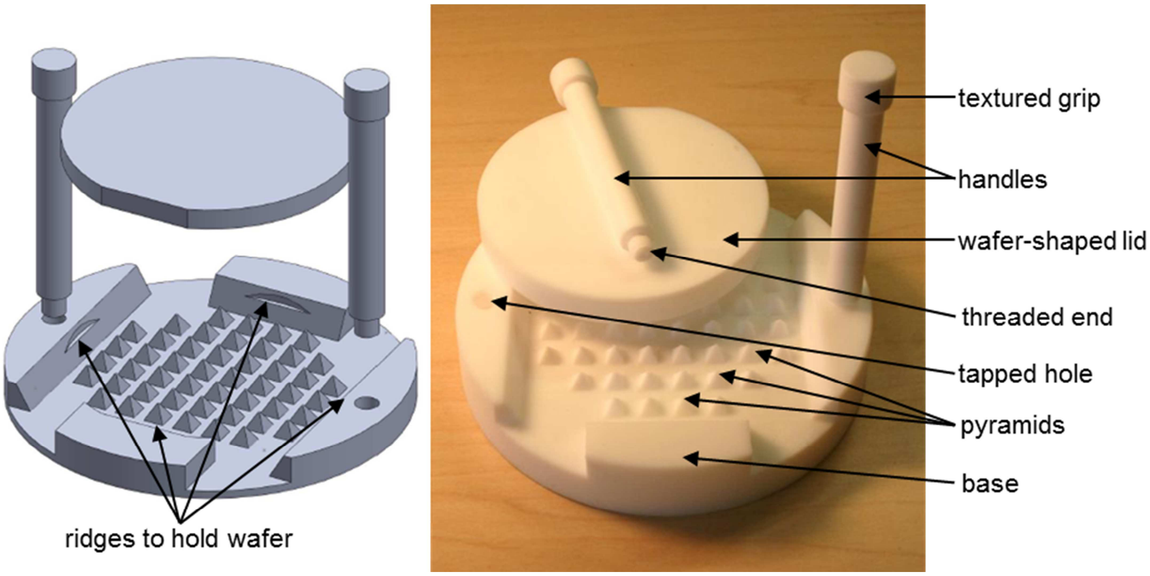

**Figure 29. SolidWorks model and machined PTFE holder to catch cells released from 100 mm wafers. The assembly base held wafers face down, with solar cells directly over PTFE pyramids. When the solar cells were released from the wafer, a heavy, wafer-shaped lid held them in place during rinsing. Screw-on handles were included for easy carrying.**

## 4.7 Flexible solar cell testing

Four designs were incorporated into the solar cell wafer: two slightly different meandered designs and two sets of concentric rings, one with four rings and another with six. Each design had a minimum radius of 2 mm (to leave the pupil unobstructed) and a maximum radius of 5 mm (to fit within a contact lens). The area of each concentric ring was designed to be equal, such that the radial width of each cell decreased toward the contact lens periphery. Ideally, each cell would then produce equal current. The first meandered structure (Type 1) was designed such that after molding the gap between radial fingers would be 200 µm, and the second was designed with slightly more room between fingers (Type 2). After release, meandered devices were easy to handle and store, but concentric rings were unusable. Presumably because of stress in the deposited films, the concentric rings either bent significantly, making it impossible to assemble, or they broke or stuck together. Therefore, all cells tested were of the two meandered designs.

### 4.7.1 One Sun efficiency

First, the solar simulator was calibrated to AM1.5 using a calibrated photodiode. A total of eight meandered cells were assembled and tested, from two slightly different processes and two cell designs (Table 5). For detailed differences in the processing and design, see Appendix B:. Briefly, in Process1 rapid thermal annealing for dopant activation took place in an oxygen environment directly after implant and cleaning, and afterward the back surface nitride was deposited. In Process2, the back surface nitride was applied first, and then the wafers were annealed. As mentioned above, the primary difference between types was that the spacing between silicon meanders was larger for Type 2 cells. Some other variations in the cell design by type are given in Table 4.

**Table 4. Cell area and percent coverage of base, emitter, via, and metal.**

| Type1 | Area [cm2] | Coverage [%] | Type2 | Area [cm2] | Coverage [%] |
|---|---|---|---|---|---|
| Area | 0.55680 | 100.000 | Area | 0.50640 | 100.000 |
| Base | 0.22473 | 40.362 | Base | 0.16444 | 32.472 |
| Emitter | 0.19558 | 35.125 | Emitter | 0.21263 | 41.989 |
| Via | 0.03800 | 6.825 | Via | 0.06749 | 13.327 |
| Metal | 0.42029 | 75.483 | Metal | 0.37707 | 74.461 |

Averages for short circuit current density, fill factor, and efficiency were 3.15 mA/cm$^2$, 0.557, and 0.36%, respectively. The efficiency varied substantially, from 0.28% to 1.32%. One reason for the low efficiency was very poor open circuit voltages. As shown in Table 5, the average open circuit voltage was 362 mV, with an 8.7 mV standard deviation. Normally, poor open circuit voltages are attributed to unacceptably low shunt resistance, meaning that there is a low impedance leakage path to ground. This could be the result of shunting across the junction at the silicon surface. Also, although a cursory examination of the short circuit current density and the open circuit voltage in Table 5 shows little correlation between open circuit voltage and current density, the low values of current density could cause low open circuit voltages. Lastly, low open circuit voltages could also be indication of very high saturation current.

**Table 5. Cell measurements for all flexible cells under AM1.5 conditions.**

| | Voc [V] | Isc [mA] | Pmax [mW] | Jsc [mA/cm2] | Fill Factor | Efficiency [%] | Normalized Eff. |
|---|---|---|---|---|---|---|---|
| Process1 Type1 Cell1 | 0.3570 | 0.6920 | 0.1560 | 1.2428 | 0.6314 | 0.2802 | 0.2125 |
| Process1 Type1 Cell2 | 0.3535 | 1.0930 | 0.2380 | 1.9627 | 0.6158 | 0.4273 | 0.3240 |
| Process1 Type1 Cell3 | 0.3576 | 0.7680 | 0.1230 | 1.3802 | 0.4493 | 0.2218 | 0.1682 |
| Process1 Type2 Cell1 | 0.3568 | 1.7140 | 0.3620 | 3.0778 | 0.5917 | 0.6498 | 0.4928 |
| Process1 Type2 Cell2 | 0.3649 | 3.0880 | 0.6680 | 6.0980 | 0.5926 | 1.3186 | 1.0000 |
| Process2 Type1 Cell1 | 0.3708 | 1.1900 | 0.2590 | 2.1364 | 0.5881 | 0.4659 | 0.3534 |
| Process2 Type1 Cell2 | 0.3786 | 1.9540 | 0.3720 | 3.5096 | 0.5033 | 0.6688 | 0.5072 |
| Process2 Type2 Cell1 | 0.3737 | 2.9410 | 0.5350 | 5.8082 | 0.4868 | 1.0567 | 0.8014 |
| Total Ave. | 0.3641 | 1.6800 | 0.3391 | 3.1520 | 0.5574 | 0.6361 | 0.4824 |
| Total Stdev | 0.0087 | 0.8690 | 0.1750 | 1.7712 | 0.0631 | 0.3562 | 0.2701 |

The fill factor and open circuit voltage are mostly independent of cell process or type (although Process2 has slightly higher open circuit voltage), so the large variation in efficiency is primarily due to short circuit current density. One explanation for the differences in short circuit current density is the fact that oxide thickness was not well controlled. To determine this effect, the reflectance at normal incidence for light from 300 to 1100 nm was calculated with oxide thickness as a parameter ranging from 50 to 150 nm using realistic values for the index of refraction of air, oxide, and silicon as a function of wavelength. Then the total transmission of the AM1.5 spectrum was calculated using these reflectance values. The results, shown in Figure 30, indicate that the difference in oxide thickness could change the total transmission of light into the cell from about 75% to 85% in reference to a perfect antireflection coating (Figure 30). Thus the worst short circuit current density would be ~88% of the maximum if only oxide thickness were considered. Therefore, differences in oxide thickness cannot completely account for the large variation in short circuit current density.

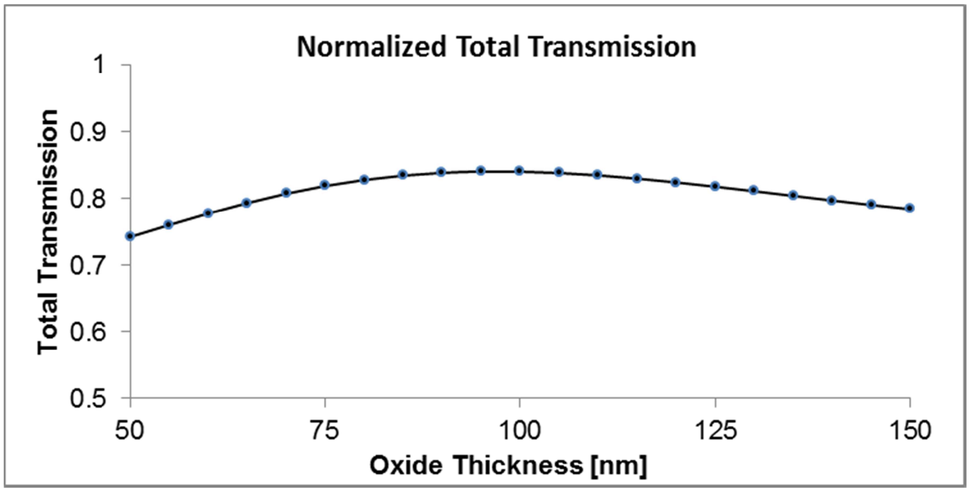

**Figure 30. Normalized total transmission into silicon calculated from reflection.**

We can further break down the differences between cells by separating them into cell type and process. The primary difference in efficiency is in relation to cell type, as seen in Table 6; in almost every case, the efficiency for Type 2 cells was higher than those of Type 1. This was likely due to larger emitter coverage (41% vs 35%, shown in Table 4) and corresponding higher short circuit current density. Ideally, the emitter coverage should have been designed to be much larger to allow for better current collection and higher current density. Aside from the emitter coverage, the differences between cells types were minor. Cell Type 2 was designed to be more forgiving of alignment errors and designed with slightly larger gaps between the silicon meandered structure for easier bending.

**Table 6. Cell measurements organized by cell design. Type2 cells had higher short circuit current densities and efficiencies, likely resulting from higher emitter coverage.**

| | Voc [V] | Isc [mA] | Pmax [mW] | Jsc [mA/cm2] | Fill Factor | Efficiency [%] | Normalized Eff. |
|---|---|---|---|---|---|---|---|
| Process1 Type1 Cell1 | 0.3570 | 0.6920 | 0.1560 | 1.2428 | 0.6314 | 0.2802 | 0.2125 |
| Process1 Type1 Cell2 | 0.3535 | 1.0930 | 0.2380 | 1.9627 | 0.6158 | 0.4273 | 0.3240 |
| Process1 Type1 Cell3 | 0.3576 | 0.7680 | 0.1230 | 1.3802 | 0.4493 | 0.2218 | 0.1682 |
| Process2 Type1 Cell1 | 0.3708 | 1.1900 | 0.2590 | 2.1364 | 0.5881 | 0.4659 | 0.3534 |
| Process2 Type1 Cell2 | 0.3786 | 1.9540 | 0.3720 | 3.5096 | 0.5033 | 0.6688 | 0.5072 |
| Type1 Ave. | 0.3635 | 1.1394 | 0.2296 | 2.0463 | 0.5576 | 0.4128 | 0.3131 |
| Type1 Stdev | 0.0096 | 0.4486 | 0.0872 | 0.8057 | 0.0699 | 0.1566 | 0.1188 |
| | Voc [V] | Isc [mA] | Pmax [mW] | Jsc [mA/cm2] | Fill Factor | Efficiency [%] | Normalized Eff. |
| Process1 Type2 Cell1 | 0.3568 | 1.7140 | 0.3620 | 3.0778 | 0.5917 | 0.6498 | 0.4928 |
| Process1 Type2 Cell2 | 0.3649 | 3.0880 | 0.6680 | 6.0980 | 0.5926 | 1.3186 | 1.0000 |
| Process2 Type2 Cell1 | 0.3737 | 2.9410 | 0.5350 | 5.8082 | 0.4868 | 1.0567 | 0.8014 |
| Type2 Ave. | 0.3651 | 2.5810 | 0.5217 | 4.9947 | 0.5571 | 1.0084 | 0.7647 |
| Type2 Stdev | 0.0069 | 0.6160 | 0.1253 | 1.3606 | 0.0497 | 0.2751 | 0.2087 |

A slight difference in cell performance was observed as a function of the fabrication process. In every case, the open circuit voltage was higher for Process 2, as shown in Table 7. Again, the main difference between processes was the order in which the back surface nitride was deposited. In Process 1, the dopants were activated in an RTA prior to nitride deposition, and in Process 2, the dopants were activated after nitride deposition. In Process 2, it is possible that the nitride acted to reduce out diffusion to keep the dopant concentrations at the surface higher than in Process 1. To first approximation, the built-in voltage is a function of the total dopant concentrations $N_a$ and $N_d$.

**Table 7. Cell measurements by organized by process. In Process1, the back surface nitride was deposited after annealing, and in Process2 the nitride was deposited before annealing. Process2 showed slightly higher open circuit voltages.**

| | Voc [V] | Isc [mA] | Pmax [mW] | Jsc [mA/cm2] | Fill Factor | Efficiency [%] | Normalized Eff. |
|---|---|---|---|---|---|---|---|
| Process1 Type1 Cell1 | 0.3570 | 0.6920 | 0.1560 | 1.2428 | 0.6314 | 0.2802 | 0.2125 |
| Process1 Type1 Cell2 | 0.3535 | 1.0930 | 0.2380 | 1.9627 | 0.6158 | 0.4273 | 0.3240 |
| Process1 Type1 Cell3 | 0.3576 | 0.7680 | 0.1230 | 1.3802 | 0.4493 | 0.2218 | 0.1682 |
| Process1 Type2 Cell1 | 0.3568 | 1.7140 | 0.3620 | 3.0778 | 0.5917 | 0.6498 | 0.4928 |
| Process1 Type2 Cell2 | 0.3649 | 3.0880 | 0.6680 | 6.0980 | 0.5926 | 1.3186 | 1.0000 |
| Process1 Ave. | 0.3580 | 1.4710 | 0.3094 | 2.7523 | 0.5762 | 0.5795 | 0.4395 |
| Process1 Stdev | 0.0037 | 0.8852 | 0.1974 | 1.7936 | 0.0652 | 0.3980 | 0.3018 |
| | Voc [V] | Isc [mA] | Pmax [mW] | Jsc [mA/cm2] | Fill Factor | Efficiency [%] | Normalized Eff. |
| Process2 Type1 Cell1 | 0.3708 | 1.1900 | 0.2590 | 2.1364 | 0.5881 | 0.4659 | 0.3534 |
| Process2 Type1 Cell2 | 0.3786 | 1.9540 | 0.3720 | 3.5096 | 0.5033 | 0.6688 | 0.5072 |
| Process2 Type2 Cell1 | 0.3737 | 2.9410 | 0.5350 | 5.8082 | 0.4868 | 1.0567 | 0.8014 |
| Process2 Ave. | 0.3744 | 2.0283 | 0.3887 | 3.8180 | 0.5261 | 0.7305 | 0.5540 |
| Process2 Stdev | 0.0032 | 0.7168 | 0.1133 | 1.5148 | 0.0444 | 0.2451 | 0.1859 |

### 4.7.2 Light intensity dependence

Light intensity dependence was testing using an AM1.5 solar simulator and a set of absorptive neutral density filers (Thorlabs, 25 mm SM1-Threaded Mount). Neutral density filters were mounted directly in front of the solar cells with minimal space in between. Three cells were tested using neutral density filters that ranged from ~80% transmission to 0.01% transmission, that were nominally neutral from 400 to 700 nm. To determine the actual intensity, AM1.5 spectral information ranging from 300 to 1100 nm in 5 nm increments was multiplied by the filter power transmission data in the same spectral range (Figure 31).

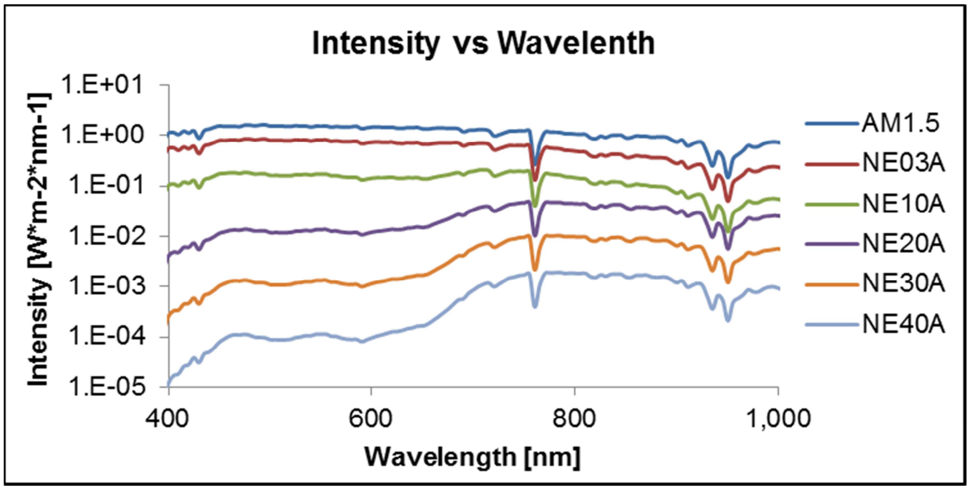

**Figure 31. Calculated intensity vs. wavelength for selected filters.**

As seen in Figure 31, the intensity reduction in the 700 to 1100 nm range was less than in the 400 to 700 nm range. The total intensity given as the x axis for figuresFigure 32, Figure 33, Figure 34, and Figure 35 does not take into account the fact that the responsivity is better for deeper penetrating wavelengths. However, this method of total intensity integration was more accurate than only using the nominal filter values as the independent variable.

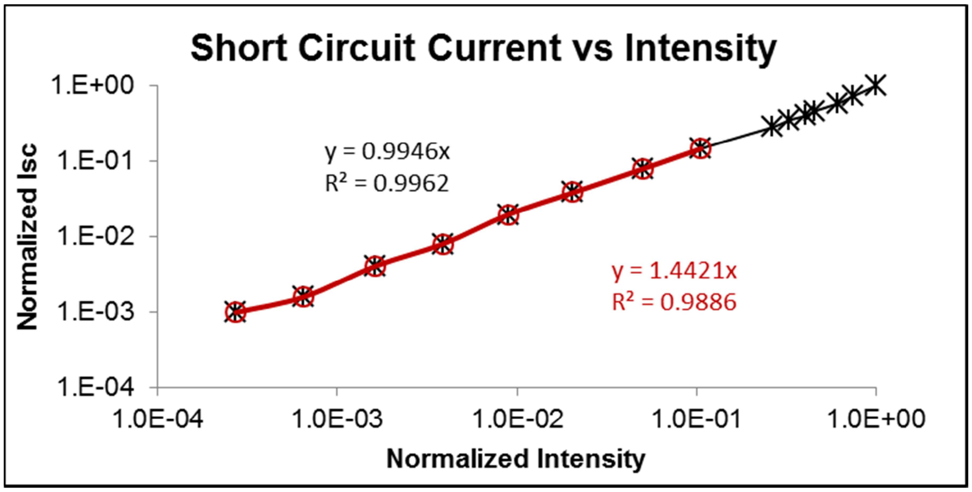

**Figure 32.Normalized short circuit current vs normalized intensity, three cell average.**

As expected from equation 3.26, the short circuit current showed a very close linear relationship with intensity. However, this relationship was different when examining only the normalized intensities from about 0.001 to 0.1.

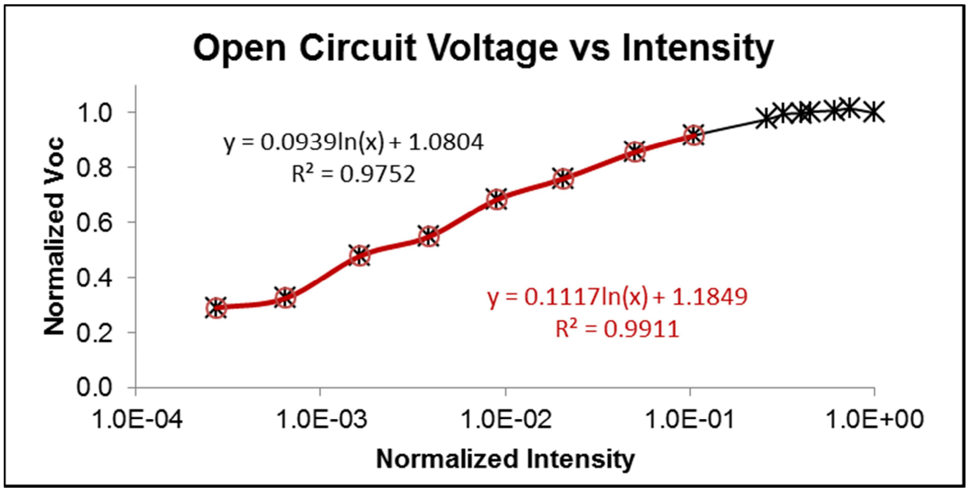

**Figure 33. Normalized open circuit voltage vs normalized intensity, three cell average.**

The open circuit voltage showed a logarithmic relationship with intensity, with a reasonable correlation for the full range ($R^2 = 0.9752$) and a very close correlation from the minimum measured intensity to 10% of AM1.5 ($R^2 = 0.9911$).

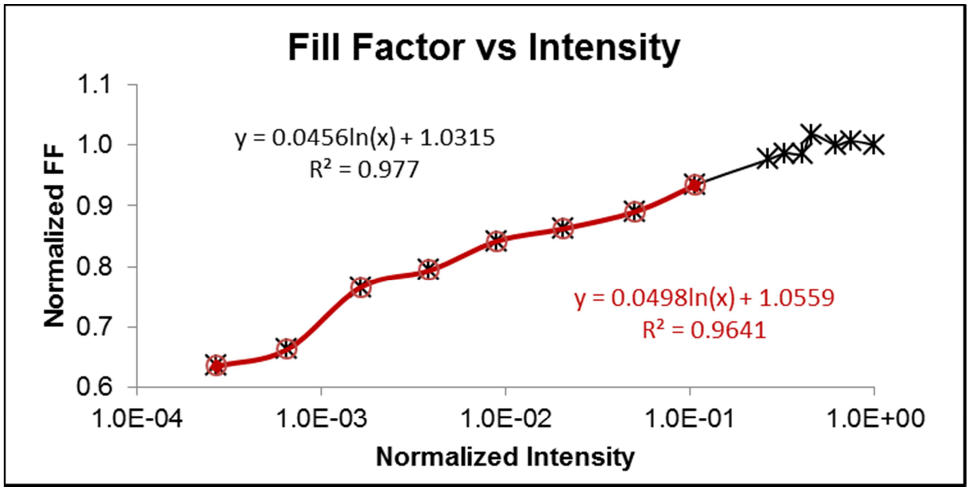

**Figure 34. Normalized fill factor vs normalized intensity, three cell average.**

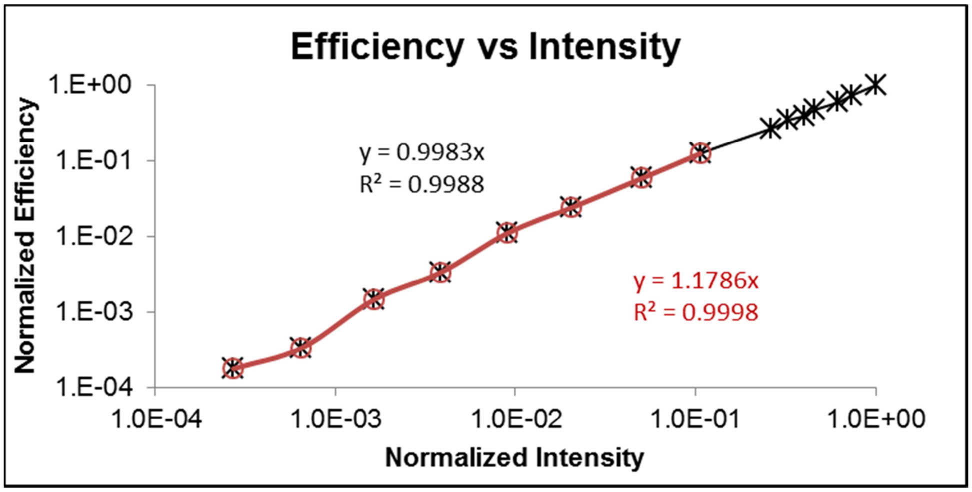

**Figure 35. Normalized power conversion efficiency vs normalized intensity, three cell average.**

The open circuit voltage and the fill factor, and to a lesser extent the efficiency and short circuit current, showed a strange deviation from linearity at the low side of the intensity range. By examining the effects of the filters more closely, it was noticed that intensities at various wavelengths did not decrease equally, as eluded to above. The “bumps” in operating characteristics at the low intensity end were also seen in the variation in intensity at 400 and 600 nm wavelengths in Figure 36, indicating wavelengths in this range had a dominant effect on performance.

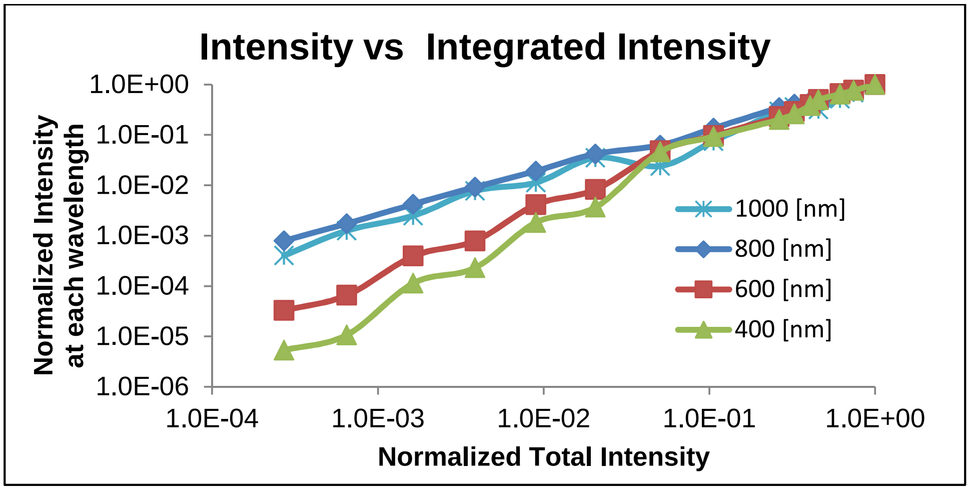

**Figure 36. Intensity at specific wavelengths as a function of total intensity. Because the initial AM1.5 spectrum intensity varies as a function of wavelength, each**

**wavelength investigated was normalized to its peak intensity (i.e. no filters) for easy side-by-side comparison. The same step-like behavior exhibited for 600 and 400 nm light at low intensity can be seen in figures 32 through 35.**

### 4.7.3 Indoor testing

Flexible cells were also tested using off-the-shelf light bulbs at distances from 10 cm to 1.5 m in an otherwise dark room. The bulbs chosen were 75 W incandescent bulbs with 850 Lumen outputs at a 3000 K color temperatures (F 75A/D/4) and compact fluorescent (CFL) bulbs rated at 75 W (18 W actual usage) with 1170 Lumen and color temperatures of 2700 W. Lumens measure light intensity scaled with the sensitivity of the human eye, as opposed to radiant flux which is not scaled.

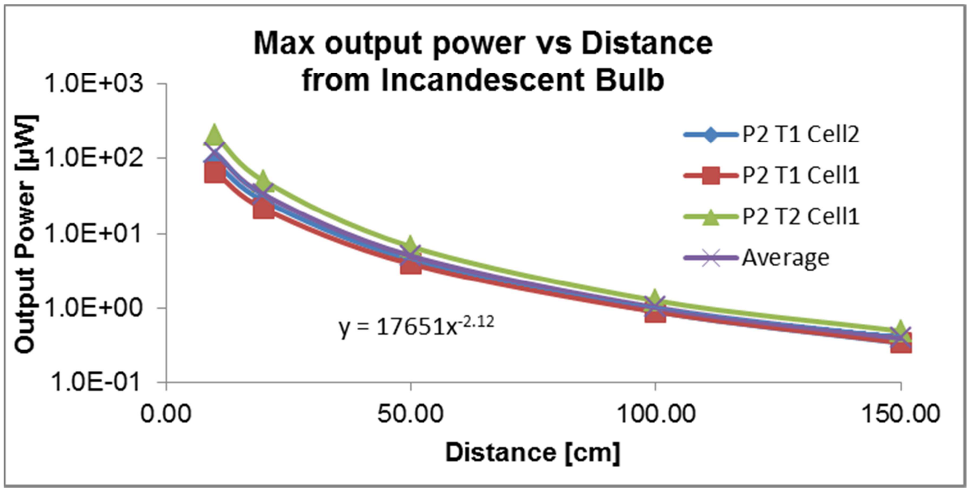

**Figure 37. Solar cell output power as a function of distance from a standard 75 W incandescent bulb.**

The maximum power output from the solar cells as a function of distance from an incandescent bulb closely followed optical power from a point source ($1/r^2$), as shown in Figure 37. The power from the CFL significantly deviated from this relationship, likely due to the fact that the bulb was less like a point source at close distances. At 1.5 m, the CFL bulb could be approximated as a point source, but at 10 cm that approximation is very inaccurate because of the coiled glass tubing. Lastly, the cells were measured at 2 m from a white wall in a normal laboratory room with fluorescent tube lighting. The cells were not pointed at the overhead lighting, but rather were parallel with the wall as if staring at it. Despite the poor efficiency, about 400 nW of power was produced in these conditions. The average power produced as a function of distance from CFL and incandescent bulbs was plotted in Figure 39.

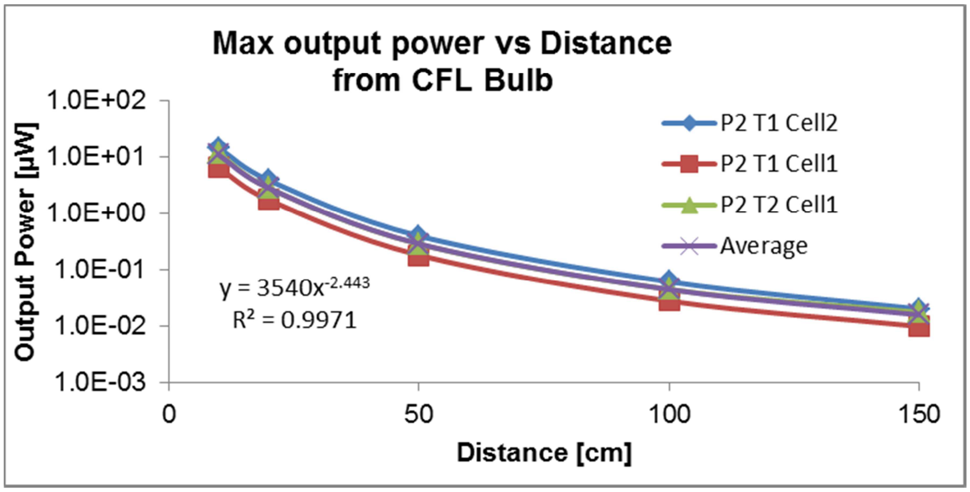

**Figure 38. Solar cell output power as a function of distance from a standard 75 W equivalent CFL bulb.**

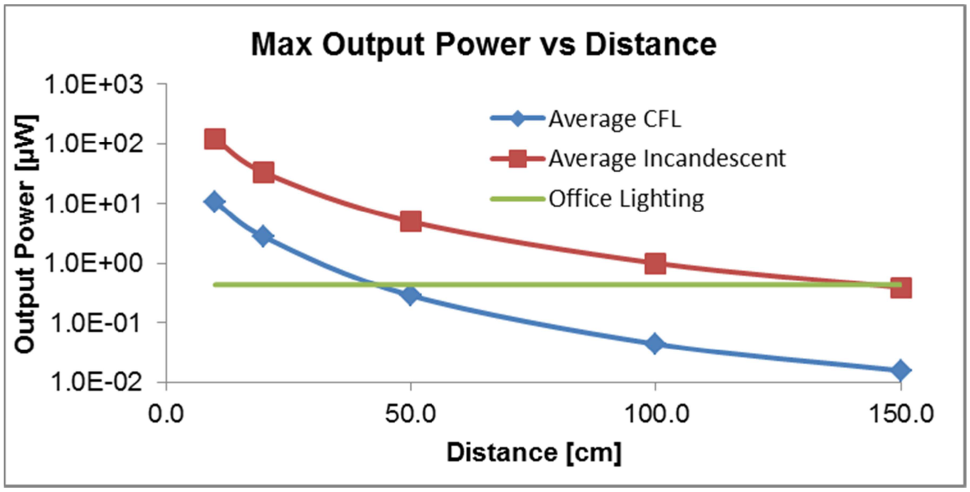

**Figure 39. Average power produced by solar cells from CFL and incandescent bulbs, plotted alongside the power produced at 2 m from a white wall in an office building. The office lighting power was not measured as a function of distance, but was included to show the actual power generated in a well lit room.**

### 4.7.4 Flexibility testing

Initially, solar cells were assembled onto planar PET substrates for testing. However, when assembled onto lenses and molded, the restoring force of the fingers was sufficient to break the connection between the solder and cell when the solder was molten, as shown in Figure 40.

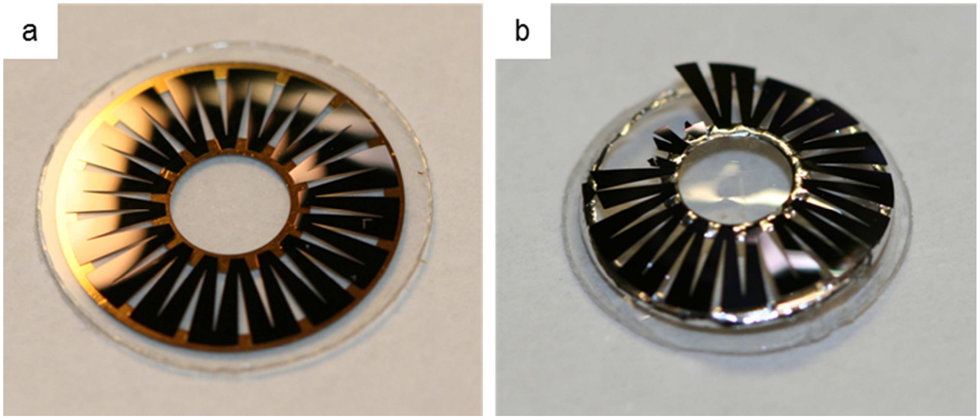

**Figure 40. Assembled meander type solar cells. a) Assembled solar cell on a planar surface. b) Solar cell on a molded substrate. The solder forces were not sufficient to withstand the restoring force of the bent fingers. Several fingers broke while attempting to manually reattach the fingers to the substrate.**

To solve this problem, cells were first coated with approximately 15 µm of parylene and then molded. The resulting curved structures (Figure 41) were tested under AM1.5 conditions. A summary of cell characteristics before and after molding is given in Table 8. The average short circuit current density dropped significantly (~25%), and the average fill factor also decreased (~8%), reducing the efficiency. However, the Type 2 cell only had a 2% reduction in efficiency. It was determined that the restoring force of the silicon beams likely broke the connection between the substrate and the inner contact in Type 1 Cells, as shown in the red circles in Figure 41. Although the differences between Type 1 and Type 2 cells were not substantial, Type 2 cells had a larger gap between silicon meanders and allowed for easier bending. Therefore, the drop in short circuit current density was likely not due to any degradation in cell performance as a function of strain, but more likely to do a reduction in short circuit current from individual fingers that were not electrically connected.

**Table 8. Solar cell characteristics before and after molding.**

| | Before Molding | | | | |
|---|---|---|---|---|---|
| | P1 T1* Cell1 | P1 T1 Cell2 | P1 T1 Cell3 | P1 T2 Cell2 | Average |
| Voc [V] | 0.357 | 0.354 | 0.358 | 0.365 | 0.358 |
| Isc [mA] | 0.692 | 1.093 | 0.768 | 3.088 | 1.410 |
| Jsc [mA/cm2] | 1.243 | 1.963 | 1.380 | 6.098 | 2.671 |
| Fill Factor | 0.63 | 0.62 | 0.45 | 0.59 | 0.57 |
| Efficiency [%] | 0.28 | 0.43 | 0.22 | 1.32 | 0.56 |
| | | | | | |
| | After Molding | | | | |
| | P1 T1 Cell1 | P1 T1 Cell2 | P1 T1 Cell3 | P1 T2 Cell2 | Average |
| Voc [V] | 0.371 | 0.388 | 0.365 | 0.387 | 0.378 |
| Isc [mA] | 0.396 | 0.919 | 0.429 | 3.109 | 1.213 |
| Jsc [mA/cm2] | 0.710 | 1.650 | 0.771 | 6.139 | 2.318 |
| Fill Factor | 0.63 | 0.40 | 0.41 | 0.54 | 0.50 |
| Efficiency [%] | 0.17 | 0.26 | 0.12 | 1.29 | 0.46 |
| | | | | | |
| | Percent Difference [%] | | | | |
| | P1 T1 Cell1 | P1 T1 Cell2 | P1 T1 Cell3 | P1 T2 Cell2 | Average |
| Voc | 4.0 | 9.9 | 2.0 | 6.1 | 5.5 |
| Isc | -42.8 | -15.9 | -44.1 | 0.7 | -25.5 |
| Jsc | -42.8 | -15.9 | -44.2 | 0.7 | -25.6 |
| Fill Factor | -0.4 | -34.6 | -8.4 | -8.6 | -13.0 |
| Efficiency | -40.8 | -39.6 | -47.8 | -2.3 | -32.6 |

*P1 T1 = Process1 Type1

This result was significant because it showed that this type of single crystalline silicon cell could be bent without changing the performance significantly. In the simplest case, the axial strain in a beam bent around a circle of radius $r$ is given by

$$\varepsilon_x = \frac{t}{r}, \tag{4.1}$$

where $\varepsilon_x$ is axial strain and $t$ is distance from the neutral surface of the beam. Therefore, the strain for a given bending radius changes drastically depending on the thickness of the cell. To determine an approximate value for the maximum strain, the inner surface of the cell can be taken as the neutral surface. The strain for these solar cells, assuming $r = 7225$ µm (lens inner curvature and thickness of PET/SU-8 structure) and $t = 15$ µm, the strain $\varepsilon_x \approx 0.21$ %.

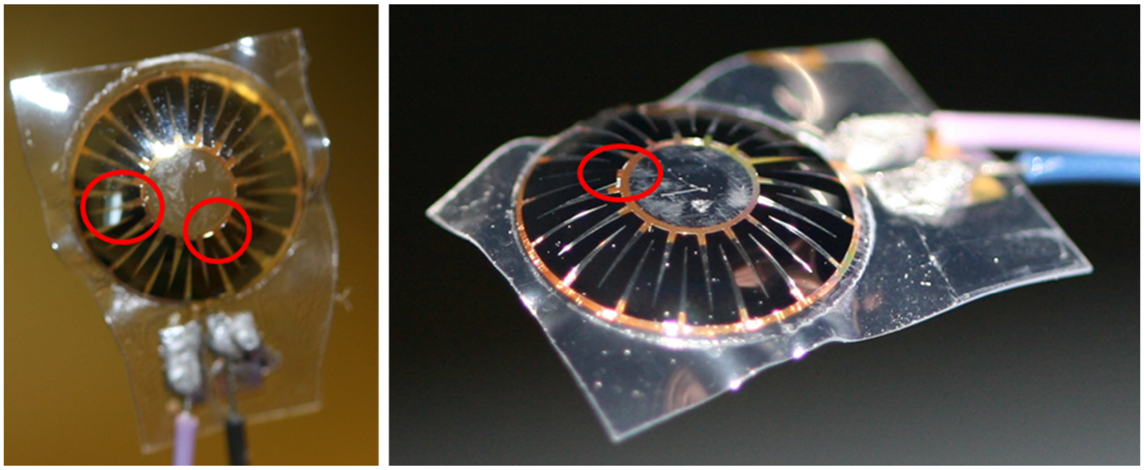

**Figure 41. Two examples of solar cells on molded PET substrates.  The cells were assembled, wired, parylene coated, molded, and then tested under AM1.5 conditions.  Red circles highlight potentially disconnected fingers that could have contributed to reduced short circuit current density and efficiency.**

Flexibility in general was more than sufficient; cells were embedded into PDMS with radius of curvature of 7.1 mm, less than that of the human eye (7.8 mm).  When encapsulated, the cells were very robust, and could withstand repeated folding and bending without fracturing.  Molded and encapsulated solar cells are shown in Figure 42.

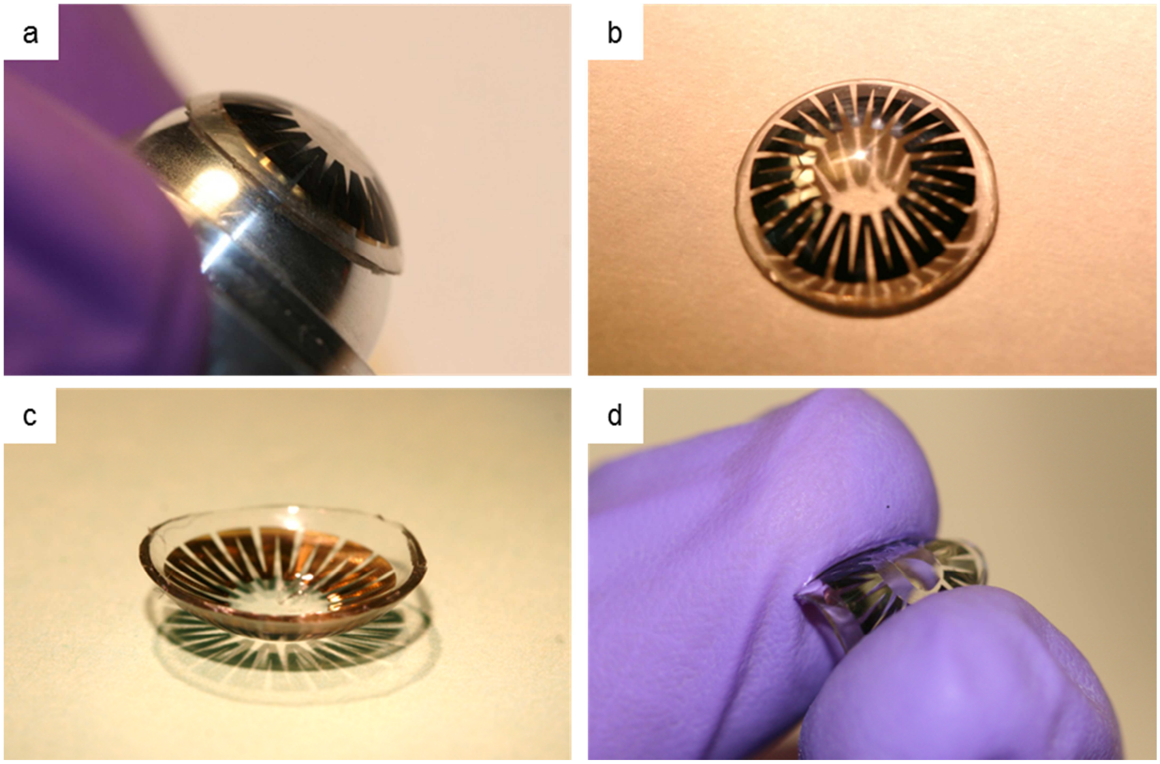

**Figure 42. Flexible solar cell encapsulated in PDMS. a) PDMS encapsulated before being peeled from mold. A razor blade was used to cut the excess PDMS, which resulted in edge imperfections. Also, the spacing between the concave and convex molds was initially 125 µm, but increased when the molds were polished for a smooth surface. b-c) PDMS encapsulated solar cell from various angles. d) The encapsulated cells could be bent and folded without breaking the silicon.**

# Chapter 5: Conclusions

Significant progress has been made toward developing functional contact lenses. First, a single pixel contact lens display powered by remote radio-frequency transmission was demonstrated in free space and on a live rabbit, which verified that antennas, radio chips, control circuitry, and micrometer-scale light sources could be integrated into a contact lens and operated on live eyes. This was achieved by optimizing processes for fabrication on PET templates, solder coating, and component assembly. Although the display had only a single pixel, it was the first proof-of-concept technology demonstration of the long term goal of producing multi-pixel and in-focus images using micro-LED array chips and micrometer-scale Fresnel lenses on transparent substrates.

Although many challenges remain, two prominent issues need to be addressed before a multi-pixel contact lens display can be developed. The first is the optics required to focus light from single pixels onto the retina. The optical power necessary to see a pixel in various light conditions needs to be determined accurately, as well as the how much power can be collected and focused by very small subsidiary lenses. The second major challenge is the determination of an acceptable method to provide power to the system. Although the LED efficiency could be improved, a multi-pixel system would likely dissipate more power because of increased circuit complexity and more pixels, and the LED of the single pixel system demonstrated in Section 2.4 could only be activated at 2 cm *in vivo*. Because the eye contains many ions and proteins, it is not the ideal location to receive RF power on an antenna. Essentially, it is similar to placing a loop antenna on a ground plane, which can significantly reduce its efficiency. Although solar power would not likely provide sufficient power for a display, eventually it may be possible to embed a battery for system operation that could be recharged wirelessly in a periodic fashion.

In addition to single pixel systems, two types of solar cells have been designed for assembly onto contact lens platforms. First, micrometer-scale freestanding cells were fabricated, assembled, and tested. Such a configuration allowed for variable output voltages, which could be beneficial for providing power to CMOS circuitry. However, the assembly was difficult and somewhat unreliable as the number of cells assembled increased. To cover an area of 0.5 $cm^2$, 200 cells (0.25 $mm^2$ each) would have to be assembled. This would require a significant amount of time for a pick-and-place machine, or would require a reliable and robust self-assembly procedure.

To cover more area and for easier assembly, flexible cells were developed that allowed for spherical deformation. Although these cells still exhibited low efficiency, they produced vastly more power because of the larger area covered. Similar back contact back junction cells have demonstrated an order of magnitude higher efficiency, so it is believed that design improvements (i.e. higher emitter coverage), and better control of surface passivation (i.e. front surface $SiN_x$ instead of SOI buried oxide) could substantially increase the efficiency. After improving efficiency through this additional optimization, similar solar cells could provide sufficient power for biosensors in ambient indoor lighting, or they could increase the read range of contact lens sensing systems. With advances in non-volatile memory, it might eventually be possible to power sensors and store data for long periods of time on-lens, while a periodic query could retrieve stored data during a single transfer. Such a system could provide unprecedented measures of health and a wealth of data on the dynamics of biochemistry for researchers.

Improvements are necessary to produce fully functional, remotely powered, contact lens based biosensors as well as displays. First, PET has been used as the contact lens substrate thus far due to the ease of performing some microfabrication processes; however, PET has poor oxygen permeability and its extended use could lead to lactate build up and corneal swelling. It will be necessary to adapt this work to more common rigid gas permeable or hydrogel contact lens materials. Next, the tradeoff between the area covered by the solar cell (i.e. power generated) and oxygen permeability needs to be closely examined. To produce the maximum power, the solar cell should be large, but to maintain a healthy cornea the oxygen permeability must be high. Lastly, much more work needs to be conducted to ensure the feasibility of detecting analytes in the tear film.

# References

[1] R. E. Records, *Physiology of the human eye and visual system*. San Francisco: Harper and Row, 1979.

[2] K. N. Leibovic, Ed., *Science of Vision*. New York: Springer-Verlag, 1990.

[3] A. Phillips and L. Speedwell, Eds., *Contact Lenses*, 5th ed. New York: Elsevier, 2007.

[4] J. Nichols, “Contact Lenses 2010 Annual Report,” 2011.

[5] B. A. Parviz, “For your eye only,” *IEEE Spectrum*, no. September 2009, pp. 36-41, 2009.

[6] I. Lahdesmaki, A. Shum, and B. Parviz, “Possibilities for continuous glucose monitoring by a functional contact lens,” *Instrumentation & Measurement Magazine, IEEE*, vol. 13, no. 3, pp. 14–17, 2010.

[7] H. Ho, E. Saeedi, S. S. Kim, T. Shen, and B. A. Parviz, “Contact lens with integrated inorganic semiconductor devices,” *Micro Electro Mechanical Systems, IEEE 21st Int. Conf. on*, pp. 403-406, 2008.

[8] J. Pandey, Y. T. Liao, A. Lingley, B. Parviz, and B. Otis, “Toward an active contact lens: Integration of a wireless power harvesting IC,” in *Biomedical Circuits and Systems Conference, 2009. BioCAS 2009. IEEE*, 2009, pp. 125–128.

[9] J. Pandey, Y. T. Liao, A. Lingley, R. Mirjalili, B. Parviz, and B. Otis, “A Fully Integrated RF-Powered Contact Lens With a Single Element Display,” *Biomedical Circuits and Systems, IEEE Transactions on*, vol. 4, no. 6, pp. 454–461, 2010.

[10] a R. Lingley et al., “A single-pixel wireless contact lens display,” *Journal of Micromechanics and Microengineering*, vol. 21, no. 12, p. 125014, Dec. 2011.

[11] J. De Smet, a. Avci, R. Beernaert, D. Cuypers, and H. De Smet, “Design and Wrinkling Behavior of a Contact Lens With an Integrated Liquid Crystal Light Modulator,” *Journal of Display Technology*, vol. 8, no. 5, pp. 299-305, May 2012.

[12] D. A. Robinson, “Movemnent Using a Scieral Search in a Magnetic Field *,” *Science*, pp. 137-145, 1963.

[13] H. Collewun, F. Van Der Mark, and T. C. Jansen, “Precise recording of human eye movements,” *Vision Res.*, vol. 15, pp. 447-450, 1975.

[14] S. Takemori, M. Tanaka, and H. Moriyama, “An analysis of ocular counter-rolling measured with search coils.,” *Acta Otolaryngol*, vol. 468, pp. 271-276, Jan. 1989.

[15] S. H. Seidman, R. J. Leigh, and C. W. Thomas, “Eye Movements During Motion After-effect,” vol. 32, no. I, pp. 167-171, 1992.

[16] J. S. Stahl, a M. van Alphen, and C. I. De Zeeuw, “A comparison of video and magnetic search coil recordings of mouse eye movements.,” *Journal of neuroscience methods*, vol. 99, no. 1–2, pp. 101-10, Jun. 2000.

[17] B. J. Hess, “Dual-search coil for measuring 3-dimensional eye movements in experimental animals.,” *Vision research*, vol. 30, no. 4, pp. 597-602, Jan. 1990.

[18] K. Y. Kim, S. Y. Lee, and H. C. Kim, “A wireless measurement system for three-dimensional ocular movement using the magnetic contact lens sensing technique.,” *Proc. of 26th Annual Inter. Conf. of the IEMBS*, vol. 3, pp. 2287-2289, Jan. 2004.

[19] J. B. Kinn and R. a Tell, “A liquid-crystal contact-lens device for measurement of corneal temperature.,” *IEEE transactions on bio-medical engineering*, vol. 20, no. 5, pp. 387-8, Sep. 1973.

[20] M. Leonardi, P. Leuenberger, D. Bertrand, A. Bertsch, and P. Renaud, “First steps toward noninvasive intraocular pressure monitoring with a sensing contact lens.,”

*Investigative ophthalmology & visual science*, vol. 45, no. 9, pp. 3113-7, Sep. 2004.

[21] M. Leonardi, “Microfabricated thin filM Strain GaGe SenSor with teleMetry MicroproceSSor eMbedded in a Soft contact lenS for MiniMally invaSive intraocular preSSure MonitorinG,” *Wired*, vol. 3978, no. 2007, 2008.

[22] M. Leonardi, E. M. Pitchon, A. Bertsch, P. Renaud, and A. Mermoud, “Wireless contact lens sensor for intraocular pressure monitoring: assessment on enucleated pig eyes.,” *Acta ophthalmologica*, vol. 87, no. 4, pp. 433-7, Jun. 2009.

[23] G. B. B. Kristensen and S. Sandberg, “Self-monitoring of blood glucose with a focus on analytical quality: an overview.,” *Clinical chemistry and laboratory medicine : CCLM / FESCC*, vol. 48, no. 7, pp. 963-72, Jul. 2010.

[24] D. C. Klonoff, “Benefits and limitations of self-monitoring of blood glucose.,” *Journal of diabetes science and technology*, vol. 1, no. 1, pp. 130-2, Jan. 2007.

[25] M. X. Chu et al., “Soft contact lens biosensor for in situ monitoring of tear glucose as non-invasive blood sugar assessment.,” *Talanta*, vol. 83, no. 3, pp. 960-5, Jan. 2011.

[26] J. D. Lane, D. M. Krumholz, R. a Sack, and C. Morris, “Tear glucose dynamics in diabetes mellitus.,” *Current eye research*, vol. 31, no. 11, pp. 895-901, Nov. 2006.

[27] R. Badugu, J. R. Lakowicz, and C. D. Geddes, “Noninvasive continuous monitoring of physiological glucose using a monosaccharide-sensing contact lens.,” *Analytical chemistry*, vol. 76, no. 3, pp. 610-8, Feb. 2004.

[28] V. L. Alexeev, S. Das, D. N. Finegold, and S. A. Asher, “Photonic crystal glucose-sensing material for noninvasive monitoring of glucose in tear fluid,” *Clinical chemistry*, vol. 50, no. 12, pp. 2353-60, Dec. 2004.

[29] Y.-te Liao, H. Yao, B. Parviz, and B. Otis, “A 3µW Wirelessly Powered CMOS Glucose Sensor for an Active Contact Lens,” *Contact Lens*, vol. 3, no. June 2009, pp. 2009-2011, 2011.

[30] a Milenkovic, C. Otto, and E. Jovanov, “Wireless sensor networks for personal health monitoring: Issues and an implementation,” *Computer Communications,* vol. 29, no. 13–14, pp. 2521-2533, Aug. 2006.

[31] C. Otto, A. Milenković, C. Sanders, and E. Jovanov, “System architecture of a wireless body area sensor network for ubiquitous health monitoring,” vol. 1, no. 4, pp. 307-326, 2006.

[32] M. J. Schöning and A. Poghossian, “Bio FEDs (Field-Effect Devices): State-of-the-Art and New Directions,” *Electroanalysis*, vol. 18, no. 19–20, pp. 1893-1900, Oct. 2006.

[33] M. K. Law, S. Member, A. Bermak, S. Member, H. C. Luong, and A. An, “A Sub-W Embedded CMOS Temperature Sensor for RFID Food Monitoring Application,” vol. 45, no. 6, pp. 1246-1255, 2010.

[34] Y.-te Liao, H. Yao, A. Lingley, B. Parviz, and B. P. Otis, “A 3 uW CMOS Glucose Sensor for Wireless Contact-Lens Tear Glucose Monitoring,” vol. 47, no. 1, pp. 335-344, 2012.

[35] C. Yang, S. R. Jadhav, R. M. Worden, A. J. Mason, S. Member, and I. Terms, “Compact Low-Power Impedance-to-Digital Converter for Sensor Array Microsystems,” vol. 44, no. 10, pp. 2844-2855, 2009.

[36] A. J. Mason and Y. Huang, “Membrane protein biosensor arrays on CMOS,” *2nd Asia Symposium on Quality Electronic Design (ASQED),* pp. 212-218, Aug. 2010.

[37] M. Alioto and S. Member, “Ultra-Low Power VLSI Circuit Design Demystified and Explained : A Tutorial,” *Circuits and Systems, IEEE Trans. on*, vol. 59, no. 1, pp. 3-29, 2012.

[38] J. A. Paradiso and T. Starner, “Energy Scavenging for Mobile and Wireless Electronics,” *IEEE CS*, pp. 1536-1268, 2005.

[39] G. Chen et al., “Millimeter-Scale Nearly Perpetual Sensor System with Stacked Battery and Solar Cells,” no. June 2009, pp. 166-167, 2010.

[40] D. Kim et al., “A 1 . 85fW / bit Ultra Low Leakage 10T SRAM with Speed Compensation Scheme,” pp. 69-72, 2011.

[41] A. Teman, L. Pergament, O. Cohen, and A. Fish, “A 250 mV 8 kb 40 nm Ultra-Low Power 9T Supply Feedback SRAM (SF-SRAM),” vol. 46, no. 11, pp. 2713-2726, 2011.

[42] E. Y. Chow, S. Chakraborty, W. J. Chappell, and P. P. Irazoqui, “Mixed-Signal Integrated Circuits for Self-Contained Sub-Cubic Millimeter Biomedical Implants,” vol. 36, pp. 236-238, 2010.

[43] M. Zwerg et al., “An 82μA / MHz Microcontroller with Embedded FeRAM,” vol. 4, no. 3, pp. 334-336, 2011.

[44] L. Mateu and F. Moll, “Review of energy harvesting techniques and applications for microelectronics,” *Energy*, 2011.

[45] J. M. Gilbert and F. Balouchi, “Comparison of energy harvesting systems for wireless sensor networks,” *International Journal of Automation and Computing*, vol. 5, no. 4, pp. 334-347, Oct. 2008.

[46] M. T. Penella and M. Gasulla, “A review of commercial energy harvesters for autonomous sensors,” in *Instrumentation and Measurement Technology Conference Proceedings, 2007. IMTC 2007. IEEE*, 2007, pp. 1–5.

[47] A. P. Chandrakasan, D. C. Daly, J. Kwong, and Y. K. Ramadass, “Next Generation Micro-power Systems,” *Symposium A Quarterly Journal In Modern Foreign Literatures*, pp. 2-5, 2008.

[48] B. Warneke, M. Last, B. Liebowitz, and K. S. J. Pister, “Smart Dust : Communicating with a Cubic- Millimeter Computer,” *Computer Magazine*, pp. 44-51, 2001.

[49] B. A. Warneke et al., “An autonomous 16 mm3 solar-powered node for distributed wireless sensor networks,” *Proceedings of IEEE Sensors*, vol. 2, pp. 1510-1515, 2002.

[50] S. S. Clark, J. Gummeson, K. Fu, and D. Ganesan, “Towards Autonomously-Powered CRFIDs,” *Power*, no. October, 2009.

[51] A. P. Sample, J. Braun, A. Parks, and J. R. Smith, “Photovoltaic Enhanced UHF RFID Tag Antennas for Dual Purpose Energy Harvesting,” *Electrical Engineering*, pp. 146-153, 2011.

[52] R. Vyas, V. Lakafosis, Z. Konstas, and M. M. Tentzeris, “Design and Characterization of a Novel Battery-less , Solar Powered Wireless Tag for Enhanced-Range Remote Tracking Applications,” *Solar Cells*, no. October, pp. 169-172, 2009.

[53] I. Doms, P. Merken, and R. Mertens, “Integrated Capacitive Power-Management Circuit for Thermal Harvesters with Output Power 10 to 1000µW,” *Solid-State Circuits*, vol. 5, pp. 300-302, 2009.

[54] K. Zhang, J.-H. Seo, W. Zhou, and Z. Ma, “Fast flexible electronics using transferrable silicon nanomembranes,” *Journal of Physics D: Applied Physics*, vol. 45, no. 14, p. 143001, Apr. 2012.

[55] S. Mack, M. a. Meitl, a. J. Baca, Z.-T. Zhu, and J. a. Rogers, “Mechanically flexible thin-film transistors that use ultrathin ribbons of silicon derived from bulk wafers,” *Applied Physics Letters*, vol. 88, no. 21, p. 213101, 2006.

[56] S. a Stauth and B. a Parviz, “Self-assembled single-crystal silicon circuits on plastic.,” *Proceedings of the National Academy of Sciences of the United States of America*, vol. 103, no. 38, pp. 13922-7, Sep. 2006.

[57] N. Qureshi, E. V. Stepanov, D. Schiraldi, a. Hiltner, and E. Baer, “Oxygen-barrier properties of oriented and heat-set poly(ethylene terephthalate),” *Journal of Polymer Science Part B: Polymer Physics*, vol. 38, no. 13, pp. 1679-1686, Jul. 2000.

[58] E. Saeedi, S. Kim, and B. a Parviz, “Self-assembled crystalline semiconductor optoelectronics on glass and plastic,” *Journal of Micromechanics and Microengineering*, vol. 18, no. 7, p. 075019, Jul. 2008.

[59] R. Feng and R. J. Farris, “Influence of processing conditions on the thermal and mechanical properties of SU8 negative photoresist coatings,” *Journal of Micromechanics and Microengineering*, vol. 13, no. 1, pp. 80-88, Jan. 2003.

[60] P. T. Törmä et al., “Effect of InGaN underneath layer on MOVPE-grown InGaN/GaN blue LEDs,” *Journal of Crystal Growth*, vol. 310, no. 23, pp. 5162-5165, Nov. 2008.

[61] O. Svensk et al., “Enhanced electroluminescence in 405nm InGaN/GaN LEDs by optimized electron blocking layer,” *Journal of Crystal Growth*, vol. 310, no. 23, pp. 5154-5157, Nov. 2008.

[62] H. C. Programme, “ICNIRP statement on the ‘Guidelines for limiting exposure to time-varying electric, magnetic, and electromagnetic fields (up to 300 GHz)’.,” *Health physics*, vol. 97, no. 3, pp. 257-8, Sep. 2009.

[63] “IEEE Standard for Safety Levels IEEE Std C95.1-2005 (Revision of IEEE Std C95.1-1991).” .

[64] A. Swerdlow, “Exposure to high frequency electromagnetic fields, biological effects and health consequences (100 kHz-300 GHz),” *Review Literature And Arts Of The Americas*, 2009.

[65] H. Hoppe and N. S. Sariciftci, “Organic solar cells: An overview,” *Journal of Materials Research*, vol. 19, no. 07, pp. 1924-1945, Mar. 2011.

[66] D. A. Neaman, *Semiconductor Physics and Devices: Basic Principles*. Burr Ridge, Illinois: Irwin, 1992.

[67] A. Goetzberger, J. Knobloch, and V. Bernhard, *Crystalline silicon solar cells*. New York: John Wiley & Sons, 1998, pp. 67-86.

[68] J. Singh, *Semiconductor Devices: An Introduction*. San Francisco: McGraw-Hill, 1994.

[69] M. A. Green and M. J. Keevers, “Optical properties of intrinsic silicon at 300 K,” *Progress in Photovoltaics: Research and Applications1*, vol. 3, no. 3, pp. 189-192, 1995.

[70] W. Shockley and H. J. Queisser, “Detailed Balance Limit of Efficiency of p-n Junction Solar Cells,” *Journal of Applied Physics*, vol. 32, no. 3, p. 510, 1961.

[71] L. C. Hirst and N. J. Ekins-daukes, “Fundamental losses in solar cells,” *Library*, no. August 2010, pp. 286-293, 2011.

[72] a. Wang, J. Zhao, and M. a. Green, “24% Efficient Silicon Solar Cells,” *Applied Physics Letters*, vol. 57, no. 6, p. 602, 1990.

[73] J. Knobloch, S. W. Glunz, D. Biro, W. Warta, E. Schaffer, and W. Wettling, “Solar cells with efficiencies above 21% processed from Czochralski grown silicon,” *Photovoltaic Specialists Conference, 1996*, pp. 405-408, 1996.

[74] J. Zhao, A. Wang, M. a. Green, and F. Ferrazza, “19.8% Efficient ‘Honeycomb’ Textured Multicrystalline and 24.4% Monocrystalline Silicon Solar Cells,” *Applied Physics Letters*, vol. 73, no. 14, p. 1991, 1998.

[75] J. Zhu, C.-M. Hsu, Z. Yu, S. Fan, and Y. Cui, “Nanodome solar cells with efficient light management and self-cleaning.,” *Nano letters*, vol. 10, no. 6, pp. 1979-84, Jun. 2010.

[76] D. Redfield, “Multiple-pass thin-film silicon solar cell,” *Applied Physics Letters*, vol. 25, no. 11, p. 647, 1974.

[77] P. Campbell and M. a. Green, “Light trapping properties of pyramidally textured surfaces,” *Journal of Applied Physics*, vol. 62, no. 1, p. 243, 1987.

[78] S. E. Materials and E. Engineering, “Light trapping in textured solar cells,” *Solar Energy Materials*, vol. 21, pp. 165-172, 1990.

[79] M. a. Green et al., “Present status of buried contact solar cells,” *The Conference Record of the Twenty-Second IEEE Photovoltaic Specialists Conference - 1991*, pp. 46-53, 1991.

[80] W. Shockley and W. T. Read, “Statistics of the Recombination of Holes and Electrons,” *Phys. Rev.*, vol. 87, p. 835, 1952.

[81] C.-T. Sah, R. N. Noyce, and W. T. Shockley, “Carrier generation and recombination in p-n junctions and p-n junction characteristics,” *Proceedings of the IRE*, vol. 109, pp. 1228-1243, 1957.

[82] A. Aberle, “Surface passivation of crystalline silicon solar cells: a review,” *Progress in Photovoltaics: Research and*, no. May, pp. 362-376, 2000.

[83] M. Tao, “A new surface passivation technique for crystalline Si solar cells: Valence-mending passivation,” *Photovoltaic Specialists Conference, 2008. PVSC’08.*, no. 100, 2008.

[84] N. H. Reich et al., “Crystalline silicon cell performance at low light intensities,” *Solar Energy Materials and Solar Cells*, vol. 93, no. 9, pp. 1471-1481, Sep. 2009.

[85] J. Schmidt, A. G. Aberle, and R. Hezel, “Investigation of carrier lifetime instabilities,” 1997.

[86] C. Gong et al., “Comparison of n- and p-type high efficiency silicon solar cell performance under low illumination conditions,” *2008 33rd IEEE Photovolatic Specialists Conference*, pp. 1-4, May 2008.

[87] D. Chapin, C. Fuller, and G. Pearson, “A New Silicon pn Junction Photocell for Converting Solar Radiation into Electrical Power,” *Journal of Applied Physics*, vol. 25, pp. 676-677, 1954.

[88] M. A. Green, K. Emery, Y. Hishikawa, W. Warta, and E. D. Dunlop, “Solar cell efficiency tables ( Version 38 ),” *Library*, no. Version 38, pp. 565-572, 2011.

[89] A. W. Blakers and M. A. Green, “678-mV open-circuit voltage silicon solar cells,” *Applied Physics Letters*, vol. 39, no. 6, p. 483, 1981.

[90] a. W. Blakers et al., “18-Percent Efficient Terrestrial Silicon Solar Cells,” *IEEE Electron Device Letters*, vol. 5, no. 1, pp. 12-13, Jan. 1984.

[91] A. W. Blakers, A. Wang, A. M. Milne, J. Zhao, and M. a. Green, “22.8% Efficient Silicon Solar Cell,” *Applied Physics Letters*, vol. 55, no. 13, p. 1363, 1989.

[92] J. Zhao and A. Wang, “24% efficient PERL structure silicon solar cells,” *Photovoltaic Specialists*, pp. 333-335, 1990.

[93] J. M. Gee, W. K. Schubert, and P. A. Basore, “Emitter wrap-through solar cell,” *Processing,* pp. 265-270, 1993.

[94] C. Ulzhöfer, P. P. Altermatt, N.-P. Harder, and R. Brendel, “Loss analysis of emitter-wrap-through silicon solar cells by means of experiment and three-dimensional device modeling,” *Journal of Applied Physics*, vol. 107, no. 10, p. 104509, 2010.

[95] F. Kiefer et al., “High Efficiency n-Type Emitter-Wrap-Through,” *IEEE Journal of Photovoltaics*, vol. 1, no. 1, pp. 49-53, 2011.

[96] E. V. Kerschaver and G. Beaucarne, “Back-contact solar cells: a review,” *Progress in Photovoltaics: Research and Applications*, vol. 14, no. 2, pp. 107-123, Mar. 2006.

[97] R. Bock, S. Mau, J. Schmidt, and R. Brendel, “Back-junction back-contact n-type silicon solar cells with screen-printed aluminum-alloyed emitter,” *Applied Physics Letters*, vol. 96, no. 26, p. 263507, 2010.

[98] R. Woehl, R. Keding, H. Gentischer, F. Clement, J. Wilde, and D. Biro, “20% Efficient screen-printed and aluminum-alloyed back-contact back-junction cells and interconnection scheme of point-shaped metalized cells,” 2011.

[99] C. L. Bellew, S. Hollar, and K. S. J. Pister, “An SOI process for fabrication of solar cells, transistors and elctrostatic actuators,” pp. 1075-1079, 2003.

[100] P. Ortega and S. Bermejo, “High voltage photovoltaic mini-modules,” *Progress in Photovoltaics:*, 2008.

[101] J. Yoon et al., “Ultrathin silicon solar microcells for semitransparent , mechanically flexible and microconcentrator module designs,” *October*, no. 111, pp. 907-915, 2008.

[102] R. J. Knuesel and H. O. Jacobs, “Self-assembly of microscopic chiplets at a liquid-liquid-solid interface forming a flexible segmented monocrystalline solar cell.,” *Proceedings of the National Academy of Sciences of the United States of America*, vol. 107, no. 3, pp. 993-8, Jan. 2010.

[103] J. L. Cruz-Campa et al., “Microsystems enabled photovoltaics: 14.9% efficient 14µm thick crystalline silicon solar cell,” *Solar Energy Materials and Solar Cells*, vol. 95, no. 2, pp. 551-558, Feb. 2011.

[104] J. L. Cruz-Campa et al., “Ultrathin Flexible Crystalline Silicon: Microsystems-Enabled Photovoltaics,” *IEEE Journal of Photovoltaics*, vol. 1, no. 1, pp. 3-8, Jul. 2011.

[105] T. Minemoto, C. Okamoto, S. Omae, M. Murozono, H. Takakura, and Y. Hamakawa, “Fabrication of Spherical Silicon Solar Cells with Semi-Light-Concentration System,” *Japanese Journal of Applied Physics*, vol. 44, no. 7A, pp. 4820-4824, Jul. 2005.

[106] W. McKee, “Development of the Spherical Silicon Solar Cell,” *IEEE Transactions on Components, Hybrids, and Manufacturing Technology*, vol. 5, no. 4, pp. 336-341, Dec. 1982.

[107] S. P. Lacour, S. Wagner, R. J. Narayan, T. Li, and Z. Suo, “Stiff subcircuit islands of diamondlike carbon for stretchable electronics,” *Journal of Applied Physics*, vol. 100, no. 1, p. 014913, 2006.

[108] P. I. Hsu et al., “Thin-film transistor circuits on large-area spherical surfaces,” *Applied Physics Letters*, vol. 81, no. 9, p. 1723, 2002.

[109] H. C. Ko et al., “A hemispherical electronic eye camera based on compressible silicon optoelectronics.,” *Nature*, vol. 454, no. 7205, pp. 748-53, Aug. 2008.

[110] M. Lu, S. Bowden, and R. Birkmirel, “Two Dimensional Modeling of Interdigitated Back Contact Silicon Heterojunction Solar Cells,” pp. 2007-2008, 2007.

[111] O. Nichiporuk, a Kaminski, M. Lemiti, a Fave, and V. Skryshevsky, “Optimisation of interdigitated back contacts solar cells by two-dimensional numerical simulation,” *Solar Energy Materials and Solar Cells*, vol. 86, no. 4, pp. 517-526, Apr. 2005.

[112] J. Craig, P. Simmons, and S. Patel, “Refractive index and osmolality of human tears,” *Optometry &amp; Vision*, vol. 72, pp. 718-724, 1995.

[113] H. Wong, I. Fatt, and C. J. Radke, “Deposition and Thinning of the Human Tear Film,” *Journal of Colloid and Interface Science*, vol. 184, pp. 44-51, 1996.

[114] J. L. Creech, L. T. Do, I. Fatt, and C. J. Radke, “In vivo tear-film thickness determination and implications for tear-film stability,” *Current Eye Research*, vol. 17, no. 11, pp. 1058-1066, Jan. 1998.

[115] M. J. D. Boer et al., “Guidelines for Etching Silicon MEMS Structures Using Fluorine High-Density Plasmas at Cryogenic Temperatures,” vol. 11, no. 4, pp. 385-401, 2002.

# Appendix A: Final template fabrication process

| | Step | Description | Details |
|---|---|---|---|
| 1 | Clean | | |
| | | Sonicate in acetone | 1 minute |
| | | Soak in IPA | 1 minute |
| | | Rinse in water | Dip in and out 10x |
| | | SRD | |
| 2 | Photolithography | For interconnects, antenna adhesion | |
| | | AZ4620 | rpm, rpm/s, time |
| | | Spread | 500/100/10 |
| | | Spin | 4500/1000/30 |
| | | Soft bake | 35 °C -> 70 °C |
| | | | 10 minute hold at 70 °C |
| | | | 70 °C -> 35 °C |
| | | | 10 minutes in air for rehydration |
| | | Expose | 35 seconds in ABM |
| | | Develop (watch!) | 1.5 minutes in 4:1 AZ400K:DI |
| 3 | Evaporate | Interconnects and antenna adhesion | |
| | | Barrel etch | 30 seconds at 100W |
| | | Deposit Cr/Ni/Au | 20/80/200 nm |
| 4 | Lift-off | Remove lift-off resist | |
| | | Soak in acetone | 1 - 2 hours |
| | | Sonicate | 10 - 60 seconds |
| | | IPA rinse, manual dry, SRD | |
| | Option 1 | Repeat steps 2 - 4, evaporate 50 nm Cr to mask solder wetting | |
| | Option 2 | Repeat steps 2 - 4, evaporate 10/20/100 nm Ti/Pd/Pt for sensor | |
| 5 | Photolithography | | |
| | | Descum in barrel etch | 30 seconds at 75W |
| | | SU-8 2 | |
| | | Spread | 500/100/10 |
| | | Spin | 3000/300/40 |
| | | Soft bake | 35 °C -> 70 °C |
| | | | 15 minute hold at 70 °C |
| | | | 70 °C -> 35 °C |
| | | Expose | 20 seconds in ABM |
| | | Post exposure bake | 35 °C -> 70 °C |
| | | | 10 minutes hold at 70 °C |
| | | | 70 °C -> 35 °C |
| | | Develop | 1.5 minutes in SU-8 developer |
| | | | Rinse with IPA, blow dry, SRD |
| | Option 3 | Repeat steps 2 - 4, evaporate 5/200 nm Cr/Au for bridges over SU-8 2 | |

| | | | |
|---|---|---|---|
| 6 | Evaporate | Seed layer Au | |
| | | Descum in barrel etch | 30 seconds at 75 W |
| | | Deposit Au | 40 nm |
| 7 | Photolithography | For electroplated antenna | |
| | | AZ4620 | |
| | | Spread | 500/100/10 |
| | | Spin | 1500/1000/30 |
| | | Soft bake | 35 °C -> 70 °C |
| | | | 1 hour hold at 70 °C |
| | | | 70 °C -> 35 °C |
| | | Expose | 45 seconds in ABM |
| | | Develop | 3 minutes in 4:1 AZ400K:DI |
| 8 | Electroplate | For thick, low resistance antenna | |
| | | Electroplate | calculate exposed area |
| | | | calculate plating charge in A-min |
| | | | (use 0.8 A-min for contact lens) |
| | | | 60mA, 1 ms on, 1 ms off |
| | | Rinse in water | DI |
| 9 | Resist strip | | |
| | | Soak in acetone | 5 minutes |
| | | Soak in IPA | 2 minutes |
| | | Rinse in DI, use SRD | |
| 10 | Au etch | Etch seed layer | |
| | | Dilute 10:1 DI:Gold etch TFA | Watch until etched, ~1 min |
| | | Rinse with DI, SRD | |
| 11 | Photolithography | For part receptors | |
| | | Descum in barrel etch | 15 seconds at 100W |
| | | SU-8 2 | |
| | | Spread | 500/100/10 |
| | | Spin | 2000/300/40 |
| | | Soft bake | 35 °C -> 70 °C |
| | | | Hold 15 minutes |
| | | | 70 °C -> 35 °C |
| | | Expose | 30 secconds in ABM |
| | | Post exposure bake | 35 °C -> 70 °C |
| | | | 30 minute hold at 70 °C |
| | | | 70 °C -> 35 °C |
| | | Develop | 3.5 minutes in SU-8 developer |
| | | | Rinse with IPA, blow dry, SRD |

# Appendix B: Multi-cell fabrication process

| | Step | Description | Details |
|---|---|---|---|
| 1 | Clean | | |
| | | SC1 or 4:1 Pirhana, dump rinse | 10 minutes, 75 ºC |
| | | SC2, dump rinse | 10 minutes, 75 ºC |
| | | 49% HF, dump rinse, SRD | 2 minutes |
| 2 | Oxide growth | Oxide to mask diffusion | |
| | | Furnace tube | 30 minutes, 1050 ºC |
| | | Bubbler | 98 ºC |
| | | | ~345 nm |
| 3 | Photolithography | Mask for oxide etch | |
| | | HMDS oven | |
| | | AZ1512 | rpm, rpm/s, time |
| | | Spread | 1000/100/10 |
| | | Spin | 4000/20000/30 |
| | | Soft bake | 1:30 minutes, 110 ºC |
| | | Expose | 3.5 seconds in EVG |
| | | Develop (watch!) | 1 minute in 4:1 DI:AZ315 |
| | | Dump rinse, SRD | |
| 4 | Oxide etch | | |
| | | Trion RIE | "Descum" recipe |
| | | | 6.25 minutes in "Oxide" recipe |
| 5 | Resist strip | | |
| | | O2 plasma | 150 W, 5 min |
| | | EKC 830 | 85ºC, 10 min |
| | | Dump rinse | |
| 6 | Clean | | |
| | | SC1 or 4:1 Pirhana, dump rinse | 10 minutes, 75 ºC |
| | | SC2, dump rinse | 10 minutes, 75 ºC |
| | | 10:1 BOE, dump rinse, SRD | 30 seconds |
| 7 | Diffusion | Create emitter regions | |
| | | Spin Filmtronics P509 | Use polymer lining in Headway |
| | | Spread | 500/100/5 |
| | | Spin | 3000/1000/10 |
| | | Prebake | 175ºC, 10 min (use foil) |
| | | Diffuse | 1 hour, 1100 ºC |
| | | | 12% mfc O2, 36% mfc N2 |
| 8 | Oxide strip | Remove oxide and spin-on-dopant | |
| | | 49% HF | 10 minutes |
| | | Dump rinse, SRD | |
| 9 | Clean | | |
| | | SC1 or 4:1 Pirhana, dump rinse | 10 minutes, 75 ºC |
| | | SC2, dump rinse | 10 minutes, 75 ºC |
| | | 49% HF, dump rinse, SRD | 2 minutes |

| | | | |
|---|---|---|---|
| 10 | Photolithography | Lift-off resist for metallization | |
| | | Futurrex NR71-1000PY | rpm, rpm/s, time |
| | | Spread | 500/100/5 |
| | | Spin | 4000/1000/30 |
| | | Soft bake | 150ºC, 1 min |
| | | Expose | 30 seconds in EVG |
| | | Post exposure bake | 100 ºC, 1 min |
| | | Develop (watch!) | 50 seconds in 3:1 RD6:DI |
| | | Dump rinse, SRD | |
| 11 | Evaporate | Deposit metal stack | |
| | | Barrel etch | 30 seconds, 100 W, 1 Torr |
| | | BOE etch, dump rinse, SRD | 15 seconds |
| | | Deposit Cr/Ni/Au | 20/80/200 nm |
| 12 | Lift-off | Remove lift-off resist | |
| | | Soak in acetone | 20 minutes (or until metal sheets off) |
| | | Sonicate | 10-60 seconds |
| | | IPA rinse, dry, SRD | |
| | | Surfactant soak | NCW-1001 (Wako) in DI bath |
| | | Dump rise, SRD | |
| 13 | Photolithography | Define component shape | |
| | | AZ4620 | rpm, rpm/s, time |
| | | Spread | 500/100/10 |
| | | Spin | 4500/1000/30 |
| | | Soft bake | 5 minutes, 110 ºC |
| | | Expose | 45 seconds in EVG |
| | | Develop (watch!) | 5 minute in 4:1 H20:AZ315 |
| | | Dump rinse, SRD | |
| | | Barrel etch | 300W, 3 min |
| | | Hard Bake | 110ºC, 30 min |
| 14 | Silicon etch | Bosch to buried oxide | |
| | | Oxford DRIE | "Standard Bosch" recipe |
| | | | 32 loops |
| 15 | Resist strip | Remove tough resist | |
| | | O2 plasma | 18.5 minutes, 150 W |
| 16 | PDMS bond | Bond SOI to handle wafer | |
| | | Mix | |
| | | Sylgard 184, 10:1 | |
| | | Use NTUF shaker | 10 minutes at 1500 rpm |
| | | PDMS on SOI and handle | 1500 rpm, 1 min |
| | | Spread | 500/100/10 |
| | | Spin | 1500/1000/30 |
| | | Planarize | 24 hours on flat surface |
| | | Plasma treat, barrel etcher | 30 seconds, 1 Torr, 25 W |
| | | Press together | ~20 - 40 lbs of force in center |
| | | Vacuum bake | 2 hours, 80 ºC |

| | | | |
|---|---|---|---|
| 17 | Silicon etch | Remove SOI handle<br>Oxford DRIE<br>Strike<br><br><br>Etch (watch at end!) | <br><br>5 seconds, 30 mTorr<br>50 W CCP, 2000 W ICP<br>200 SF6 [sccm]<br>2.67 hours, 30 mTorr<br>50 W CCP, 2000 W ICP<br>200 SF6 [sccm] |
| 18 | PDMS etch* | Place wafer in glass beaker face down with 3:1 NMP:TBAF. When parts are released, remove handle wafer. Pour solution and parts through filter paper in funnel into polymer waste container. Rinse filter paper into waste container several times, then into sink for at least 20 minutes. Rinse parts into polymer scintillation vial. | |
| | * Wear proper personal protective equipment | | |

# Appendix C: Flexible-cell fabrication process

| | Step | Description | Details |
|---|---|---|---|
| 1 | Clean | | |
| | | SC1 or 4:1 Pirhana, dump rinse | 10 minutes, 75ºC |
| | | SC2, dump rinse, SRD | 10 minutes, 75ºC |
| | | 49% HF, dump rinse | 2 minutes |
| 2 | Photolithography | Mask for base implant | |
| | | HMDS oven | |
| | | AZ1512 | rpm, rpm/s, time |
| | | Spread | 1000/100/10 |
| | | Spin | 4000/20000/30 |
| | | Soft bake | 1:30 minutes, 110 ºC |
| | | Expose | 3.5 seconds in EVG |
| | | Develop (watch!) | 1 minute in 4:1 DI:AZ315 |
| | | Dump rinse, SRD | |
| 3 | Base implant | Base finger implant | |
| | | Send to Core Systems | n-type, phosphorus |
| | | | 65 keV |
| | | | 7E15/cm2 |
| | | | ~ surface doping 5E20/cm3 |
| 4 | Resist strip | Remove tough resist | |
| | | O2 plasma | 150 W, 5 min |
| | | EKC 830 | 85ºC, 10 min |
| | | Dump rinse | |
| 5 | Clean | | |
| | | SC1 or 4:1 Pirhana, dump rinse | 10 minutes, 75ºC |
| | | SC2, dump rinse, SRD | 10 minutes, 75ºC |
| | | 49% HF, dump rinse | 2 minutes |
| 6 | Photolithography | Mask for emitter implant | |
| | | HMDS oven | |
| | | AZ1512 | rpm, rpm/s, time |
| | | Spread | 1000/100/10 |
| | | Spin | 4000/20000/30 |
| | | Soft bake | 1:30 minutes, 110 ºC |
| | | Expose | 3.5 seconds in EVG |
| | | Develop (watch!) | 1 minute in 4:1 DI:AZ315 |
| | | Dump rinse, SRD | |
| 7 | Emitter implant | Emitter finger implant | |
| | | Send to Core Systems | p-type, boron |
| | | | 23 keV |
| | | | 7E15/cm2 |
| | | | ~ surface doping 5E20/cm3 |
| 8 | Resist strip | Remove tough resist | |
| | | O2 plasma | 150 W, 5 min |
| | | EKC 830 | 85ºC, 10 min |

| | | | |
|---|---|---|---|
| 9 | Clean | | |
| | | SC1 or 4:1 Pirhana, dump rinse | 10 minutes, 75ºC |
| | | SC2, dump rinse, SRD | 10 minutes, 75ºC |
| | | 49% HF, dump rinse | 2 minutes |
| 10 | Nitride | For backside passivation | |
| | | Oxford PECVD | Opt - SiNx |
| | | | 10 minutes, 1 Torr, 20 W |
| | | | 30 NH3, 15 SiH4, 980 N2 [sccm] |
| | | | ~115 nm |
| 11 | Clean | | |
| | | SC1 or 4:1 Pirhana, dump rinse | 10 minutes, 75ºC |
| | | SC2, dump rinse, SRD | 10 minutes, 75ºC |
| | | 10:1 BOE, dump rinse, SRD | 2 minutes |
| 12 | Drive in | Drive in both implants | |
| | | Clean RTA | 2 min, 1100ºC |
| | | | 3x |
| 13 | Photolithography | Mask for via etch | |
| | | HMDS oven | |
| | | AZ1512 | rpm, rpm/s, time |
| | | Spread | 1000/100/10 |
| | | Spin | 4000/20000/30 |
| | | Soft bake | 1:30 minutes, 110 ºC |
| | | Expose | 3.5 seconds in EVG |
| | | Develop (watch!) | 1 minute in 4:1 DI:AZ315 |
| | | Dump rinse, SRD | |
| 14 | Via etch | To contact emitter and base | |
| | | Vision RIE | MFF - Nitride |
| | | | 3 minutes, 40 mTorr, 225 W |
| | | | 10 CHF3, 40 CF4 [sccm] |
| 15 | Resist strip | | |
| | | O2 plasma | 150 W, 5 min |
| | | EKC 830 | 85ºC, 10 min |
| 16 | Photolithography | Lift-off resist for metallization | |
| | | Futurrex NR71-1000PY | rpm, rpm/s, time |
| | | Spread | 500/100/5 |
| | | Spin | 4000/1000/30 |
| | | Soft bake | 150ºC, 1 min |
| | | Expose | 30 seconds in EVG |
| | | Post exposure bake | 100 ºC, 1 min |
| | | Develop (watch!) | 50 seconds in 3:1 RD6:DI |
| | | Dump rinse, SRD | |
| 17 | Evaporate | Deposit metal stack | |
| | | Barrel etch | 30 seconds, 100 W, 1 Torr |
| | | BOE etch, dump rinse, SRD | 15 seconds |
| | | Deposit Ti/Ni/Au | 10/80/200 nm |

| | | | |
|---|---|---|---|
| 18 | Lift-off | Remove lift-off resist | |
| | | Soak in acetone | 20 minutes (or until metal sheets off) |
| | | Sonicate | 10-60 seconds |
| | | IPA rinse, dry, SRD | |
| | | Surfactant soak | NCW-1001 (Wako) in DI bath |
| | | Dump rise, SRD | |
| 19 | Photolithography | Define component shape | |
| | | AZ4620 | rpm, rpm/s, time |
| | | Spread | 500/100/10 |
| | | Spin | 4500/1000/30 |
| | | Soft bake | 5 minutes, 110 ºC |
| | | Expose | 45 seconds in EVG |
| | | Develop (watch!) | 5 minute in 4:1 H20:AZ315 |
| | | Dump rinse, SRD | |
| | | Barrel etch | 300W, 3 min |
| | | Hard Bake | 110ºC, 30 min |
| 20 | Nitride etch | To expose silicon | |
| | | Trion RIE | "Nitride" recipe |
| | | | 1 minute, 130 mTorr, 75 W |
| | | | 15 SF6 [sccm] |
| 21 | Silicon etch | Bosch to buried oxide | |
| | | Oxford DRIE | "Standard Bosch" recipe |
| | | | 32 loops |
| 22 | Oxide etch | To etch majority of buried oxide | |
| | | Trion RIE | "Oxide" recipe |
| | | | 10 minute, 75 mTorr, 50 W |
| | | | 25 CHF3, 5 O2 [sccm] |
| 23 | Resist strip | Remove tough resist | |
| | | O2 plasma | 18.5 minutes, 150 W |
| 24 | PDMS bond | Bond SOI to handle wafer | |
| | | Mix | |
| | | Sylgard 184, 10:1 | |
| | | Use NTUF shaker | 10 minutes at 1500 rpm |
| | | PDMS on SOI and handle | 1500 rpm, 1 min |
| | | Spread | 500/100/10 |
| | | Spin | 1500/1000/30 |
| | | Planarize | 24 hours on flat surface |
| | | Plasma treat, barrel etcher | 30 seconds, 1 Torr, 25 W |
| | | Press together | ~20 - 40 lbs of force in center |
| | | Vacuum bake | 2 hours, 80 ºC |

| | | | |
|---|---|---|---|
| 25 | Silicon etch | Remove SOI handle<br>Oxford DRIE | |
| | | Strike | 5 seconds, 30 mTorr<br>50 W CCP, 2000 W ICP<br>200 SF6 [sccm] |
| | | Etch (watch at end!) | 2.67 hours, 30 mTorr<br>50 W CCP, 2000 W ICP<br>200 SF6 [sccm] |
| 26 | Oxide etch | Thin buried oxide | |
| | | Trion RIE | "Oxide" recipe<br>10 minute, 75 mTorr, 50 W<br>25 CHF3, 5 O2 [sccm] |
| 27 | PDMS etch | Etch all PDMS | |
| | | 3:1 NMP:TBAF | 24 hours<br>Use specially designed holder<br>In 6" evaporating dish |
| 28 | Rinse/store | | |
| | | Deionized water | 10 minutes with with lid on holder |
| | | Store | Individually in plastic containers |

# Appendix D: Handle wafer etch development

With 100% exposed silicon and no masking, aspect ratio, lateral etching, and aspect ratio dependent etching (ARDE) were not primary considerations. However, etch rate, uniformity, and selectivity were crucial. The basic DRIE process in the MFF cleanroom resulted in an etch rate at the center of approximately 80% the etch rate near the edges. Therefore, for a 450 µm etch, the handle, the buried oxide, and the 15 µm device later were completely etched at the periphery before the center was etched to the buried oxide. Normally to achieve high aspect ratio structures, sidewall passivation must be employed to decrease lateral etch rates. However, for a bulk wafer etch, sidewall passivation was not required. Therefore, an $SF_6$-only etch was developed in an inductively coupled plasma etcher, with the purpose of achieve excellent oxide selectivity and high etch rates.

For an $SF_6$ etch, the primary means of oxide erosion is from ion bombardment. Therefore, after determining the max flow rate, the maximum ICP power, minimum capacitively coupled power (CCP), and max chamber pressure while maintaining plasma, an average etch rate of over 3 µm/min and average oxide selectivity higher than 1000:1 was achieved. Increasing the flow and the pressure increases the etch rate and decreases the erosion, respectively. However, the uniformity was still poor, so the buried oxide was not perfectly uniform after etching.

**Table 9. Handle wafer etch parameters.**

| | Strike | Etch |
|---|---|---|
| SF6 flow [sccm] | 200 | 200 |
| ICP Power [W] | 2000 | 2000 |
| CCP Power [W] | 20 | 0 |
| Pressure [mTorr] | 35 | 35 |
| Time | 5 s | 150 min |

# Appendix E: Sentaurus Simulation Files

sProcess command file for parametric sweep or representative cell

```
# Andrew Lingley
# Solar Cell Process Simulation

# 2D grid definition
line x location=0.0 spacing= 100<nm> tag=DeviceTop
line x location=2<um> spacing= 1<um>
line x location=@<Thick-1>@ spacing= 0.5<um>
line x location=@<Thick>@<um> spacing= 0.1<um> tag=DeviceBottom
line x location=@<Thick+0.094>@<um> spacing= 0.1<um> tag=BoxBottom
line y location=0.0<um> spacing= 1<um> tag=CellLeft
line y location=10<um> spacing= 1<um> tag=CellRight

# Initial simulation domain, SOI wafer 15 um device thickness
region oxide xlo=DeviceBottom xhi=BoxBottom
region silicon xlo=DeviceTop xhi=DeviceBottom

# Initialize simulation
init resistivity=@<BaseDope>@<ohm-cm> field=Phosphorus

# Define masks for fast simulation
mask name=base_mask left=1<um> right=3<um>
mask name=emit_mask left=5<um> right=9<um>
mask name=via_mask \
   segments= {1.5<um> 2.5<um> 6<um> 8<um>} negative
mask name=metal_mask \
   segments= {1<um> 3<um> 5<um> 9<um>}

# Refine interface and implant regions
refinebox interface.materials = { Silicon Oxide Nitride Ti }
refinebox min= {0 0.8} max= {1.5 3.2} \
   xrefine= {0.1 0.25 1} yrefine= {0.25 0.25 0.25} silicon
refinebox min= {0 4.8} max= {1.5 9.2} \
   xrefine= {0.1 0.25 1} yrefine= {0.25 0.25 0.25} silicon

# Implant base
photo mask=base_mask thickness=1.5<um>
implant Phosphorus energy=@<PkeV>@<keV> dose=@<PDose>@<cm-2>
tilt=7.0<degree>
strip resist

# Implant emitter
```

```
photo mask=emit_mask thickness=1.5<um>
implant Boron energy=@<BkeV>@<keV> dose=@<BDose>@<cm-2> tilt=7.0<degree>
strip resist

# Deposit nitride
deposit nitride type=anisotropic thickness=120<nm>

# Diffuse dopants
diffuse temperature=1100<C> init=0.001<s> time=@<DiffTime>@<min>

# Etch vias
etch nitride type=isotropic etchstop= {Si} thickness=120<nm> mask=via_mask

# Deposit and lift-off metal layer stack
photo mask=metal_mask thickness=3

deposit material=Ti thickness=10<nm> type=anisotropic
deposit material=Ni thickness=80<nm> type=anisotropic
deposit material=Al thickness=200<nm> type=anisotropic

strip resist

# Define contacts
contact name=nContact x=-190<nm> y=2<um> point
contact name=pContact x=-190<nm> y=7<um> point

# Check structure
struct tdr= n@node@_TSC1_Final

# Define structure for sdevice
struct smesh= n@node@_TSC1mesh
```

sDevice command file for parametric sweep or representative cell

```
# Andrew Lingley
# Solar Cell Device Simulation

# Set dependence on previous node
#setdep @previous@

# Set input and output files
File
{
  * Input files
  Grid = "n@node|-1@_TSC1mesh_fps.tdr"
  IlluminationSpectrum= "spectra/am15g.txt"
  Parameter= "@parameter@"

  * Output files
  Plot = "n@node@_des.tdr"
  Current = "n@node@_des.plt"
}

# Select contacts for simulation
Electrode
{
  { Name="nContact" Voltage=0.0 }
  { Name="pContact" Voltage=0.0 }
}

# Set physical models to employ
Physics
{
  AreaFactor= 1e10    * Gives mA/cm^2 for a 10 x 1 um^2 cell
  Mobility (DopingDependence HighFieldSat Enormal)
  EffectiveIntrinsicDensity (BandGapNarrowing (OldSlotboom))

  Optics
  (
    ComplexRefractiveIndex (WavelengthDep(Real Imag))
    OpticalGeneration
    (
      QuantumYield (StepFunction (EffectiveBandgap))
      ComputeFromSpectrum
      TimeDependence (Wavetime= (1,2) WaveTSlope= 0.05)
    )
    Excitation
    (
```

```
      Theta= 180                * From cell front
      Polarization= 0.5         * Unpolarized light
    )
    OpticalSolver
    (
      TMM
      (
        NodesPerWavelength= 100 *TMM mesh points
        IntensityPattern= StandingWave
        Stripe
           (
                   Left= 0
                   Right= 10
                 )
      )
    )
  )

  Recombination
  (
    SRH(DopingDependence)
    Auger
  )
}

# Account for front surface recombination
Physics (MaterialInterface="Silicon/Oxide")
{
  Recombination(surfaceSRH)
}

# Account for back surface recombination
Physics (MaterialInterface="Silicon/Nitride")
{
  Recombination(surfaceSRH)
}

Plot
{
  * Bands and fields
  Potential SpaceCharge ElectricField EffectiveBandGap
  * Carrier densities, lifetimes, mobilities
  eDensity hDensity eLifeTime hLifeTime eMobility hMobility
  * Current densities
  eCurrent/Vector hCurrent/Vector TotalCurrent/Vector
```

```
  * Generation
  OpticalGeneration
  * Recombination
  SurfaceRecombination TotalRecombination
}

Math
{
  Extrapolate
  Derivates
  RelErrControl
  BreakCriteria
  {
    Current(Contact="pContact" maxval=0)
  }
}

Solve
{
  * Initial solution
  Poisson

  * Ramp up optical generation
  Transient
  (
    InitialTime=0 FinalTime=1.0
    InitialStep=1 MaxStep=1 Minstep=1e-5
  )
  { Coupled { Poisson Electron Hole } }

  * Ramp pContact voltage
  Quasistationary
  (
    MaxStep=0.01
    Goal{ Name="pContact" Voltage=0.7 }
  )
  { Coupled { Poisson Electron Hole } }
}
```

## Inspect command file for parametric sweep or representative cell

```
# Andrew Lingley
# Solar Cell Parameter Extraction and Plotting

# Set node dependence
#setdep @previous@

# Set up some variables to extract
#set Jsc x
#set Voc x
#set Pmpp x
#set FF x
#set Efficiency x

# Create some variable numbers
set n     @node@
set i     @node:index@

# Load data from SDevice into a project called PLT_JV
proj_load n@node|sdevice@_des.plt PLT_JV($n)

# Define a few constants
set Ps 100.0

# Plot illuminated J-V and characteristics in first quadrant
# Current was converted to J using "AreaFactor" in SDevice
cv_create J($n) "PLT_JV($n) pContact OuterVoltage" "PLT_JV($n) nContact
TotalCurrent"

# Plot illuminated P-V and characteristics in first quadrant
cv_create V($n)  "PLT_JV($n) pContact OuterVoltage" "PLT_JV($n) pContact
OuterVoltage"
cv_createWithFormula P($n)  "<V($n)>*<J($n)>" A A

# Extract short circuit current density, Jsc [mA/cm^2]
set Jsc($n) [cv_compute "vecvaly(<J($n)>,0.0)" A A A A]

# Extract open circuit voltage, Voc [V]
set Jmin [cv_compute "vecmin(<J($n)>)" A A A A]
if {$Jmin <= 0} {
        set Voc($n) [expr [cv_compute "veczero(<J($n)>)" A A A A]]
} elseif {$Jmin <= 1e-6} {
        set Voc($n) [expr [cv_compute "vecvalx(<J($n)>,$Jmin)" A A A A]]
}
```

```
# Extract fill factor (FF), maximum power output (Pmpp [mW/cm2]) and efficiency [%]

set Pmpp($n) [cv_compute "vecmax(<P($n)>)" A A A A]
set FF($n) [expr $Pmpp($n)/($Voc($n)*$Jsc($n))*100]
set Efficiency($n) [expr $Pmpp($n)/$Ps*100]

#; Write Extracted variables to SWB
ft_scalar Jsc [format %.2f $Jsc($n)]
ft_scalar Voc [format %.4f $Voc($n)]
ft_scalar Pmpp [format %.2f $Pmpp($n)]
ft_scalar FF  [format %.2f $FF($n)]
ft_scalar Efficiency  [format %.2f $Efficiency($n)]

puts "Done"
```

sProcess command file for front surface recombination sweep of realistic cell

```
#Andrew Lingley
#Solar Cell Simulation
#Front surface recombination sweep

# 2D grid definition for real cell
line x location=0.0 spacing= 100<nm> tag=DeviceTop
line x location=5<um> spacing= 2<um>
line x location=10<um> spacing= 2<um>
line x location=15<um> spacing= 100<nm> tag=DeviceBottom
line x location=15.085<um> spacing= 100<nm> tag=BoxBottom
line y location=0.0<um> spacing= 2<um> tag=CellLeft
#line y location=10<um> spacing= 1<um>
#line y location=25<um> spacing= 5<um>
#line y location=40<um> spacing= 1<um>
#line y location=50<um> spacing= 5<um>
#line y location=60<um> spacing= 1<um>
#line y location=100<um> spacing= 10<um>
#line y location=140<um> spacing= 1<um>
line y location=150<um> spacing= 2<um> tag=CellRight

# Initial simulation domain, SOI wafer 15 um device thickness
region oxide xlo=DeviceBottom xhi=BoxBottom
region silicon xlo=DeviceTop xhi=DeviceBottom

# Initialize simulation
init resistivity=@<BaseDope>@<ohm-cm> field=Phosphorus

# Define masks for fast simulation
mask name=base_mask left=10<um> right=40<um>
mask name=emit_mask left=60<um> right=140<um>
mask name=via_mask segments= {20<um> 30<um> 80<um> 90<um> 110<um>
120<um>} negative
mask name=metal_mask segments= {10<um> 40<um> 60<um> 140<um>}

# Refine interface and implant regions
refinebox interface.materials = { Silicon Oxide Nitride Ti }
refinebox min= {0 8} max= {4 42} \
  xrefine= {0.01 0.2 1} yrefine= {0.2 2 0.2} silicon
refinebox min= {0 58} max= {4 142} \
  xrefine= {0.01 0.2 1} yrefine= {0.2 2 0.2} silicon

# Implant base
photo mask=base_mask thickness=1.5<um>
```

```
implant Phosphorus energy=@<PkeV>@<keV> dose=@<PDose>@<cm-2>
tilt=7.0<degree>
strip resist

# Implant emitter
photo mask=emit_mask thickness=1.5<um>
implant Boron energy=@<BkeV>@<keV> dose=@<BDose>@<cm-2> tilt=7.0<degree>
strip resist

# Deposit nitride
deposit nitride type=anisotropic thickness=75<nm>

# Diffuse dopants
diffuse temperature=1100<C> init=0.001<s> time=@<DiffTime>@<min>

# Etch vias
etch nitride type=isotropic etchstop= {Si} thickness=80<nm> mask=via_mask

# Deposit and lift-off metal layer stack
photo mask=metal_mask thickness=3

deposit material=Ti thickness=10<nm> type=anisotropic
deposit material=Ni thickness=80<nm> type=anisotropic
deposit material=Al thickness=200<nm> type=anisotropic

strip resist

# Define contacts
contact name=nContact x=-190<nm> y=25<um> point
contact name=pContact x=-190<nm> y=100<um> point

# Check structure
struct tdr= n@node@_TSC1_Final

# Define structure for sdevice
struct smesh= n@node@_TSC1mesh
```

### sDevice command file for front surface recombination sweep of realistic cell

```
# Andrew Lingley
# Solar Cell Device Simulation
# Front surface recombination sweep

# Set dependence on previous node
#setdep @previous@

# Set input and output files
File
{
  * Input files
  Grid = "n@node|-1@_TSC1mesh_fps.tdr"
  IlluminationSpectrum= "spectra/am15g.txt"
  Parameter= "@parameter@"

  * Output files
  Plot = "n@node@_des.tdr"
  Current = "n@node@_des.plt"
}

# Select contacts for simulation
Electrode
{
  { Name="nContact" Voltage=0.0 }
  { Name="pContact" Voltage=0.0 }
}

# Set physical models to employ
Physics
{
  AreaFactor= 666666666 * Gives mA/cm^2 for cell area in um^2
  Mobility (DopingDependence HighFieldSat Enormal)
  EffectiveIntrinsicDensity (BandGapNarrowing (OldSlotboom))

  Optics
  (
    ComplexRefractiveIndex (WavelengthDep(Real Imag))
    OpticalGeneration
    (
      QuantumYield (StepFunction (EffectiveBandgap))
      ComputeFromSpectrum
      TimeDependence (Wavetime= (1,2) WaveTSlope= 0.05)
    )
    Excitation
```

```
    (
      Theta= 180                * From cell front
      Polarization= 0.5         * Unpolarized light
    )
    OpticalSolver
    (
      TMM
      (
        NodesPerWavelength= 100 *TMM mesh points
        IntensityPattern= StandingWave
        Stripe
           (
                Left= 0
                Right= 150
              )
      )
    )
  )

  Recombination
  (
    SRH(DopingDependence)
    Auger
  )
}

# Account for front surface recombination
Physics (MaterialInterface="Silicon/Oxide")
{
  Recombination(surfaceSRH)
}

# Account for back surface recombination
Physics (MaterialInterface="Silicon/Nitride")
{
  Recombination(surfaceSRH)
}

Plot
{
  * Bands and fields
  Potential SpaceCharge ElectricField EffectiveBandGap
  * Carrier densities, lifetimes, mobilities
  eDensity hDensity eLifeTime hLifeTime eMobility hMobility
  * Current densities
```

```
  eCurrent/Vector hCurrent/Vector TotalCurrent/Vector
  * Generation
  OpticalGeneration
  * Recombination
  SurfaceRecombination TotalRecombination
}

Math
{
  Extrapolate
  Derivates
  RelErrControl
  BreakCriteria
  {
    Current(Contact="pContact" maxval=0)
  }
}

Solve
{
  * Initial solution
  Poisson

  * Ramp up optical generation
  Transient
  (
    InitialTime=0 FinalTime=1.0
    InitialStep=1 MaxStep=1 Minstep=1e-5
  )
  { Coupled { Poisson Electron Hole } }

  * Ramp pContact voltage
  Quasistationary
  (
    MaxStep=0.01
    Goal{ Name="pContact" Voltage=0.7 }
  )
  { Coupled { Poisson Electron Hole } }
}
```

### Inspect command file for front surface recombination sweep of realistic cell

```
# Andrew Lingley
# Solar Cell Parameter Extraction and Plotting
# Front surface recombination sweep

# Set node dependence
#setdep @previous@

# Set up some variables to extract
#set Jsc x
#set Voc x
#set Pmpp x
#set FF x
#set Efficiency x

# Create some variable numbers
set n    @node@
set i    @node:index@

# Load data from SDevice into a project called PLT_JV
proj_load n@node|sdevice@_des.plt PLT_JV($n)

# Define a few constants
set Ps 100.0

# Plot illuminated J-V and characteristics in first quadrant
# Current was converted to J using "AreaFactor" in SDevice
cv_create J($n) "PLT_JV($n) pContact OuterVoltage" "PLT_JV($n) nContact
TotalCurrent"

# Plot illuminated P-V and characteristics in first quadrant
cv_create V($n)  "PLT_JV($n) pContact OuterVoltage" "PLT_JV($n) pContact
OuterVoltage"
cv_createWithFormula P($n)  "<V($n)>*<J($n)>" A A

# Extract short circuit current density, Jsc [mA/cm^2]
set Jsc($n) [cv_compute "vecvaly(<J($n)>,0.0)" A A A A]

# Extract open circuit voltage, Voc [V]
set Jmin [cv_compute "vecmin(<J($n)>)" A A A A]
if {$Jmin <= 0} {
        set Voc($n) [expr [cv_compute "veczero(<J($n)>)" A A A A]]
} elseif {$Jmin <= 1e-6} {
        set Voc($n) [expr [cv_compute "vecvalx(<J($n)>,$Jmin)" A A A A]]
}
```

```
# Extract fill factor (FF), maximum power output (Pmpp [mW/cm2]) and efficiency [%]

set Pmpp($n) [cv_compute "vecmax(<P($n)>)" A A A A]
set FF($n) [expr $Pmpp($n)/($Voc($n)*$Jsc($n))*100]
set Efficiency($n) [expr $Pmpp($n)/$Ps*100]

#; Write Extracted variables to SWB
ft_scalar Jsc [format %.2f $Jsc($n)]
ft_scalar Voc [format %.4f $Voc($n)]
ft_scalar Pmpp [format %.2f $Pmpp($n)]
ft_scalar FF  [format %.2f $FF($n)]
ft_scalar Efficiency  [format %.2f $Efficiency($n)]

puts "Done"
```

Example parameter file for sweep, including n-k files (not shown) and materials properties

```
# Andrew Lingley
# Solar Cell Device Simulation Parameter File

Material = "Nitride"  {
 #include "SiN-nk.par"
}

Material = "Silicon" {
 #include "Si.par"
 #include "Si-nk.par"
}

Material = "Oxide"  {
 #include "SiN-nk.par"
}

Material = "Titanium"  {
 #include "Ti-nk.par"
}

Material = "Nickel"  {
 #include "Ni-nk.par"
}

Material = "Aluminum"  {
 #include "Al-nk.par"
}

MaterialInterface = "Silicon/Oxide" {
   SurfaceRecombination {
      S0 = @Sfront@, @Sfront@ * [cm/s]
      Sref = 0 * [1], no doping dependence
   }
}

MaterialInterface = "Silicon/Nitride" {
   SurfaceRecombination {
      S0 = @Sback@, @Sback@ * [cm/s]
      Sref = 0.001 * [1], doping dependence
      Nref = 1e15 * [cm-3] for ~5 Ohm-cm Phosphorus
   }
}
```

# Appendix F: Pseudo self-assembly process

| | Step | Details |
|---|---|---|
| 1 | Turn on hotplate 1 | set to 225ºC |
| 2 | Clean substrates | spray with acetone/IPA 2x<br>dry with nitrogen |
| 3 | Polish edges | cut small bit of 5 µm grit<br>hold in fingers and polish edges |
| 4 | Clean substrates | spray with acetone/IPA 2x<br>dry with nitrogen |
| 5 | Prepare solar cells | Pipette cells into vial with DI<br>Remove as much DI as possible<br>Add 10 mL EG, swish thoroughly |
| 6 | Prepare petri dish | pour 25 mL of EG in petri dish<br>add 10 µL HCl, mix<br>place dish on cold hotplate 2 under microscope |
| 7 | Heat solder | place solder beaker in water beaker<br>place beakers on hot plate<br>when solder reaches 90 ℃ add 60 µL HCl<br>wait 1-2 minutes, pipette all EG out<br>add 10 mL EG<br>add 60 µL HCl |
| 8 | Coat template | pick up substrate with broad tweezers<br>pipette solder over template*<br>check in microscope, repeat coat if necessary<br>place in petri dish |
| 9 | Place cells and reflow | use pipette to place components<br>turn heat up to 5<br>after ~2 min, solder should melt (but watch)<br>turn on spinner (to cause vibration) ~15 seconds |
| 10 | Cool | take petri dish off hot plate<br>wait ~5 minutes<br>rinse with IPA, dry with nitrogen<br>place substrates on fluoroware with blue tape |
| | *Change angles and flow rate if necessary | |